

---


Electronic Theses and Dissertations, 2004-2019

---

2019

## Development of a Single Sensor Approach for Capturing Three-Dimensional, Time Resolved Flame and Velocity Information

Jonathan Reyes  
*University of Central Florida*

 Part of the [Mechanical Engineering Commons](#)  
Find similar works at: <https://stars.library.ucf.edu/etd>  
University of Central Florida Libraries <http://library.ucf.edu>

This Doctoral Dissertation (Open Access) is brought to you for free and open access by STARS. It has been accepted for inclusion in Electronic Theses and Dissertations, 2004-2019 by an authorized administrator of STARS. For more information, please contact [STARS@ucf.edu](mailto:STARS@ucf.edu).

---

### STARS Citation

Reyes, Jonathan, "Development of a Single Sensor Approach for Capturing Three-Dimensional, Time Resolved Flame and Velocity Information" (2019). *Electronic Theses and Dissertations, 2004-2019*. 6426.  
<https://stars.library.ucf.edu/etd/6426>

DEVELOPMENT OF A SINGLE SENSOR APPROACHE FOR CAPTURING THREE-  
DIMENSIONAL, TIME RESOLVED SPECIES AND VELOCITY INFORMATION

by

JONATHAN ELIEL REYES  
B.S. University of Central Florida, 2015  
M.S. University of Central Florida, 2017

A dissertation submitted in partial fulfillment of the requirements  
for the degree of Doctor of Philosophy of Mechanical Engineering  
in the Department of Mechanical and Aerospace Engineering  
in the College of Engineering and Computer Science  
at the University of Central Florida  
Orlando, Florida

Spring Term  
2019

Major Professor: Kareem Ahmed

© 2019 Jonathan Reyes

## ABSTRACT

Performing non-intrusive measurements is the key to acquiring accurate information representative of what is being observed. The act of measuring often changes the environment being observed altering the information that is being obtained. Due to this, the community of fluid scientists have gravitated towards using laser-based measurements to observe the phenomena occurring in their experiments. The study of fluids has advanced since this point, utilizing techniques such as planar laser induced fluorescence (PLIF), particle image velocimetry (PIV), laser doppler velocimetry (LDV), particle doppler anemometry (PDA), etc. to acquire chemical species information and velocity information. These techniques, though, are inherently two-dimensional and cannot fully describe a flow field.

In the area of reacting flow fields (combustion) acquiring the local fuel to air ratio information is increasingly important. Without it, scientist must rely on global one-dimensional metering techniques to correlate the fuel to air ratio of their flow field of interest. By knowing the fuel to air ratio locally and spatially across a flame, the location of products and reactants can be deduced, giving insight into any inefficiencies associated with a burner. Knowing the spatial fuel air field also gives insights into the density gradient associated with the flow field.

Discussed in this work will be the development of a non-intrusive local fuel-air measurement technique and an expansion of the PIV technique into the third dimension, tomographic PIV, utilizing only one camera to do so for each measurement. The local fuel-air measurement is performed by recording two species ( $C_2^*$  and  $CH^*$ ) simultaneously and calibrating their ratio to the known fuel-air field. Tomographic PIV is performed by utilizing fiber coupling to acquire multiple viewpoints utilizing a single camera.

I dedicate this dissertation to the hard-working students at the Center for Advanced Turbomachinery and Energy Research (CATER) and the Propulsion and Energy Research Laboratory (PERL) at the University of Central Florida (UCF). Day in and day out all of you are there helping push my research forward as I help you better your understanding for yours. This research belongs just as much to you as it does to me. It is my hope that we can be proud of what we have accomplished, big and small, together. May our hard work in that small laboratory produce great changes for the scientific community.

## ACKNOWLEDGMENTS

I must first acknowledge the creator of the sciences, The Triune God. His ability to breathe science into existence and allowing us to explore and subdue it in manners known and unknown is what allows us to function as a society whether we acknowledge or deny His existence. Without His constant guidance and continual support, I could not have achieved such feats. Johanna Divina Reyes, my wife, I thank you. You have endured much in my quest for deeper knowledge, and I cannot seem to create the words to describe how amazing you are. You have been my hands and feet during this time of my life, feeding me, reminding me to relax, pushing me to my limits, and reminding me of my Savior. Johanna, I love you with all that I am, as imperfect as it may be sometimes. To my parents, Ismael and Rosa Reyes, your instruction in my upbringing is what has allowed me to stand in this time and place today. Just know, that God's promise to you for me is continually being fulfilled. This is only another portion of His blessing because of your faithfulness. To my brothers, Joshua and Jason Reyes, thanks for always reaching out to me. You guys have never stopped believing in me and I will try my hardest to do the same in return. To my extended family members, I thank you for always providing guidance and support. I cannot thank my entire family enough for their immense support system. To my family by law, our bond goes deeper than blood. You have all shown me what it means to acquire a higher education and to never stop pursuing the better character that awaits in the future. Don Juan, Doña Oneida, Oneida, Ana, Tito, Yahaira, Doña Divina, Anthony, Yahdel, and Delyah, thank you for constantly being there for me. You have all shown me that the past only serves to instruct you on a brighter future. Core Faith, you have been my safe haven and source of wisdom in these times. The philosophical portion of this doctorate was obtained in the boundaries of your ever-growing community's desire to know more of Christ.

# TABLE OF CONTENTS

LIST OF FIGURES .....	viii
LIST OF TABLES.....	xiii
LIST OF ACRONYMS (or) ABBREVIATIONS .....	xiv
CHAPTER ONE: THE DILEMA OF SOLVING NAVIER STOKES .....	1
CHAPTER TWO: INTRODUCTION TO LINE OF SIGHT FUEL-AIR .....	2
2.1 Background.....	2
2.2 The fuel-air measurement at pressure.....	3
2.3 The gap between local fuel-air and practical use.....	5
CHAPTER THREE: FUEL-AIR EXPERIMENTAL APPROACH.....	6
3.1 Facility Description .....	6
3.2 Facility Operation .....	8
3.3 Optical Diagnostics.....	10
3.4 Image Processing .....	15
3.5 Validation .....	16
CHAPTER FOUR: INTRODUCTION TO THREE-DIMENSIONAL VELOCITMETRY MEASUREMENTS .....	18
4.1 Background.....	18
4.2 Three-Dimensional Approaches .....	19
4.3 Tomographic PIV Drawbacks .....	20
4.4 Fiber Optic Technology .....	21
4.5 The Application of Fiber Optics to the Three-dimensional PIV Measurement.....	22
CHAPTER FIVE: FIBER OPTIC TOMOGRAPHIC PIV SYSTEM DESCRIPTION.....	23
5.1 Optical Setup .....	23

5.2 Fiber Bundle Characterization.....	25
5.3 System Calibration.....	27
CHAPTER SIX: VALIDATION EXPERIMENT FOR THE SINGLE CAMERA TOMOGRAPHIC SYSTEM .....	33
6.1 Experiment Description.....	33
6.2 Validation .....	35
CHAPTER SEVEN: FINDINGS FROM THE FUEL-AIR EXPERIMENT.....	39
7.1 Data Characterization .....	39
7.2 Creating the Calibration Map .....	44
CHAPTER EIGHT: TOMOGRAPHIC PIV FINDINGS .....	48
8.1 Air Jet.....	48
8.2 Confined Bluff Body Flow .....	53
CHAPTER NINE: COMBINING SPECIES IMAGING AND THREE-DIMENSIONAL PIV UTILIZING THE SINGLE SENSOR APPROACH .....	58
9.1 System description.....	58
9.2 Spatial Uncertainty .....	61
9.3 Light Transmittance.....	66
CHAPTER TEN: SIMULTANEOUS THREE-DIMENSIONAL CH* IMAGING AND PIV...	67
10.1 Experiment Description.....	67
10.2 Non-Reacting .....	69
10.3 Reacting .....	77
10.4 Capturing a Blow Off Event.....	85
CHAPTER 11: CONCLUSIONS.....	90
LIST OF REFERENCES.....	91



## LIST OF FIGURES

Figure 1: A.) Schematic of the pressure vessels with primary ports labeled. B.) Photograph of the experimental setup. ....	7
Figure 2: A.) Schematic of the control system for fuel injection. B.) Schematic of the ignition and data acquisition control system. ....	8
Figure 3: A.) Schematic breakdown of the optics used in the image splitting device and their orientation. B.) Optical orientation of the endoscope to image the flame kernel .....	13
Figure 4: a.) Target image. b.) Image of flame kernel. c.) Split image of $C_2^*$ . d.) Split image of $CH^*$ . e.) Initial image division. f.) Masked image. g.) The ratio of images after background subtraction, noise reduction, and mask application. ....	16
Figure 5: Comparison of the results obtained from the experimental hardware and optical components of a propane-air and methane-air. ....	17
Figure 6: Schematic of the single camera tomographic PIV imaging system with various components labeled. Shown on the left are various flow topologies that have been explored utilizing the single camera system. ....	24
Figure 7: Detailed view of the distal lens mounting orientation. ....	25
Figure 8: Normalized radial error of the distal lens and fiber leg at various standoff distances...	27
Figure 9: Schematic of the PIV laser diagnostic system. ....	31
Figure 10: Timing Schematic for the TPIV system .....	31
Figure 11: A. Schematic of the 2D target (3 planes shown). B. Image of the target acquired at $x=0$ mm. C. Image of the target acquired at $x=13$ mm. D. The projected volume (sum of views). ....	32

Figure 12: Schematic of the facility with the location of the imaging domain in A.) XY and B.) YZ, with the C.) tomographic data displayed in relation to hot wire and 2D PIV. .... 34

Figure 13: Mean axial velocity (along x axis) associated with the Hot wire and PIV measurements. Error bars denote deviation from the mean..... 36

Figure 14: Deviation of the PIV measurements from the hot wire velocity profile along the height of the measurement domain. .... 37

Figure 15: Mean span wise velocity (along z axis) associated with the stereoscopic and tomographic PIV measurements. .... 38

Figure 16: The initial 13 ms duration of the intensity ratio, laminar flame speed, and pressure.. 43

Figure 17: Various time steps of the intensity ratio for the different equivalence ratios acquired in the region of interest de-noted in Figure 16. .... 43

Figure 18: Correlation curve of the radical intensity ratio  $C_2^*/CH^*$  versus the equivalence ratio measured by oxygen sensor in the exhaust port for certified gasoline (99 % isooctane) at a charge pressure of atmosphere and initial temperature of 380 K. Points are averaged over 7 ms. .... 45

Figure 19: Correlation curves for charge pressures of atmosphere to 10 bar. .... 46

Figure 20: A.) Correlation curves from 1 to 10 bar at select equivalence ratios. B.) Correlation map of the intensity ratio as a function of equivalence ratio and charge pressure. .... 47

Figure 21: Image of the seeded air jet experiment, only corner imagers used to take data. .... 49

Figure 22: A. Raw image of flow field associated with the air jet experiment B. Lens location callout, only the four corner imagers are used to take the data..... 50

Figure 23: A. 3D mean axial velocity flow field from the seeded air jet data set with the stereo plane outlined by the dotted section B. extracted mean velocity profiles from the seeded air jet data for both 4D and stereo PIV at all x locations ..... 51

Figure 24: A. Mean Three-dimensional z-vorticity of the seeded air jet with the stereo result outlined by the dotted section B. Extracted vorticity profiles associated with the air jet compared to stereo PIV at all x locations. .... 52

Figure 25: Schematic of Confined Bluff body flow experiment. .... 54

Figure 26: A. Three-dimensional mean axial velocity B. Axial velocity acquired from 2D PIV taken in the same facility. .... 55

Figure 27: A. Mean Three-dimensional cross plane velocity data B. Cross plane velocity acquired from 2D PIV taken from the same facility..... 56

Figure 28: A. Mean Three-dimensional z-vorticity data B. Z-vorticity acquired from 2D PIV taken from the same facility..... 57

Figure 29: Schematic of the three-dimensional CH\* and PIV imaging system with key components labeled. High speed intensifier is not included in the diagram..... 60

Figure 30: Timing diagram for combined three-dimensional CH\* and PIV imaging ..... 60

Figure 31: Options for choosing fiber size magnification. A. Choosing scaling such that the fiber diameters is the size of the pixel diagonal. B. Choosing scaling such that the fiber diameter is the size of the pixel side (preferred). .... 65

Figure 32: Diagram of the VAG burner in all its glory. .... 68

Figure 33: Orientation of the experiment relative to the tomographic imaging system. .... 68

Figure 34: Mean axial velocity associated with the experiment. Outlined in grey are the nozzle exit and bluff body. .... 72

Figure 35: Mean axial Velocity profiles at various spanwise locations. A. An isometric view of the profiles plotted from  $z = -10$  to  $10$  mm. B. Side view of all the profiles plotted from  $z = 0$  to  $10$  mm. .... 72

Figure 36: A. Mean cross plane velocity at the centerline of the bluff body. B. Span wise velocity at the centerline of the bluff body. C. Span wise velocity after 100 MART iterations along the centerline of the bluff body..... 73

Figure 37: Combined mean velocity components. XY slice is  $V_x$ , the isosurface is of  $V_y$ , and the YZ slice is of  $V_z$ . ..... 74

Figure 38: Components of vorticity. A. about z, B. about x, and C. is about y ..... 75

Figure 39: Mean vorticity magnitude..... 76

Figure 40: Instantaneous snap shot of the vorticity magnitude colored by the z vorticity ..... 76

Figure 41: Instantaneous Snapshot of the  $CH^*$  species ..... 79

Figure 42: Mean  $CH^*$  tomographic reconstruction ..... 79

Figure 43: Mean cross plane vorticity at A. the centerline of the bluff body and B. the outer edge of the bluff body..... 80

Figure 44: Mean span wise vorticity at A. the centerline of the bluff body and B. at the outer edge of the bluff body ..... 81

Figure 45: Mean three-dimensional axial velocity profile, cross plane vorticity, and span wise vorticity overlaid from the PIV data. .... 82

Figure 46: Mean three-dimensional axial velocity overlaid with the mean of the  $CH^*$  measurement. .... 82

Figure 47: Mean three-dimensional cross plane vorticity overlaid with the mean  $CH^*$  intensity of the flame..... 83

Figure 48: Extracting the edge of the flame on an instantaneous snapshot overlaid with the vorticity field..... 83

Figure 49: 6 Instantaneous snapshots of a vortex wrinkling the flame..... 84

Figure 50: Instantaneous snapshot where the flame is beginning to produce flame holes. A. is the raw data and B. is the three-dimensional reconstruction. .... 86

Figure 51: Rotated view of Figure 50B overlaid with the cross-plane vorticity..... 87

Figure 52: Three-dimensional reconstruction of a flame hole associated with the blow off data. A. is the raw data and B. is the three-dimensional reconstruction overlaid with the vorticity ..... 88

Figure 53: Plotted isosurfaces of the vorticity field in Figure 52B to display the size of the vortex structures that are inducing this flame hole. .... 89

**LIST OF TABLES**

Table 1: Optical components used for the image splitter de-sign, with their specifications, and their application in the system. .... 14

Table 2: Light throughput (8-bit scale) for individual distal fibers..... 26

Table 3: Necessary components to perform tomographic PIV ..... 30

## LIST OF ACRONYMS (or) ABBREVIATIONS

CARBON DIOXIDE	$CO_2$
CARBON MONOXIDE	$CO$
CONSTANT VOLUME COMBUSTION CHAMBER	CVCC
DIATOMIC CARBON	$C_2$
DIRECT INJECTION	DI
ENGINE CONTROL UNIT	ECU
ENVIRONMENTAL PROTECTION AGENCY	EPA
EQUIVALENCE RATIO	$\Phi$
ETHYLENE	$C_2H_4$
FUEL TO AIR RATIO	FAR
HYDROXYL	$OH$
LASER DOPPLER VELOCIMETRY	LDV
METHANE	$CH_4$
METHYLIDYNE	$CH$
PARTICLE IMAGE VELOCIMETRY	PIV
PHASE DOPPLER ANEMOMETRY	PDA
PLANAR LASER INDUCED FLORESENCE	PLIF
PORT FUEL INJECTION	PFI
PROPANE	$C_3H_8$
RADICAL SPECIES	*
SPARK IGNITION	SI
TOMOGRAPHIC	TOMO

## CHAPTER ONE: THE DILEMA OF SOLVING NAVIER STOKES

$$\frac{\partial \rho}{\partial t} + \frac{\partial(\rho u)}{\partial x} + \frac{\partial(\rho v)}{\partial y} + \frac{\partial(\rho w)}{\partial z} = 0 \quad (1)$$

$$\frac{\partial(\rho u)}{\partial t} + \frac{\partial(\rho u^2)}{\partial x} + \frac{\partial(\rho uv)}{\partial y} + \frac{\partial(\rho uw)}{\partial z} = -\frac{\partial P}{\partial x} + \frac{1}{Re} \left( \frac{\partial \tau_{xx}}{\partial x} + \frac{\partial \tau_{xy}}{\partial y} + \frac{\partial \tau_{xz}}{\partial z} \right) \quad (2)$$

$$\frac{\partial(\rho v)}{\partial t} + \frac{\partial(\rho uv)}{\partial x} + \frac{\partial(\rho v^2)}{\partial y} + \frac{\partial(\rho vw)}{\partial z} = -\frac{\partial P}{\partial y} + \frac{1}{Re} \left( \frac{\partial \tau_{xy}}{\partial x} + \frac{\partial \tau_{yy}}{\partial y} + \frac{\partial \tau_{yz}}{\partial z} \right) \quad (3)$$

$$\frac{\partial(\rho w)}{\partial t} + \frac{\partial(\rho uw)}{\partial x} + \frac{\partial(\rho vw)}{\partial y} + \frac{\partial(\rho w^2)}{\partial z} = -\frac{\partial P}{\partial z} + \frac{1}{Re} \left( \frac{\partial \tau_{xz}}{\partial x} + \frac{\partial \tau_{yz}}{\partial y} + \frac{\partial \tau_{zz}}{\partial z} \right) \quad (4)$$

Above are the very well-known Navier-Stokes equations presented in a Eulerian format that together describe the motion of viscous fluid substances. It is not possible to solve them directly, unless either assumptions are made, or some previous information is known. Notice that the variables in question are density ( $\rho$ ), velocity ( $u, v, w$ ), pressure ( $P$ ), and stress ( $\tau$ ). Each variable is a function of space and time  $f(x, y, z, t)$ . We generally know our spatial domain ( $x, y$ , and  $z$ ) and the acquisition speed of your recording equipment will determine your time step,  $dt$ . The blanks left to fill are the 6 variables. To fill in these blanks experimentally usually requires expensive and complicated optical and experimental set ups. This means that only select few scientists with access to such equipment are able to perform these measurements, slowing down scientific progress. So, the question becomes, how can we make acquiring these measurements simpler so that smaller laboratories can help speed up our understanding of reacting flow fields. This can be done by minimizing the equipment required to take such exotic measurements and simplifying its approach. The proceeding chapters will explain a few methodologies of achieving this goal and demonstrating their capabilities. It is split into three main topics. Capturing species, capturing velocity, and combining the two approaches.



## CHAPTER TWO: INTRODUCTION TO LINE OF SIGHT FUEL-AIR

### 2.1 Background

This work starts off with the acquisition of the local fuel to air ratio and its determination at various pressures. If the chemistry of the fuel is known along with its ratio to air, the density ( $\rho$ ) can be back calculated for a reacting flow field solving for one variable of the N-S equations. The key is to do this spatially so that the calculations can be done on a local level.

The fuel to air ratio is the cornerstone of the energy release for any combustion application. With an increased understanding of the fuel-air delivery process, engines have evolved to become more efficient while producing more power [1]. Engineers striving to develop engines to meet ever increasing stringent emission requirements, need the necessary tools to assess the effectiveness of their fuel and air delivery designs [2]. Current methods of assessment use point based approaches, such as pressure, mass air flow, oxygen sensors, etc. to calculate the efficiency of the combustion process [3]. Though the use of these sensors is effective, engineers are turning to imaging techniques to study combustion efficiency. Flame imaging allows for the visualization of the temporal combustion processes spatially rather than a global measurement of the post combustion products [2], [4]–[7]. Though, straightforward luminescence imaging of a flame does not provide enough quantitative information of its characteristics. The deficiency can be remedied using chemiluminescence, in which only specific wavelengths associated with a combustion product are captured [8].

Clark [9] reported that the ratio of diatomic carbon ( $C_2^*$ ) and methyldiene ( $CH^*$ ) radiation intensities was found to be a good index of the equivalence ratio. He utilized a monochromator to isolate the radiations of the radical species associated with laminar propane-air and ethylene-

air flames that had a metered equivalence ratio. His results show that the intensity ratio ( $C_2^*/CH^*$ ) can be used as an indicator of local equivalence ratio as well as overall flame equivalence ratio, and that the resultant correlation is fuel specific [9]. Other researchers have utilized this technique as a method of detecting the equivalence ratio associated with steady flames. Cheng et al.[10] performed the technique utilizing a chemiluminescence imaging approach on partially premixed methane-air flames, and found that there is indeed a strong relation between the intensity ratio and the equivalence ratio. Furthermore, Cheng et al. [10] states that a correlation equation can be drawn from the data that correlate to the equivalence ratios of unregulated methane-air flame under the same conditions. Jeong et al. [8] performed a similar study documenting that there is an associated rich limit with the measurement for methane-air flames. They show that the measurement becomes insensitive to the equivalence ratio at about an equivalence ratio of 4 for methane-air flames.

## 2.2 The fuel-air measurement at pressure

The flames of the aforementioned studies are of steady, burner type flames exhausting to atmosphere. Flames associated with combustion chambers are unsteady, propagating flames that are subject to pressure rise. Jeon et al. [11] employs a constant volume combustion chamber to ignite a methane-air mixture at a range of 0.8 to 4 bar to record the development of the radical species associated with a propagating flame front. The research concludes that an equation to estimate the equivalence ratio can be derived for propagating flames at elevated pressures.

Sawada et al. [12] demonstrates the promise of this technique at high pressure combustion by igniting a propane-air mixture at various initial charge pressures up to 70 bar in a constant volume combustion chamber. The radical species intensity data is acquired using a

photomultiplier tube and shows that  $C_2^*$  is strongly influenced by the combustion pressure as compared to other species radicals [12]. Because of this, the inverse intensity ratio of  $C_2^*/CH^*$  proved to be more sensitive to the equivalence ratio in regions above an equivalence ratio of unity. This is due to the maximum luminous intensity of  $C_2^*$  shifting towards lean mixtures as combustion pressure is increased [12].

Chou et al. [13] recorded the radical intensities of  $C_2^*$  and  $CH^*$  of propane-air and indolene-air flames inside of a cylinder of an L-head engine. The engine was fixed to 1600 RPM and the fuel-air mixture was metered using carburetors and air intake valves. The radical intensities are recorded with photomultiplier tubes at various locations in the engine. A correlation curve was generated from the intensity ratio  $C_2^*/CH^*$  to the metered equivalence ratio for the two fuels using uniform fuel-air mixtures. The curve was then used to back calculate the equivalence ratio field of an inhomogeneous mixture with an average equivalence ratio of unity [13]. From their investigation, it was determined that the intensity ratio measurement is an accurate diagnostic technique for understanding the fuel-air field associated with internal combustion engines. More recently, this technique has been performed utilizing a chemiluminescence imaging approach on an optically accessible 548 cc four-stroke engine, utilizing gasoline port injection by Ikeda et al. [14]. The engine was fixed to 1200 RPM, and the chemiluminescence intensities were recorded using custom Cassegrain optics and compared to the air-fuel ratio measured by an oxygen sensor in the exhaust port. It was concluded that the comparison of the intensity ratio to the fuel-air ratio measured by the oxygen sensor provides accurate results in formulating a correlation curve.

### 2.3 The gap between local fuel-air and practical use

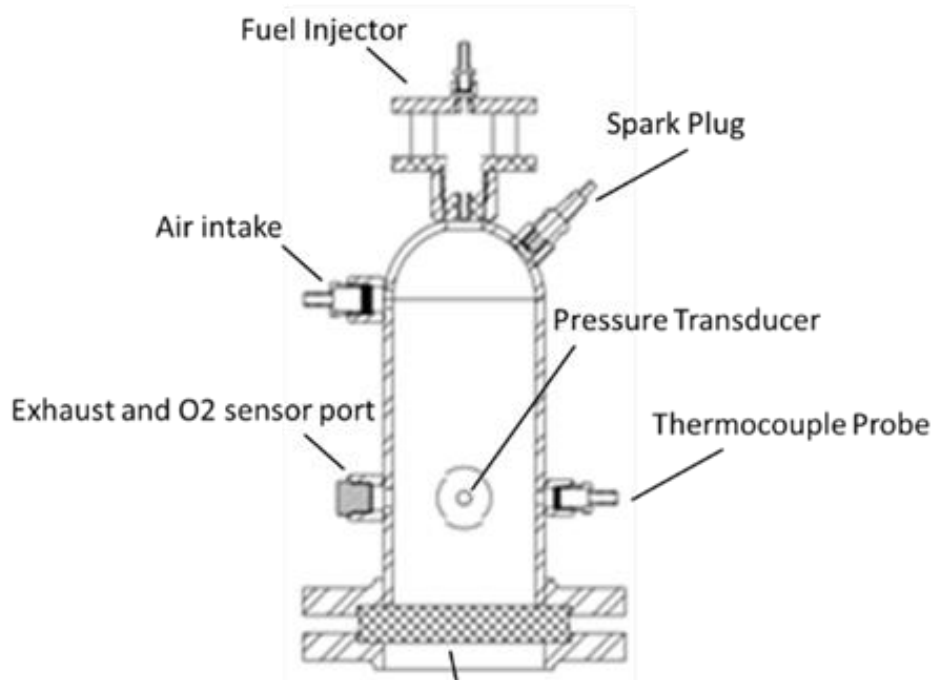
The measurement is therefore practical, but the data presented in the aforementioned studies display results for a single load condition and produce a single correlation curve. If this technique is to be applied to an engine, its behavior must be characterized considering the various parameters that effect the chemiluminescence intensity of the radical species. Known parameters that effect the chemiluminescence intensity of radical species associated with a flame are fuel composition [9], [13] equivalence ratio [9], [11]–[13], [15] temperature [15]–[17], and pressure [18]–[20].

The scope of this work is concerned with the effects of the initial pressure on the intensity ratio measurement of gasoline-air mixtures. The goal is to demonstrate that it is possible to generate a correlation map of the intensity to equivalence ratio for gasoline (a commonly utilized liquid fuel) at relatively high pressures. This allows for the detection of the local spatial and temporal equivalence ratio at the flame and can aid engineers in improving the efficiency of the combustion process in engines, where premixing is not as well characterized. The experiment is not meant to simulate an engine, but instead is used as a controlled approach for acquiring intensity data. The study measured the radical intensities of  $C_2^*$  and  $CH^*$  in a short time span from the point of ignition, while maintaining the initial temperature constant for all cases. The time span is chosen such that there is negligible pressure rise in the window of observation. The current study is conducted at initial charge pressures of 1 to 10 bar, limited by the air supply. The data presented demonstrates the capability of this technique and its potential expansion to higher loads.

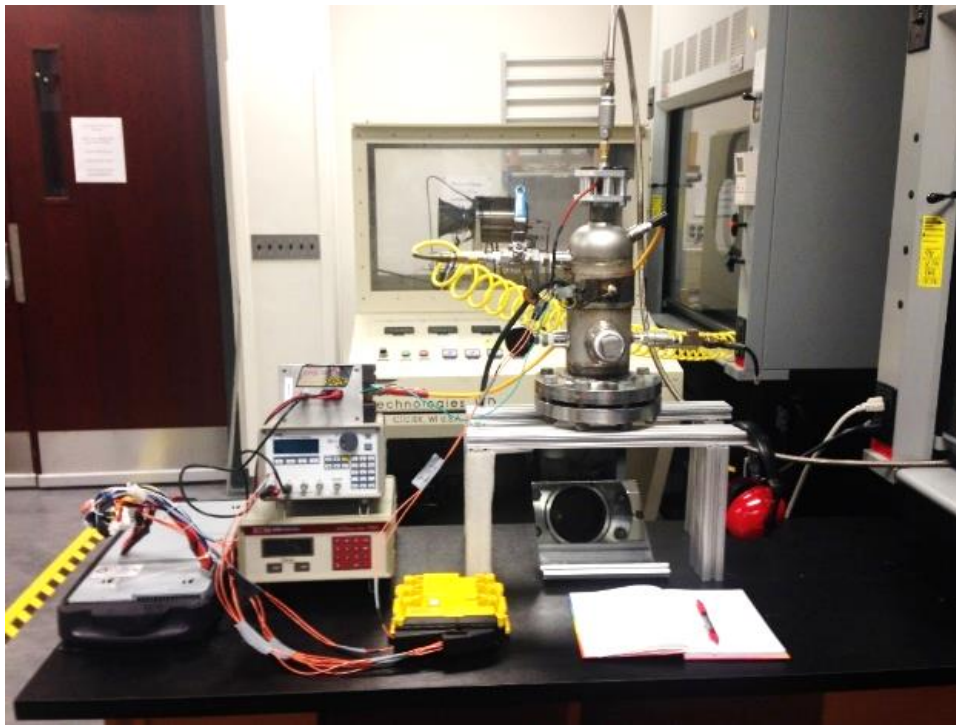
## CHAPTER THREE: FUEL-AIR EXPERIMENTAL APPROACH

### 3.1 Facility Description

A pressure vessel with multiple access ports was used to acquire chemiluminescence data. The facility has a total volume of 2 liters and is capable of handling pressures over 200 bar. The facility has been tested in temperatures up to 600 K and is optically accessible. The facility is instrumented with a Piezo Electric Pressure sensor. The pressure sensor is capable of handling pressures above 200 bar and is highly sensitive and accurate ( $\pm 0.2$  bar). A K type thermocouple that is accurate up to 1000 K with a 0.75 percent error in measurement is oriented inside the chamber with the end of the probe about 2 mm from the chamber interior wall to measure the internal gas temperature. A platinum four prong spark plug is used for the ignition process. An oxygen sensor is mounted to the facility exhaust line to measure the equivalence ratio of the exhaust gases respectively. A high-pressure fuel injector with a multi-point spray cone was used to inject gasoline. The fuel had a composition mixture of 99 % iso-octane and 0.9 % n-heptane. The manufacturer of the injector ensures atomization of gasoline with droplet size on the order of 5 microns, and 10 mg of gasoline injected per pulse at a pulse width of 1.6 ms and fuel pressure of 100 bar. Pressurized air is injected through an intake port with a 0.25-inch inner diameter. Air, fuel injection, ignition, and data acquisition timing parameters were set using a delay generator capable of picosecond accuracy in conjunction with a data acquisition and control program to acquire the data. A schematic of the facility and an image of the experimental set up can be seen in Figure 1. A block diagram of the fuel injection and data acquisition systems can be seen in Figure 2.



A.)



B.)

Figure 1: A.) Schematic of the pressure vessels with primary ports labeled. B.) Photograph of the experimental setup.

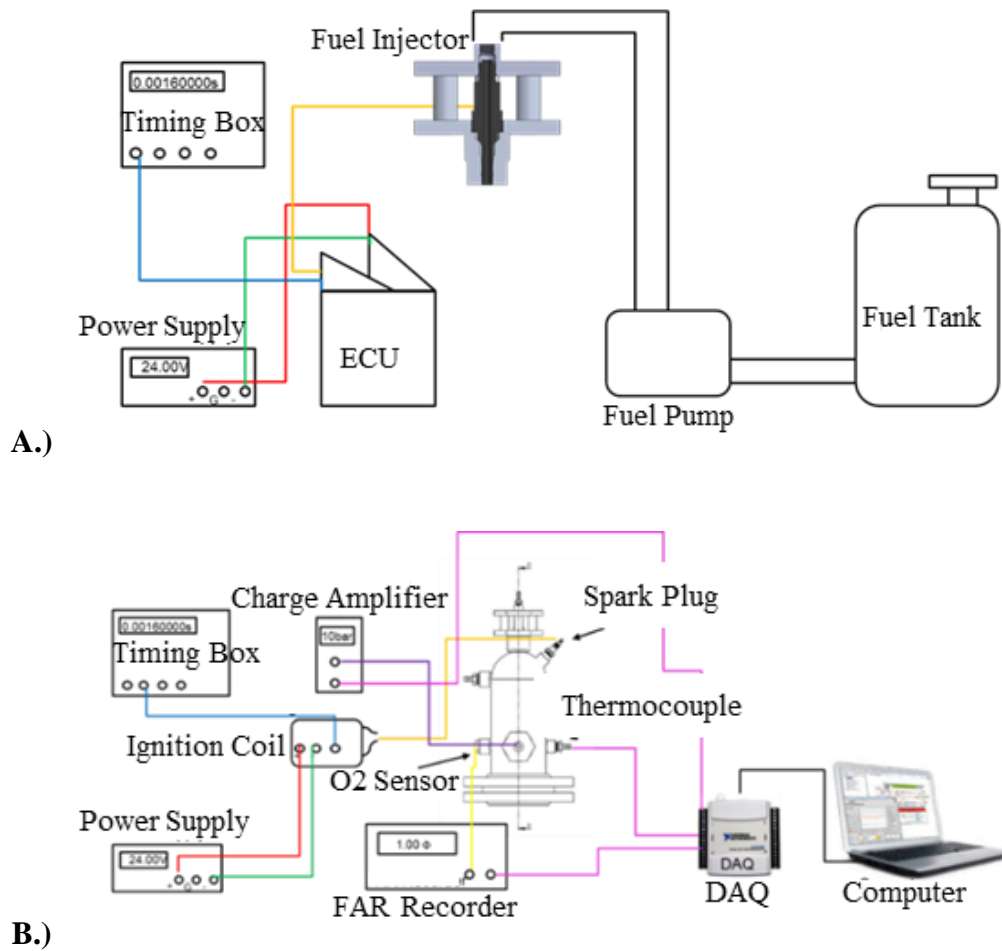


Figure 2: A.) Schematic of the control system for fuel injection. B.) Schematic of the ignition and data acquisition control system.

### 3.2 Facility Operation

The chamber is first preheated to an internal temperature of 380 K. The initial temperature is maintained constant for all cases associated with this work as the effects of the initial temperature are not explored in this study. The mixing process in the chamber begins with the opening of the exhaust port and allowing air to flow through the facility for 5 minutes to help evacuate the chamber completely and generate the necessary turbulence for mixing. The exhaust port is then closed, and air and fuel are injected simultaneously until the desired charge pressure

is achieved. The amount of fuel injected is changed by increasing or decreasing the number of injector pulses.

Fuel injection velocities ( $v_{fuel}$ ) are determined using equation 5, which is a simple one-dimensional Bernoulli's calculation assuming the initial chamber fluid velocity just behind the injection point is at zero,  $\Delta P_{fuel}$  is the pressures difference between the injection pressure and the chamber, and  $\rho_{fuel}$  is the density of the fuel being injected. The air injection velocity ( $v_{air}$ ) was determined using equation 6, where  $q_{air}$  is the volumetric flowrate, and  $d_{air\ inj}$  is the inner diameter of the air injection port.

$$v_{fuel} = \left( \frac{2 * \Delta P_{fuel}}{\rho_{fuel}} \right)^{\frac{1}{2}} \quad (5)$$

$$v_{air} = \frac{4 * q_{air}}{\pi * d_{air\ inj}^2} \quad (6)$$

The injection pressure of the air and fuel were held constant by two air driven liquid/air pumps and were 10 bar and 100 bar respectively. The volumetric flow rate ( $q_{air}$ ) seen by the air pump associated with the air injector was rated at 7 cfm. This resulted in an air injection velocity of 100 m/s and a fuel injection velocity of 110 m/s. The error associated with the pressure and density calculation of the fuel is  $\pm 0.2$  bar and  $\pm 30 \text{ kg/m}^3$  which results in a velocity uncertainty of  $\pm 5$  m/s calculated using a propagation of error analysis. The same approach is done for the air injection velocity equation with the manufacture uncertainty of the air pump's flowrate being  $\pm 0.2$  cfm and the uncertainty of the inner diameter of the air intake port being  $\pm 0.01$  inches; this results in an uncertainty of  $\pm 6$  m/s in air velocity.



The fuel-air ratio is metered by calculating the amount of required gasoline needed to arrive at the desired equivalence ratio for the quantity of pressurized air in the chamber. The total required gasoline content is divided by the quantity of fuel injected per pulse (10 mg per pulse) to arrive at the number of required injection pulses. To benchmark the homogenous fuel-air mixture and consistency in the mixing process, a series of 10 tests were conducted at metered equivalence ratios of  $\phi = 0.7$ ,  $\phi = 1.0$ , and  $\phi = 1.2$  (30 tests in total). Initial charge pressure was held at atmosphere with an internal temperature of 380 K before ignition for all cases. Fuel and air were systematically injected to mix together until the desired metered equivalence ratio was achieved, and the mixture was ignited by the automotive spark plug. The mixture was then immediately exhausted, and the equivalence ratio was measured by the oxygen sensor mounted to the exhaust port. The gases were exhausted over the oxygen sensor for one minute, in which the fuel air ratio data was recorded at 1 kHz. The corresponding measured equivalence ratios are  $0.71 \pm 0.05$ ,  $0.98 \pm 0.05$ , and  $1.22 \pm 0.07$  respectively. This deviation was calculated by taking the oxygen sensors readout of the exhaust gases over the ten tests, reporting the standard deviation from the mean of the recorded values, and including the oxygen sensor uncertainty of  $\pm 0.01$  of the equivalence ratio into a propagation of error analysis. The recorded equivalence ratio from the oxygen sensor is in good agreement with the flow-based calculation of the equivalence ratio with a max disparity of 0.09. The above testing ensured confidence in the homogeneity of the mixtures produced in the facility since the oxygen sensor readout was nominally constant over the minute of acquisition time.

### 3.3 Optical Diagnostics

The optical components are encased in a rigid housing which minimizes movement. The specifications of the optical components are listed in Table 1 and a schematic of the optical set

up can be seen in Figure 3. The optical path includes: an endoscope, a focusing lens, a relay lens coupled with an angle spaced aperture to allow for magnification of the image, a collimating lens, dichroic mirrors that allows the  $C_2^*$  bandwidth to pass and reflects the  $CH^*$  bandwidth, a filter in one channel for the  $CH^*$  emissive peak, a filter in a second channel for the  $C_2^*$  emissive peak, steering mirrors allowing for alignment of the filtered split light beams onto the image sensor, and a collection lens to focus the images onto an intensifier coupled high speed camera. This approach sacrifices image resolution but allows for the simultaneous capture of  $C_2^*$  and  $CH^*$  on the same sensor.

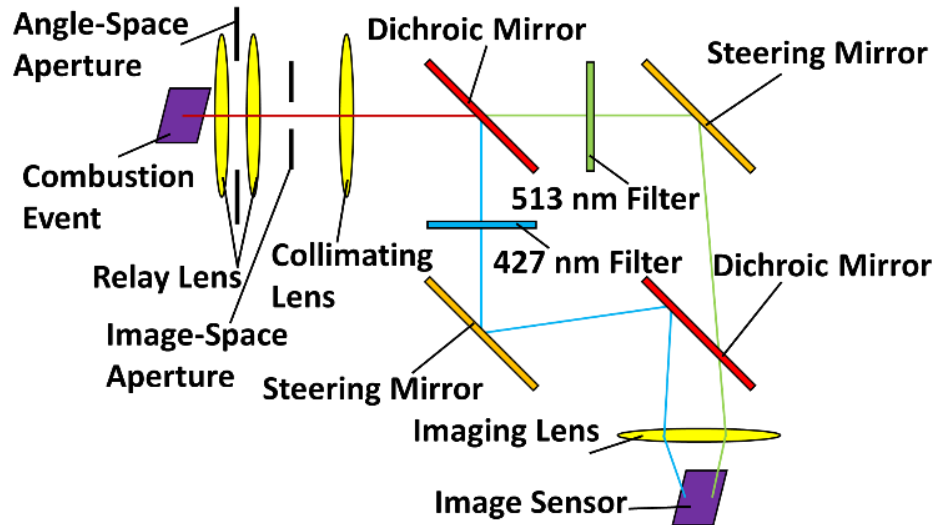
The data was acquired by recording the flame associated with the initial flame kernel. As such, the spark plug was oriented directly across from the distal end of the optical setup.

Theoretical light transmittance in percentage,  $\sigma$ , of the optical system is calculated for the two wavelengths using equation 7, where  $\eta$  is the relative amount of light transmitted by the optical component and  $s$  is the image sensors relative sensitivity to a wavelength.

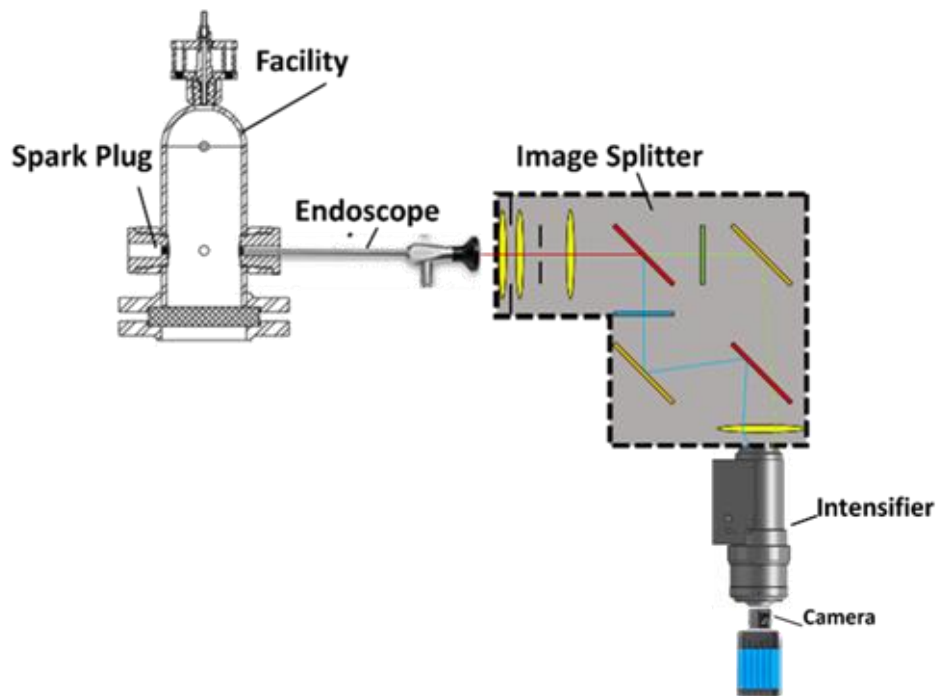
$$\sigma_{\lambda} = 100 * \eta_{endo} * \eta_{DM}(\lambda)^2 * \eta_{BanPass}(\lambda) * s_{\lambda} \quad (7)$$

This returns a transmittance percentage of  $30 \pm 7\%$  for the 427 nm wavelength and  $48 \pm 12\%$  for the 513 nm wavelength. To ensure image capture at high speed, the intensifier is used. The gain on the intensifier is fixed for all experimental conditions. The uncertainty was calculated using the manufactures reported uncertainty and a propagation of error approach. The 427 nm wavelength suffers a heavier loss due to the image sensors sensitivity in that range (as noted in Table 1). This disparity is accounted for by digitally intensifying the recorded images of the 427 nm wavelength by a factor of 1.6, the ratio of the spectral sensitivity at 513 nm to the spectral sensitivity at 427 nm. This factor is independent of equivalence ratio and pressure; it is only

affected by the optical sensitivity to light at the wavelengths of interest. Any effects to light throughput by the equivalence ratio and pressure are used in producing the correlation.



A.)



B.)

Figure 3: A.) Schematic breakdown of the optics used in the image splitting device and their orientation. B.) Optical orientation of the endoscope to image the flame kernel

Table 1: Optical components used for the image splitter de-sign, with their specifications, and their application in the system.

<b>Optical Component</b>	<b>Specification</b>	<b>Application</b>
Dichroic Mirror	98 % Transmission $\lambda > 484$ nm 98 % Reflectance $\lambda < 484$ nm	To direct light onto the image sensor of camera
Bandpass Filter	95 % Transmission $505 < \lambda < 522$ nm	Viewing $C_2^*$ bandwidth
Bandpass Filter	95 % Transmission $422 < \lambda < 432$ nm	Viewing $CH^*$ bandwidth
Image Intensifier	25 mm sensor size dual stage GEN II S20 200 – 900 nm spectral response	Capturing the intensified split light signals from a combustion event
Image Sensor	CMOS 1024x1024 pix 20 $\mu$ m square pixel size Sensitivity peak at 680 nm Relative spectral response: 40 % of peak value at 427 nm 65 % of peak value at 513 nm	

### 3.4 Image Processing

A target image is used to ensure that there is a proper pixel to pixel comparison between the two wavelength images. The camera and optics are then oriented with respect to the facility as displayed in figure 3. The camera is set to capture at 3,000 FPS with an exposure of 3.33  $\mu\text{s}$  and begins recording 2  $\mu\text{s}$  before ignition. The mixture is ignited, and the combustion event is captured as two split images on the image sensor. The split images have a spatial resolution of 154  $\mu\text{m}$  per pixel.

The target image is used to create the crop regions for the split images. Patterns detected on one side of the target image are searched for on the other side and matched to generate a pixel-pair matrix. The created crop regions are applied to the respected wavelength images to create two separate images for use in intensity ratio calculations.

The intensity values of the images are used to extract the radical intensity ratio. Dividing the  $C_2^*$  image's intensity values by the digitally scaled  $CH^*$  intensity values yields the intensity ratio field for a specific frame. This division can produce unwanted noise due to the possible divisions by zero, division by the noise level of the image sensor, or division by any possible background noise. Techniques such as background subtraction, adaptive masking, noise reduction, and nonzero division algorithms are employed to reduce any inclusion of noise. A breakdown of the process is described in Figure 4 where the technique is applied to a gasoline-air mixture at an equivalence ratio of unity. This process is repeated for all frames of a recording and for various equivalence ratios. Finally, the intensity ratios are plotted against the equivalence ratio measured by the oxygen sensor to obtain a correlation curve. This process is used to calculate the intensity ratio ( $C_2^*/CH^*$ ) at charge pressures of 1,3,5,7, and 10 bar.

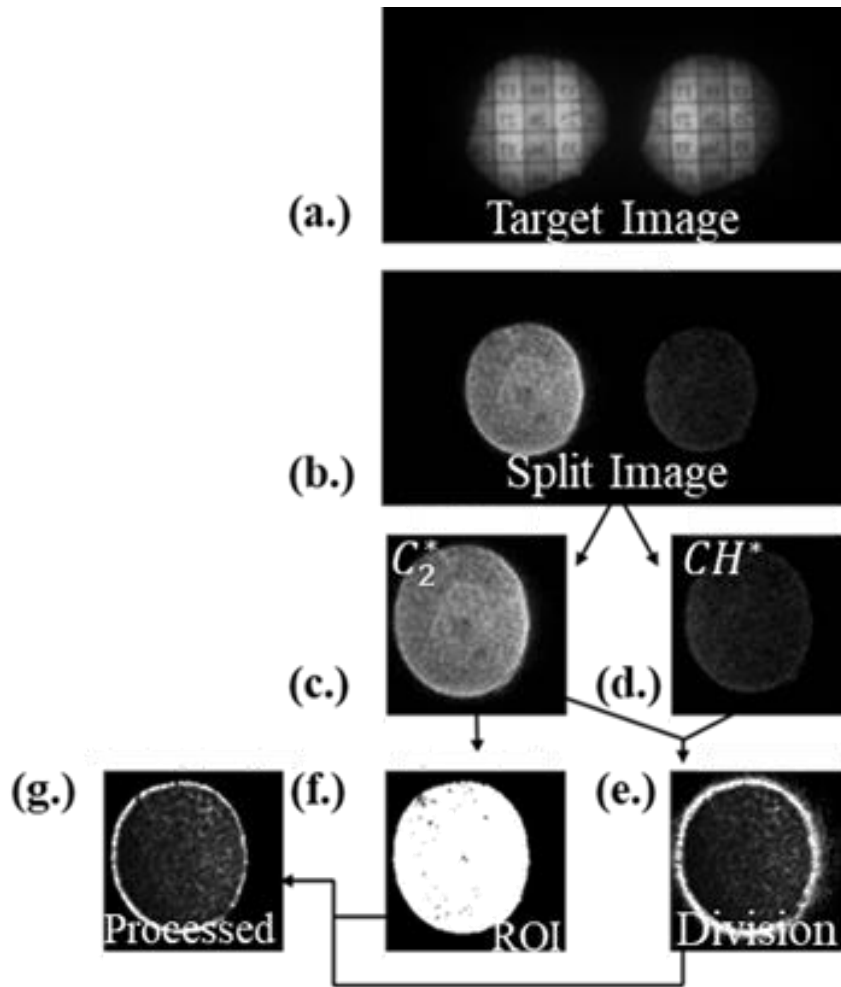


Figure 4: a.) Target image. b.) Image of flame kernel. c.) Split image of  $C_2^*$ . d.) Split image of  $CH^*$ . e.) Initial image division. f.) Masked image. g.) The ratio of images after background subtraction, noise reduction, and mask application.

### 3.5 Validation

Validation of the experimental setup was first performed by investigating methane-air and propane-air flames. The intensity ratios were calculated by recording the split wavelength images associated with a steady flame produced from a natural gas burner. The fuel to air ratio for the validation experiment was controlled using flow meters with a resolution of 0.1 SCFH.

The fuel and air mix-ture was stabilized using a natural gas burner with a 12 mm diameter circular exit plane. The split images of the flames were processed, and the intensity ratios recorded. This was plotted and compared to findings by Clark [9] and Jeong et al. [8] to validate the setup and the methodology employed. In comparison the burner used by Clark [9] and Jeong et al. [8] utilized burner diameters of 10 mm and 8 mm respectively. 20 images were taken at each equivalence ratio point and used to acquire the average of the intensity ratio at that location utilizing the proposed image processing technique. The results of the comparison test can be seen in Figure 5. The test show that the optical setup produces results comparable to what has been seen in previous studies.

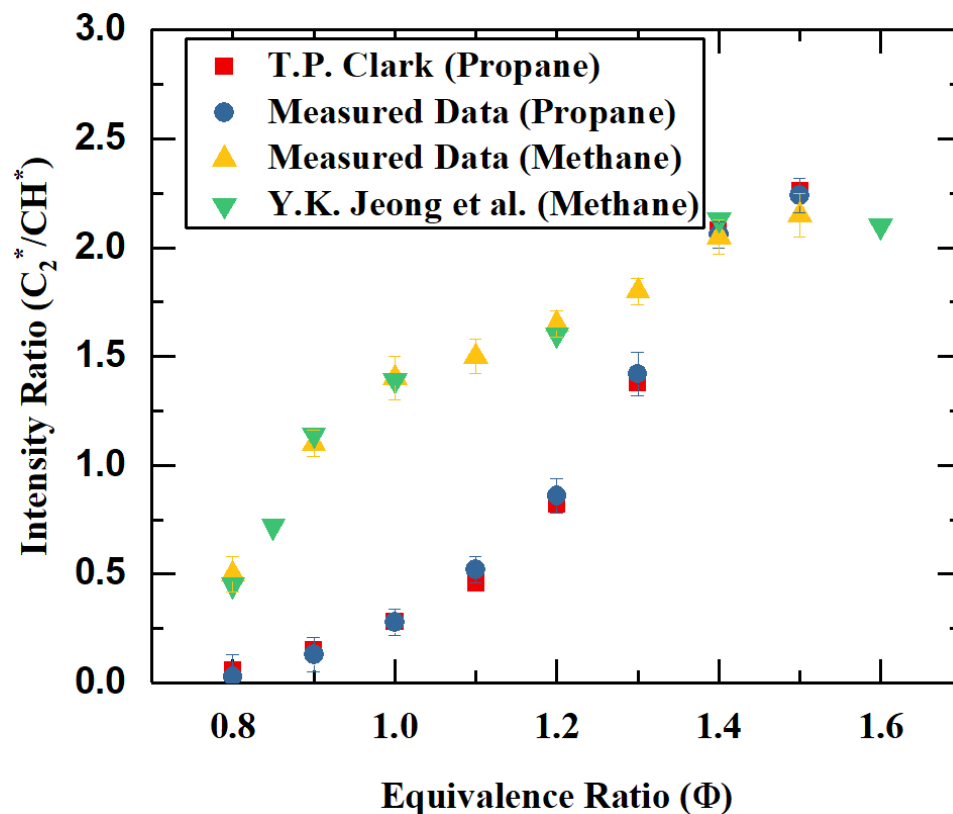


Figure 5: Comparison of the results obtained from the experimental hardware and optical components of a propane-air and methane-air.



## CHAPTER FOUR: INTRODUCTION TO THREE-DIMENSIONAL VELOCITMETRY MEASUREMENTS

### 4.1 Background

Now that a simple method of acquiring the fuel-air field on one sensor has been established (and in turn a method of back calculating the density), we will move on to filling a few more blanks in the Navier-Stokes equations, namely,  $u$ ,  $v$ , and  $w$ .

The instantaneous structures associated with turbulence is a fundamental aspect of fluids that is more often assumed than described. To describe such phenomena, a three-dimensional approach to capturing the flow-field information is a requirement rather than a luxury. Three-dimensional flows have been investigated with the use of particle image velocimetry (PIV) because of its ability to quantify flow field information both spatially and temporally. By illuminating particles in a seeded flow with a planar light source and capturing the behavior with the use of a high-speed image sensor, it is possible to describe flow field behavior in terms of velocimetric information in the field of view (FOV) of the sensor. The approach is two-dimensional in nature and is inherently incapable of describing complex three-dimensional flows. By applying a stereoscopic approach to the planar technique it is possible to acquire the third component of the velocity [22], [23]. The depth to which this can be calculated is limited to the planar nature of the light source classifying the technique as two-dimensional. Work has been done to expand stereoscopic PIV (stereo-PIV) to include more information in the third dimension with the addition of a secondary plan (dual plane stereo-PIV) [24], [25]. The complete velocity tensor is evaluated over the two planar domains but proves to be insufficient for the study of resolving information that occurs over a larger space [26]. To describe the behaviors associated with complex three-dimensional flow fields, the afore mentioned PIV techniques rely

heavily on two-dimensional statistical information and a good deal of assumptions to arrive at a conclusion. Because of this, temporal evolution is not captured and can only be observed by uncorrelated planar frames.

In an attempt to describe turbulence physics, scientist and engineers have turned to computational approaches. Techniques such as direct numerical simulation (DNS) and large eddy simulation (LES) are capable of supplying complete descriptions of flow structures, specifically those associated with turbulence [26]–[28]. The benefit being that the computational approach is both cost effective and requires less labor force than experimentation. Computational models have since exceeded the information gathered experimentally on turbulence physics. This leap in information has created a need for validation of models by means of physical data acquisition. Simply, there is a need for experimentation to expand its three-dimensional data acquisition capabilities to ensure accuracy of current turbulence physics models.

#### 4.2 Three-Dimensional Approaches

Among the many approaches to remedy this need are most notably three-dimensional particle tracking velocimetry (3D PTV), scanning light sheet PIV (SLS), and holographic PIV [29]–[33]. 3D PTV has been used to study particle motion in a Lagrangian reference frame as a means of describing turbulence using either of the digital focusing PIV or photogrammetric PIV techniques. Either approach suffers from the lack of adequate temporal resolution and relies on statistical descriptions of the flow-field [34], [35]. The SLS approach achieves great spatial resolution and is able to capture information relating to patterns associated with transitional flows [26]. The drawback of the technique is that it is only utilizable for lower velocity flows, typically under 1 m/s [32], [36], [37]. Holographic PIV approaches the measurement by

utilizing photographic plates as a recording medium to capture three-dimensional information. It is capable of capturing instantaneous information, but because of the optical limitations it is only capable of small measurement volumes on the order of cubic millimeters [30], [38], [39]. The spatial limitations of such a measurement make it unsuitable for turbulence characterization in most cases.

Tomographic PIV (tomo-PIV) is a technique that makes use of simultaneous views of particles illuminated using a volume of light to perform a three-dimensional reconstruction of the flow field as a light intensity distribution by means of optical tomography [40]. The approach results in tomogram pairs from which three-dimensional cross correlation algorithms are employed to return a three-component velocity vector distribution [40]. If high-speed image sensors are used, then it is possible to acquire temporally resolved three-dimensional flow-field information. Tomo-PIV, since its introduction, has demonstrated capabilities in the acquisition of temporal information of the complete velocity tensor associated with complex flow fields [41], [42]. It allows for inspection of volume domains utilizable for the study of unsteady three-dimensional flows and has been shown to be an accurate means of extracting three-dimensional flow field data [26]–[28], [40]–[43].

#### 4.3 Tomographic PIV Drawbacks

Tomo-PIV is not without its limitations. The technique requires a good deal of optical accessibility and is mainly utilized for visualization of unconfined flows or large optical test sections. Because high-speed cameras are usually large and bulky, the optical layout either requires that the cameras be spread far apart on separate mounts or that a large optical rig be designed to orient the cameras. The amount of recording equipment requires that there be a more

complex timing, control, and monitoring system. The amount of data saved is quite large and can pose storage issues. Finally, the four-dimensional (temporally resolved, three-dimensional) technique is inaccessible to most laboratories due to its cost and complexity. The lack of optical versatility hinders laboratories that mainly deal with confined flows and smaller experiments from applying the technique. High-speed cameras are necessary to perform four-dimensional tomographic PIV. The purchase of four or more is often unrealistic for most laboratories forcing them to resort to traditional planar methods to acquire data. If the technique is to be used to further the study of turbulence physics, steps towards making the technology more accessible and versatile must be made.

#### 4.4 Fiber Optic Technology

Imaging using fiber optics is an approach that is used in many industries to acquire images where space is limited. Fiber bundles act as a flexible light relay and can cover distances of up to several meters [44]. The technology has mainly been used in biomedical, spectroscopy, and photochemistry applications [45]–[48]. More recently, the technology has been expanded to use on flow visualization studies. The approach allows for cameras to be placed in a convenient location, allowing the fiber bundle to relay the information of the desired domain [49]. If multiple fiber bundles are coupled it is possible to view multiple angles simultaneously from one image sensor by essentially splitting an image sensor into quadrants. Individual image resolution is sacrificed with the added benefit of reduced cost and space. The approach has been utilized to perform tomographic reconstruction of flames utilizing species luminescence and has been shown to produce accurate results [50], [51]. Thus, the use of fiber bundle technology proves useful in reducing the cost, complexity, and overall size of a tomo-PIV system, the drawback being a reduction of image resolution.

#### 4.5 The Application of Fiber Optics to the Three-dimensional PIV Measurement

This work applies the reduced resolution fiber bundle approach to the tomographic PIV technique. Tomo-PIV is heavily reliant on image resolution to acquire accurate, quantifiable three-dimensional information. Thus, it is imperative that the proposed reduced resolution tomo-PIV technique be characterized and scrutinized in comparison to traditional PIV measurements on well understood flows. High speed cameras are used to demonstrate the four-dimensional capabilities of the proposed system. This approach to tomo-PIV can make the technique more accessible to the fluid sciences community and help accelerate understanding of turbulent physics.

# CHAPTER FIVE: FIBER OPTIC TOMOGRAPHIC PIV SYSTEM DESCRIPTION

## 5.1 Optical Setup

Figure 6 displays a schematic of the tomographic PIV system. The system consists of a fiber bundle that is split into 4 separate fiber legs, a high-speed camera, a dual head Nd:YAG laser, a timing box, and associated software for control and data acquisition. The fiber bundle is made up of 1,016,064 individual fibers (1,008 x 1,008 array). Each individual fiber is 10  $\mu\text{m}$ , forming a 10 x 10 mm fiber bundle sensor. The bundle is then separated into four 5 x 5 mm equal fiber sub-bundles for imaging, as shown in Figure 6. The fiber to camera coupling end is denoted as the proximal end, whereas the free imaging ends are denoted as the distal ends. The proximal end is coupled to the high-speed camera via a relay lens that is sealed from ambient light. The distal fiber ends are arranged on a rigid optical setup that measures 610mm in width and 508 mm in height and are equipped with multiangle stages for each bundle. This decouples the distal ends of the fiber bundle to satisfy the scheimpflug criterion by keeping the objective lenses stationary and rotating the distal end of the fibers. Each objective lens (distal lens) has a focal length of 50 mm with a minimum aperture size of  $f/2$ . For data acquisition the aperture was reduced to allow the entire measurement volume to remain in focus. The objective lenses are mounted in the manner shown in Figure 7. The lenses are mounted where  $\theta$  is 22.5 degrees and  $\phi$  is 22.5 degrees. The mounts for the distal ends are vertically translatable to allow for adjustment of the standoff distance,  $d$ .

The high-speed camera (Photron SA-Z) is equipped with a one megapixel (1,024 x 1,024) square CMOS sensor. The camera can capture 20,000 frames per second at full resolution with a 150 ns inter-frame time. The overall physical area of the image sensor is 20 x 20 mm. The 10 x

10 mm proximal end of the fiber is magnified by a factor of 2, to ensure an approximate 1:1 fiber to pixel ratio. Magnification is achieved by mounting a relay lens to the proximal fiber end opposed to the lens on the high-speed camera, with a two to one ratio in their respective focal lengths (see Figure 6). The larger focal length (Nikon 50 mm f/1.2) on the camera and the lower focal length (Zeiss 25 mm f/2) on the proximal end of the bundle. The approach allows for a total inspection volume of 37.5 x 37.5 x 25 mm at 0.25 megapixel (MP) individual image resolution with a 61  $\mu\text{m}$  per pixel spatial resolution. A dual pulsed Nd:YAG laser (Lee Laser LDP-200MQG DUAL) is used to illuminate the inspection volume. Each head of the Nd:YAG laser is capable of producing a 12 mJ, 4 mm diameter beam at a repetition rate of 10,000 Hz. This provides sufficient light throughput into the tomo-PIV system and adequate temporal resolution. A timing box that allows for picosecond accuracy, acts as the external clock for both the laser and camera to ensure synchronization of the PIV measurement.

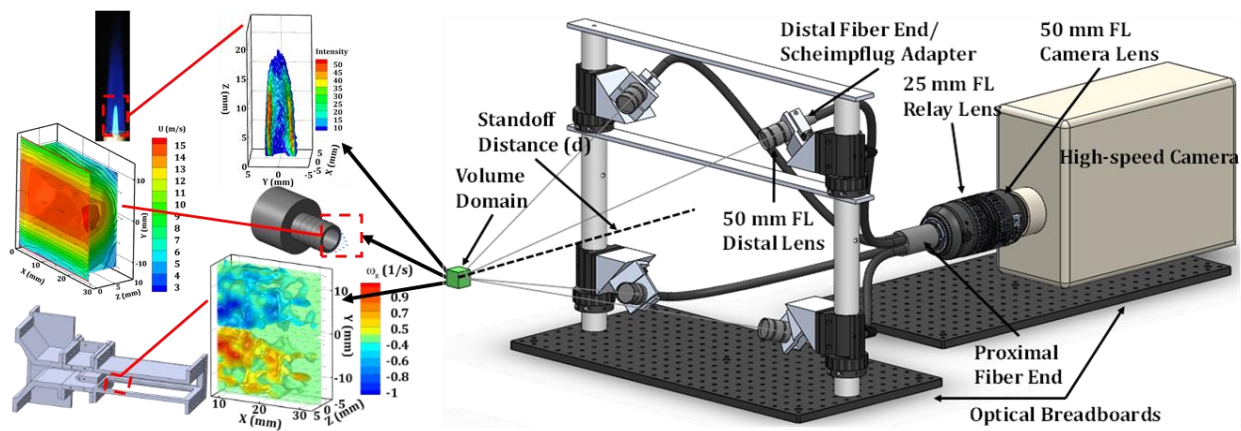


Figure 6: Schematic of the single camera tomographic PIV imaging system with various components labeled. Shown on the left are various flow topologies that have been explored utilizing the single camera system.

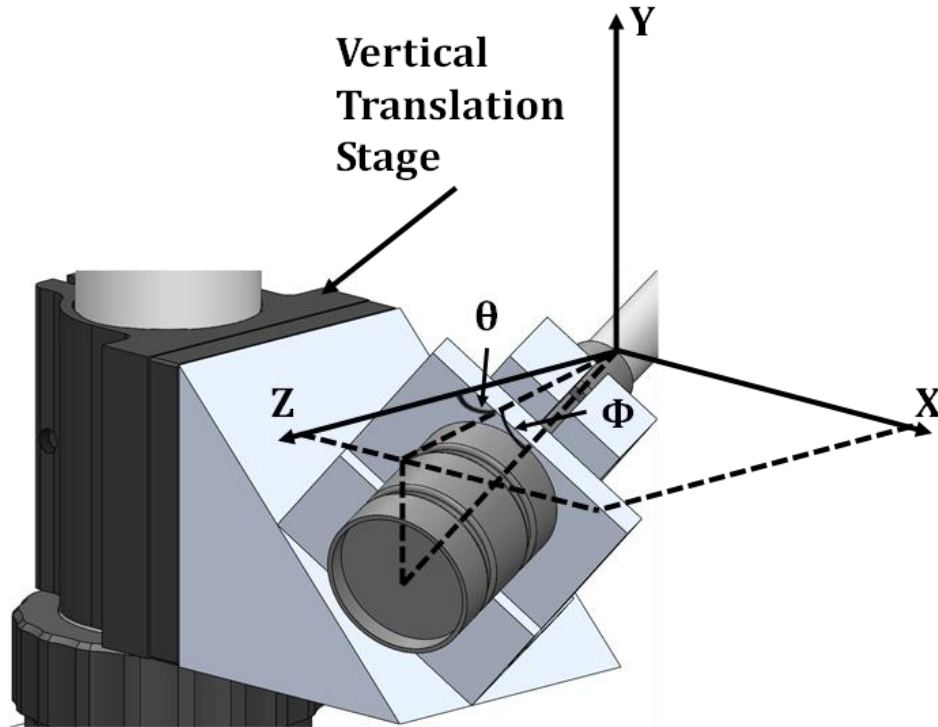


Figure 7: Detailed view of the distal lens mounting orientation.

## 5.2 Fiber Bundle Characterization

A modular light source with a white back lit panel was used to ensure that images produced from each distal end capture uniform and similar light intensity distributions. The back lit panel produces a uniform light field in which the intensity is recorded from each distal end individually at various light source input voltages [50]. A distal end was mounted so that it was parallel to the back lit panel, 1000 images were captured at various light source intensities, and the mean taken for comparison. The results are tabulated in Table 2. The test returned a maximum difference of 2 in recorded intensity between any distal end with a deviation across an image area for any given end being less than 3.0%. This demonstrates that the distal ends have similar light throughput characteristics between each other and across their respective fiber grids. Radial distortion effects from the distal lens were assessed by placing a gridded target in the



center of the distal lens array at various standoff distances [51]. The radii of the images were computed from the center of the target. The normalized error is reported in Figure 8 for the various standoff distances. At the targeted standoff distance of 350 mm the normalized radial error is below 3.0%.

Table 2: Light throughput (8-bit scale) for individual distal fibers.

Light Source Voltage Input	Mean Gray Intensity Values							
	Fiber	Fiber	Fiber	Fiber	Fiber	Fiber	Fiber	Fiber
	1	2	3	4	5	6	7	8
1.00	13	14	12	13	13	12	12	12
2.00	82	80	81	81	81	81	80	82
3.00	199	198	200	199	198	200	199	199
4.00	211	210	212	211	210	211	211	212
5.00	224	223	224	224	224	224	222	223

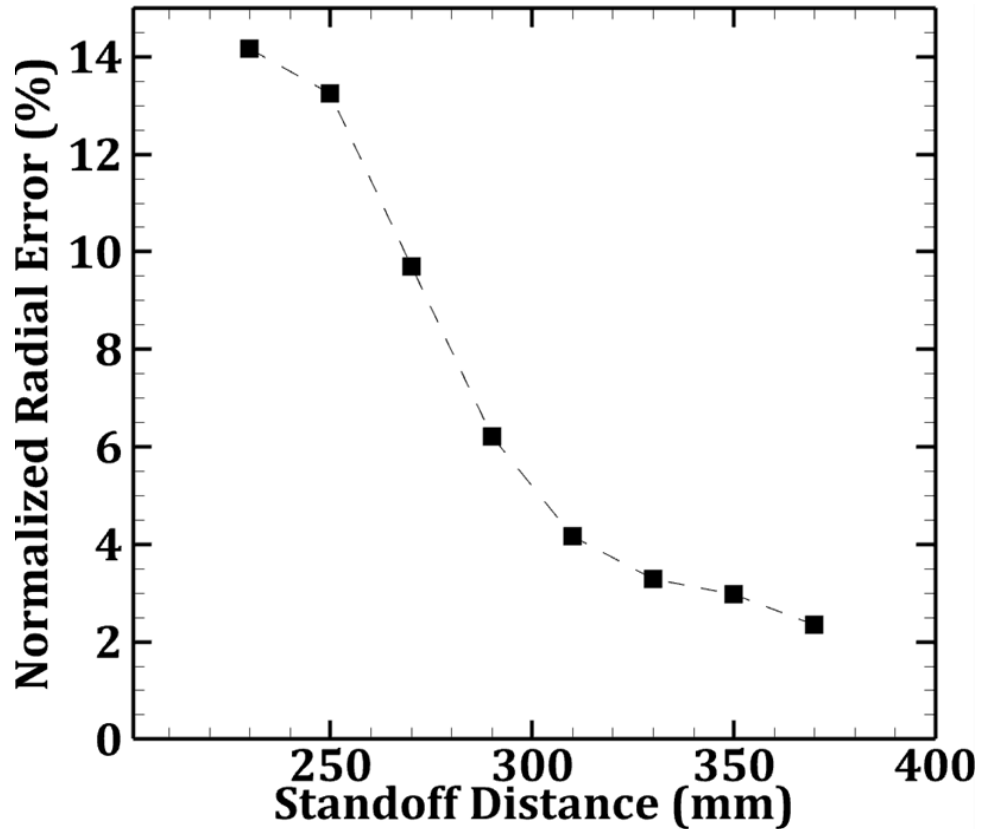


Figure 8: Normalized radial error of the distal lens and fiber leg at various standoff distances

### 5.3 System Calibration

There is a total of ten required components for this system. Their purpose and description can be seen in Table 3. To begin calibration and alignment of the system the fiber optic bundle system is first coupled to the camera. The fiber proximal end is rotated until the desired orientation is attained. The legs of the fiber are then oriented into the lens array (see Figure 6) and rotated until the desired image orientation is attained. A calibration plate is placed on a translational stage at a standoff distance of 350 mm from the lens plane and in the center of the lens array. The target is placed so that it is in the center of the desired depth of field. The distal lens is then mounted to the fiber leg mounts and the orientation and focus are adjusted until the image of the calibration plate is clear and sharp. The Scheimpflug angles of each fiber leg is

adjusted until the entirety of the image is in optimal focus. The apertures on the distal lens are then closed. The calibration plate is then traversed towards and away from the lens array to ensure the plate stays in focus throughout the desired image space. This process ensures that all views are acquiring information from the same domain and that the entire domain is in focus.

Volume optics are placed in the beam path to generate an illuminated volume. At the start of the beam path a 25 mm negative focal length spherical lens is used to expand the 4 mm beam in all directions. A 300 mm positive focal length lens is placed 275 mm away from the 25 mm negative focal length lens to collimate the light to a 48 mm diameter cylindrical illumination volume. A volume aperture that shapes the light cross section into a 33 x 33 mm square is placed after the positive focal length light to convert the cylindrical volume into a cube volume. The rest of the beam is absorbed by beam blocks and is not passed into the inspection volume. A schematic of this set up can be seen in Figure 9.

With the camera and laser system aligned to be viewing and illuminating the same domain their timing parameters are set for PIV recording. Because only two cameras are required for this approach the timing scheme is set up in a similar manner to that of stereoscopic PIV approach. The timing scheme used for this test can be seen in Figure 10. The recording rate for the cameras is set to 20 kHz and the repetition rate of each laser head was set to 10 kHz. The time difference between the image pairs was 20 microseconds. This timing parameters provided for a 10 kHz three-dimensional PIV system.

A set of images are acquired of the calibration plate for later volume calibration. The calibration is done by setting the plate at the front most plane of the imaging volume and traversing the plate incrementally and acquiring images for each increment of depth. After, any

seeded flow (reacting and non-reacting) can be issued into the volume domain and a PIV recording can be captured. Before processing the images, the quadrants must first be split and separated into multiple images, essentially cropping the original image into four separate images. The intensity of the images should be normalized and scaled to be similar if there are any noticeable intensity disparities.

The tomographic reconstruction and 3D cross correlation are performed using LaVision's imaging software, DaVis (version 10). To perform the tomographic reconstruction a projected calibrated volume is required. To calibrate the imaging volume, a two-dimensional target with known patterns is translated in the 3D domain and an image is captured at each increment. A total of 25 calibration images are acquired at 1 mm increments, from  $x=0$  to 25 mm. The target consists of 1 mm diameter dots spaced at 1.5 mm from the center with a total of 256 dots (16 x 16 array). The target parameters, increment size, and the calibration images are uploaded into DaVis. An origin is selected based off a common location in each calibration image, and a 3rd order polynomial fit is used to map the 25 calibration images into a projected 3D imaging volume. An example of the calibration procedure can be seen in Figure 11.

The algorithm implemented for tomographic reconstruction of the PIV data is the multiplicative algebraic reconstruction technique (MART). This produces a digital volume of a maximum of 750 x 750 x 500 voxels (37.5 x 37.5 x 25 mm, see Figure 4D) at 182,329 cubic microns per voxel (61 x 61 x 49  $\mu\text{m}$ ). Areas of low reconstruction confidence (view overlaps less than 50%) are excluded from data analysis reducing the final data size to 500 x 500 x 500 voxels (25 x 25 x 25 mm). To assess the spatial accuracy of the system, the digitally created volume is compared to the known physical dimensions of the calibration target over the three-dimensional domain. The physical volume was a total of 15,625 mm<sup>3</sup> and the digitally calculated volume

returned 15,640 mm<sup>3</sup> total volume (a 0.1% difference). This means that at any given voxel plane there is a spatial uncertainty of 0.05  $\mu\text{m}$ , ensuring that the three-dimensional cross correlation is being provided accurate spatial information.

Table 3: Necessary components to perform tomographic PIV

<b>Required Components</b>	
<b>Component Class</b>	<b>Component Description</b>
High Speed Camera	A minimum of 3 views needed
Scheimpflug Adapters	Required for focusing on domain of interest
Laser	High speed dual pulsed ND:Yag 532 nm
Volume Optics	Optics used to achieve illumination volume
Computational Hardware	Used to process images and extract velocimetry data
Programable Timing Unit	Sets the duty clock for each component in the PIV system
Calibration Plate	Sets the spatial coordinates of the imaging volume
Translation Stage	Translates calibration plate to calibrate depth of field
Tomographic Algorithm	Used to reconstruct volume and perform 3D cross correlation
Fiber Optic Light Bundles	For use in capturing multiple views with a single camera

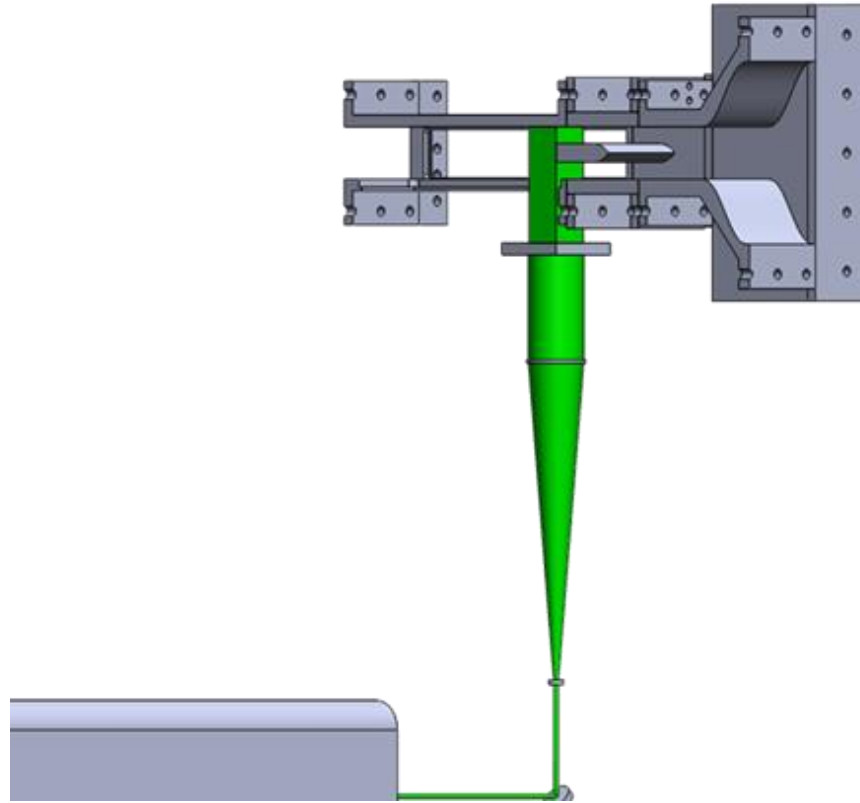


Figure 9: Schematic of the PIV laser diagnostic system

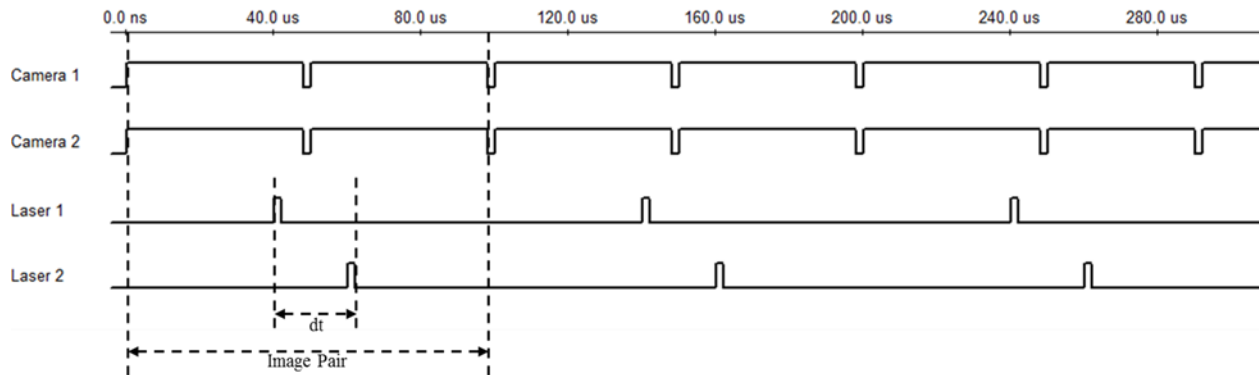


Figure 10: Timing Schematic for the TPIV system

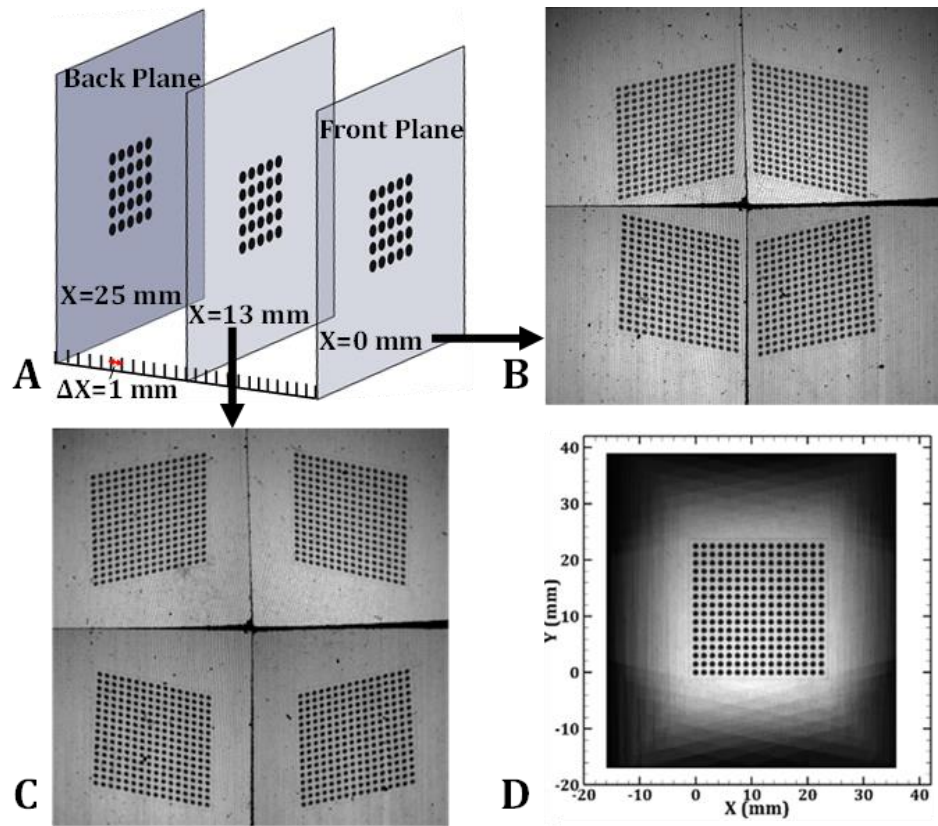


Figure 11: A. Schematic of the 2D target (3 planes shown). B. Image of the target acquired at  $x=0\text{ mm}$ . C. Image of the target acquired at  $x=13\text{ mm}$ . D. The projected volume (sum of views).

## CHAPTER SIX: VALIDATION EXPERIMENT FOR THE SINGLE CAMERA TOMOGRAPHIC SYSTEM

### 6.1 Experiment Description

A series of measurements were performed on a conventional channel flow to assess the accuracy of the single camera system. These included hot wire, planar PIV, stereoscopic PIV, and tomographic PIV. A blow down wind tunnel facility was used to generate a fully developed top hat velocity profile with a bulk velocity of 12 m/s in the optical domain, see Figure 12. This is achieved by using a 1.5 m long flow straightening duct upstream of the optical test section (45 x 127 mm cross section). The hot wire system consists of a unidirectional, single sensor wire used to extract the velocity profile by translating the probe along the 45 mm height at the center of the 127 mm span (63.5 mm). One high-speed camera is used to capture the planar PIV data at the center of the span and height with a spatial domain of 25 x 25 mm. The region of interest is illuminated by using cylindrical lenses to expand and collimate a beam into a 33 mm laser sheet with 90% uniformity in intensity and sub millimeter thickness. The planar PIV data is captured at 10 kHz at 1 MP (24.4  $\mu\text{m}$  per pixel). The stereo PIV data is captured in the same spatial domain using the same illumination optics but utilizes the top two views from the tomographic system (Figure 6) as the stereo views and a 1 mm thick laser sheet. The stereo data is also captured at 10 kHz at a 0.25 MP resolution (61  $\mu\text{m}$  per pixel). Spherical lenses and beam blocks are used to expand and collimate a beam into a 33 x 33 mm square cross section for tomographic PIV. The illumination volume contains 60% of the pulse energy (7.2 mJ) with 85% uniformity in intensity. Tomographic PIV is captured in the same spatial domain utilizing the single sensor system (Figure 6) described in the previous section with the depth centered at 63.5 mm in the span (Figure 12).



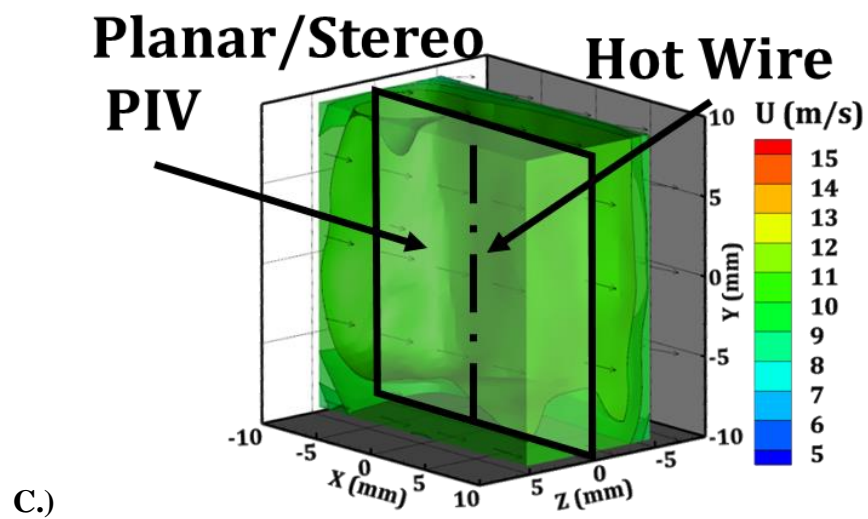
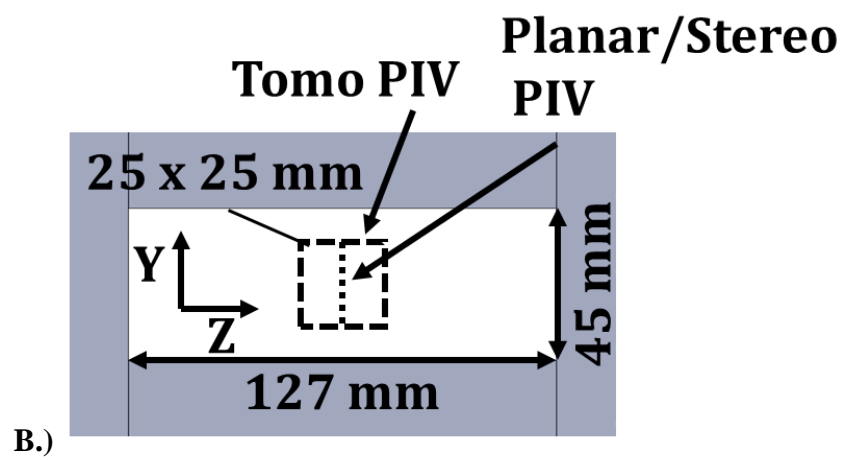
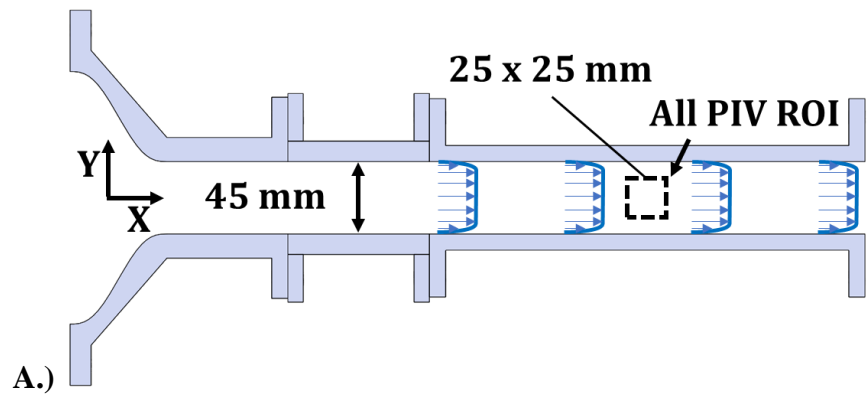


Figure 12: Schematic of the facility with the location of the imaging domain in A.) XY and B.) YZ, with the C.) tomographic data displayed in relation to hot wire and 2D PIV.

## 6.2 Validation

All PIV data is captured in the same spatial domain as depicted in Figure 12, with the exception of the hot wire data that is confined to a single line over the entire 45 mm height. The tomographic PIV data is temporally and spatially averaged in two dimensions, along the axial length (x) and through the depth (z) and is plotted against the height (y) to represent the mean velocity profile for the measurement. The stereoscopic and planar PIV data is reported by taking a temporal and spatial average along the axial length (x) and is plotted against the height (y) as well for comparison. The hot wire data is presented as a temporal average only and is plotted along the height (y). The data for the axial velocity is compiled in Figure 13, where the bars display the standard deviation of the spatial and temporal data range at a given height.

Utilizing the hot wire data as the standard measurement for acquiring the velocity profile, the deviation from the true axial velocity profile in the range of  $-12.5 \leq y \leq 12.5$  mm is reported by calculating the percent differences between the velocity profiles associated with the PIV measurements to that of the hot wire velocity profile. This returns a maximum of 3.1% deviation from the hot wire velocity profile for the fiber coupled tomographic PIV system, 1.9% for the stereoscopic PIV data, and 1.7% for the planar PIV data. The percent deviation from the hot wire velocity profile is compiled in Figure 14 and shows that the tomographic data deviates the most from the reference hot wire data, however, this error is less than twice that of the conventional planar (higher resolution, non-fiber coupled) PIV. Further comparisons show that the total mean of the axial velocity is  $12.1 \pm 0.6$  m/s,  $12.0 \pm 0.5$  m/s,  $12.0 \pm 0.4$  m/s, and  $11.9 \pm 0.2$  m/s for the tomographic, stereoscopic, planar, and hot wire respectively. This shows agreement between the measurements and demonstrates the accuracy of the single camera system.

To assess the performance of the system in capturing the span wise velocity (depth velocity  $z$ ), a cross comparison between the stereoscopic PIV, the current standard for capturing cross plane velocity information, and the tomographic PIV is performed similar to the axial profile comparison. The span wise velocity for both measurements is plotted in Figure 15, where the bars denote the standard deviation of the spatial and temporal data range. Utilizing the span wise velocity profile associated with the stereoscopic data as the standard, the tomographic data deviates from the profile by a maximum of 0.8%, demonstrating the accuracy of the single camera system in capturing the third component of velocity associated with the depth.

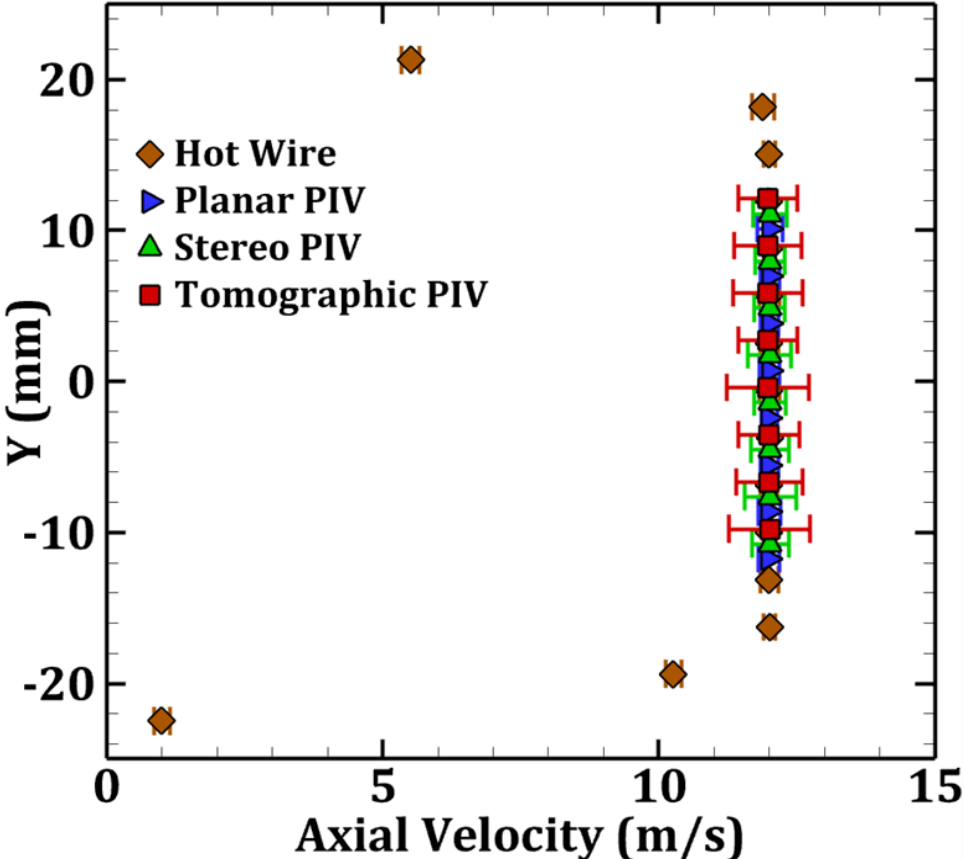


Figure 13: Mean axial velocity (along x axis) associated with the Hot wire and PIV measurements. Error bars denote deviation from the mean.

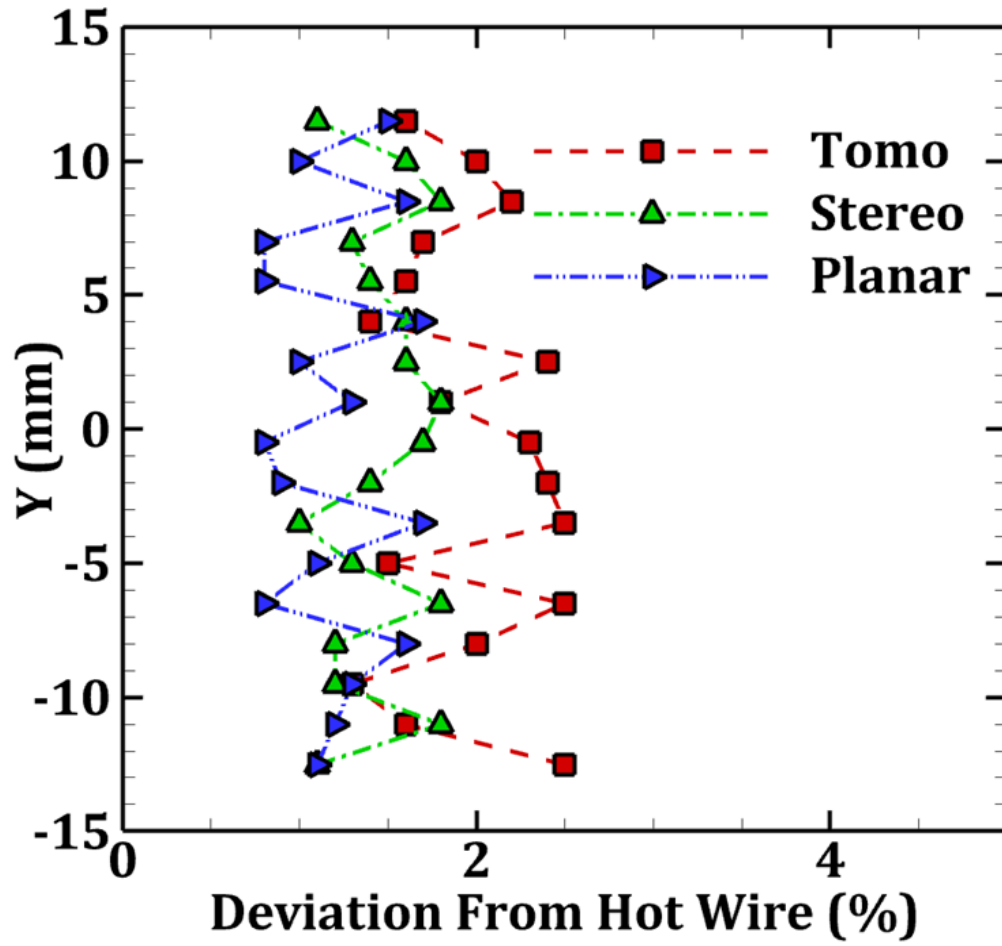


Figure 14: Deviation of the PIV measurements from the hot wire velocity profile along the height of the measurement domain.

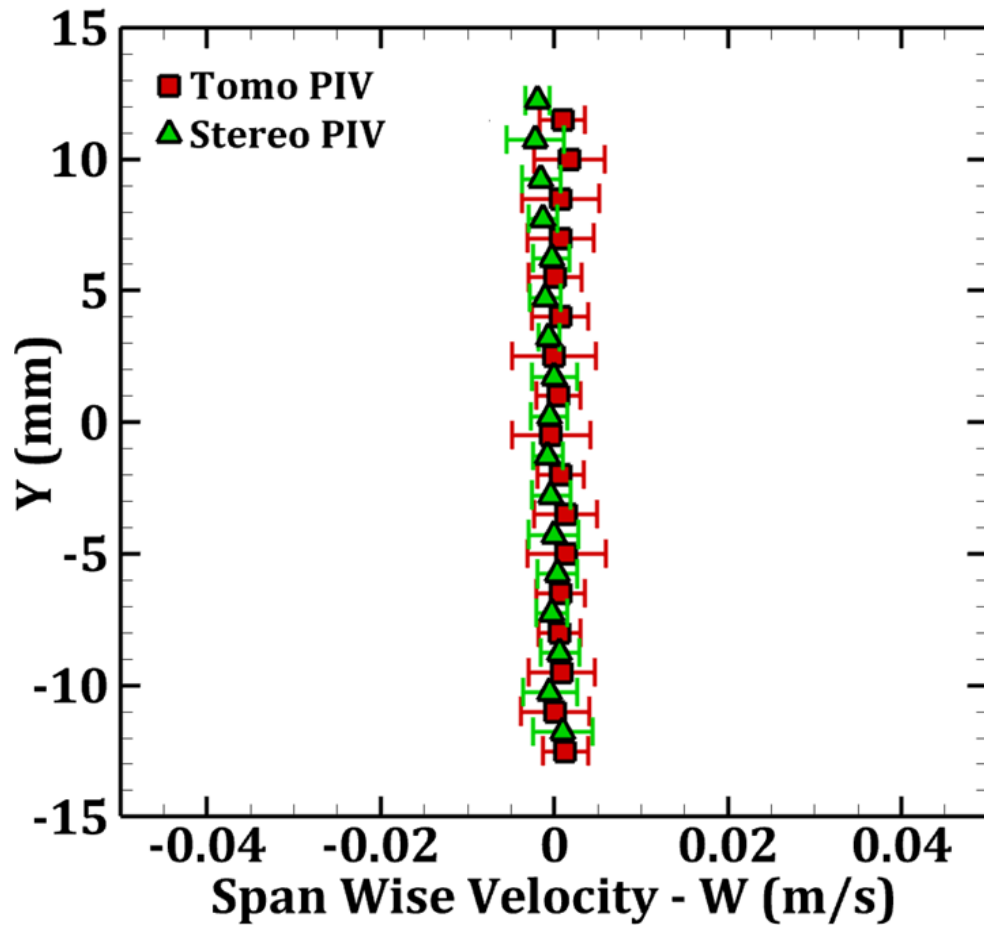


Figure 15: Mean span wise velocity (along z axis) associated with the stereoscopic and tomographic PIV measurements.

## **CHAPTER SEVEN: FINDINGS FROM THE FUEL-AIR EXPERIMENT**

At this point, simple cost-effective methods have been described for acquiring both the density and velocity information associated with reacting flow fields, but it is important to scrutinize these methods and assess their limitations. We begin with the fuel-air approach.

### 7.1 Data Characterization

Upon successful validation, the experiments were conducted in the pressure vessel with the 99% iso-octane certified gasoline. The injection procedure discussed in the experimental section is followed to introduce fuel and air into the chamber. Internal temperature was held at 380 K before ignition for all cases. Local temperature rise due to the laminar flame pre-heat zone is expected to scale and captured through the equivalence ratio effects. Fuel and air were injected until the desired charge pressure and equivalence ratio was achieved, and the mixture was ignited by the spark plug. The ignition event is followed by a pressure rise in the pressure vessel. A rapid pressure rise due to combustion is not seen until nominally 20 ms after ignition. This allows for ample time to acquire the effects of charge pressure on the intensity ratio of the initial flame kernel. Data acquisition is initiated 2 ms prior to ignition where ignition occurs at 0 ms.

The average of the intensity ratio data for comparison to the charge pressure needs to be clear. As such, the time domain for data extraction is determined using the propagation speed as an indicator of the constant pressure region. Spherical propagating flames are a widely used method in the calculation of propagation speed and can provide information on the pressure of a flame kernel's environment [52]–[54].

Propagation speeds have previously been measured using spherically propagating flames by the constant pressure method (CPM). The CPM's primary advantage is that the well-established fact that the pressure and temperature rise is negligible and that the burned gas can be assumed to be static in this early stage of the development of the spherical flame kernel [55], [56]. The measurement of propagation speed is desirable at points where there are minimal effects of stretch or when there is zero stretch on the kernel [57]. The pressure vessel used in this study is well suited for the CPM in that its large volume allows for minimal effects in the early stages of the spherical kernel's development. During the early stages of the flame kernel, where the pressure rise and temperature rise is considered negligible [55], a time frame can be chosen for constant pressure analysis.

Propagation speeds at atmospheric pressure for gasoline surrogate fuels have been measured previously to be on the order of 55 to 60 cm/s at 358 K and an equivalence ratio of unity [58]. Using the propagation speed as a benchmark and applying the CPM, the propagation speeds of the gasoline flame in this facility were calculated to be on the order of 65 cm/s for atmospheric cases at 380K. The calculation is based on visual techniques, which involved tracing the outer edge of the propagating flame, relating pixel values to a physical dimension measured from a calibration grid, and relating the displacement to the camera frame speed. This is summarized by equation 8.

$$S_L = \frac{SR * \Delta Pix * FPS}{F} \quad (8)$$

Here,  $S_L$  denotes the propagation speed, SR is the spatial resolution of the image, which is 0.019 cm/pixel,  $\Delta Pix$  is the number of pixels the flame front has displaced between frames, FPS is the recording framerate, which is 3000 frames per second, and F is the amount frames

used for the calculation. This results in an intensity ratio calculation that is performed and reported for a time increment of 0.333 ms and allows for a total of 60 steps before the kernel edge is no longer in the field of view.

The calculated propagation speed, the intensity ratio, and pressure associated with an atmospheric case are presented in Figure 16. The intensity ratio and flame speed are not calculated for the first 3 ms as the flame kernel is relatively small to acquire accurate measurements. As shown in Figure 16, the propagation speed is nominally constant for a time span of 7 ms before the speed and the corresponding intensity ratio begins to deviate. From 3 to 10 ms the flame speeds moving average was 65 cm/s. At ten milliseconds post-ignition the flame speed begins to taper, decreasing to almost 55 cm/s. The intensity ratio behaves in a similar manner, in that, in the region where the flame speed is constant the intensity ratio is also nominally constant. Inversely, though, instead of a taper in the intensity ratio, an increase is observed at 10 ms post-ignition. Thus, it is expected that there is an inverse relationship between the flame speed and pressure rise and a direct relationship between the intensity ratio and pressure rise at 10 ms post-ignition. Because the interest of this study is on the behavior of the intensity ratio at various charge pressures, a region of interest of 7 ms (from 3 ms post ignition to 10 ms post ignition), denoted in Figure 16 by the dash dotted lines, is used to extract intensity ratio data. This time span, chosen by utilizing the area where flame speed is nominally constant, ensures that the acquisition of the intensity ratio is in a constant pressure region and that there is negligible pressure rise similar to propagation speed studies using the CPM. The data associated with the divergence domain in Figure 16 displays that the intensity ratio is indeed affected by pressure and care must be taken when selecting data to compare to the initial charge pressure.



The samples acquired during the 7 ms are on the order of twenty frames. During this period, the pressure rise is less than 0.5 bar. To characterize the impact of this pressure, rise at various equivalence ratios, the intensity ratios were calculated at each time step and plotted as a function of equivalence ratio. Figure 17 shows the plot of intensity ratio as a function of equivalence ratio for multiple time steps after ignition at a charge pressure of atmosphere. The intensity ratios are plotted against the equivalence ratios measured from the oxygen sensor. The  $CH^*$  signal is also digitally scaled by a factor of 1.6 before the intensity ratio is taken to account for image sensor sensitivity. The results show a gradual shift of the intensity ratio as the time step increases. It is important to note, that the pressure rise effect on the intensity ratio within this time duration is not significant enough to consider the time steps as separate correlation curves. This in fact shows that the intensity ratio is nominally insensitive to relatively minor changes in pressure for 99 % iso-octane gasoline. Accordingly, the average intensity ratio of the sample of frames acquired during the 7 ms is used for the study of the intensity ratio relative to equivalence ratio and charge pressure.

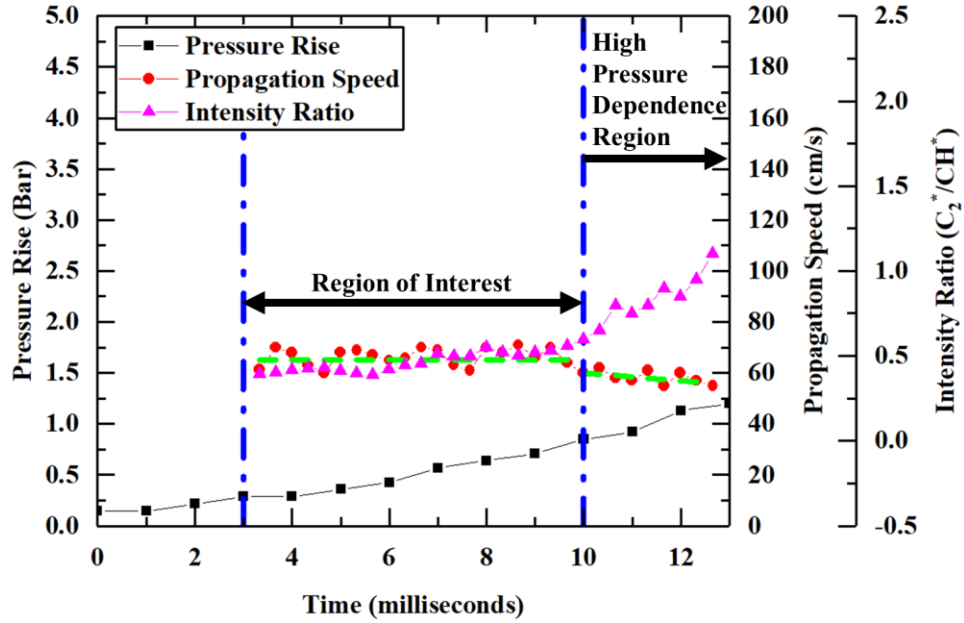


Figure 16: The initial 13 ms duration of the intensity ratio, laminar flame speed, and pressure.

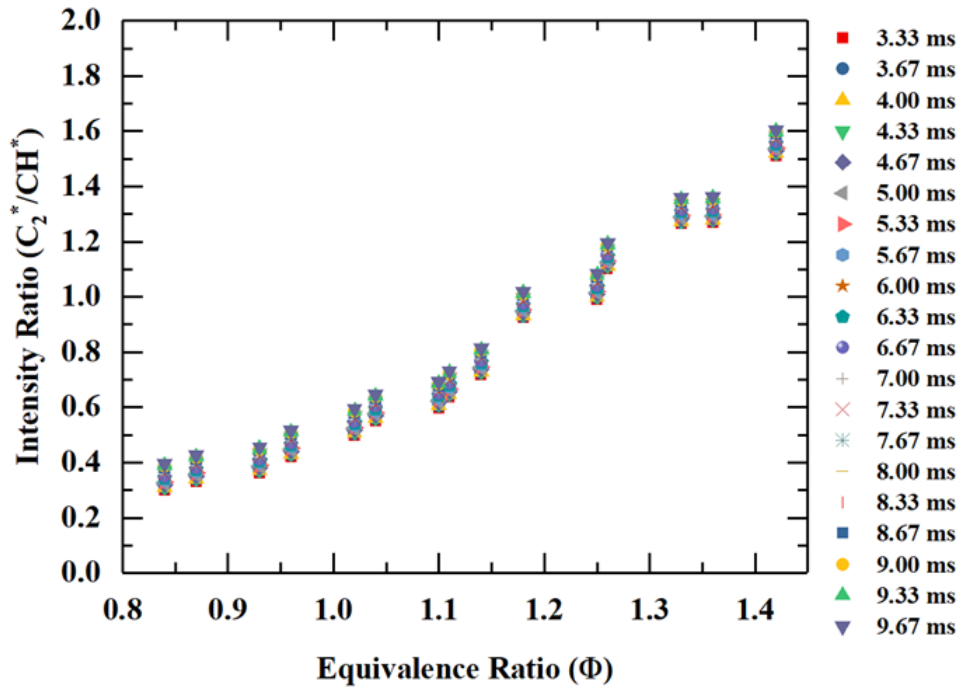


Figure 17: Various time steps of the intensity ratio for the different equivalence ratios acquired in the region of interest de-noted in Figure 16.

## 7.2 Creating the Calibration Map

The initial internal temperature of every test is held at 380 K. Once the frames have been extracted and processed, the average intensity ratios for each point are calculated and plotted as a function of the equivalence ratio. Figure 19 shows a representative correlation curve obtained for a charge pressure of one atmosphere for the certified gasoline (99 % iso-octane). The points are acquired by averaging the data taken within the time span and reporting the value associated with the equivalence ratio. The results shown in Figure 19, behave in the same manner as previous works where the intensity ratio increases with increasing equivalence ratio [8], [9].

This process is repeated for all charge pressures from 1-10 bar, and the compiled data is presented in Figure 19. The charge pressure effects the intensity ratio in the same manner as noted in the Figure 16 with a few differences. Figure 19 shows that the intensity ratios associated with the lean equivalence ratio are not as sensitive to the change in charge pressure as much as the rich equivalence ratios.

The higher charge pressure cases (i.e. 7 and 10 bar) show a larger sensitivity in intensity ratio as the equivalence ratio shifts towards rich. This is most likely due to the dominance of  $C_2^*$  at higher pressure [11], [12], [19]. As the charge pressure is increased, the average intensity ratio increases accordingly. The intensity ratio difference between the 1 and 3 bar cases are lower than the intensity ratio between the 7 and 10 bar cases. This would suggest that the relationship of the intensity ratio to pressure is more sensitive with increased pressure. Thus, presented differently in Figure 20, it can be said that the intensity ratio,  $C_2^*/CH^*$ , becomes more sensitive as the equivalence ratio goes towards rich and with increase in pressure. In Figure 20, the direct effect of pressure on the intensity ratio  $C_2^*/CH^*$  can be seen at select equivalence ratios. It is noted that

the range of intensity ratio values widens as the pressure increases, indicating the previously observed high sensitivity of pressure to intensity ratio.

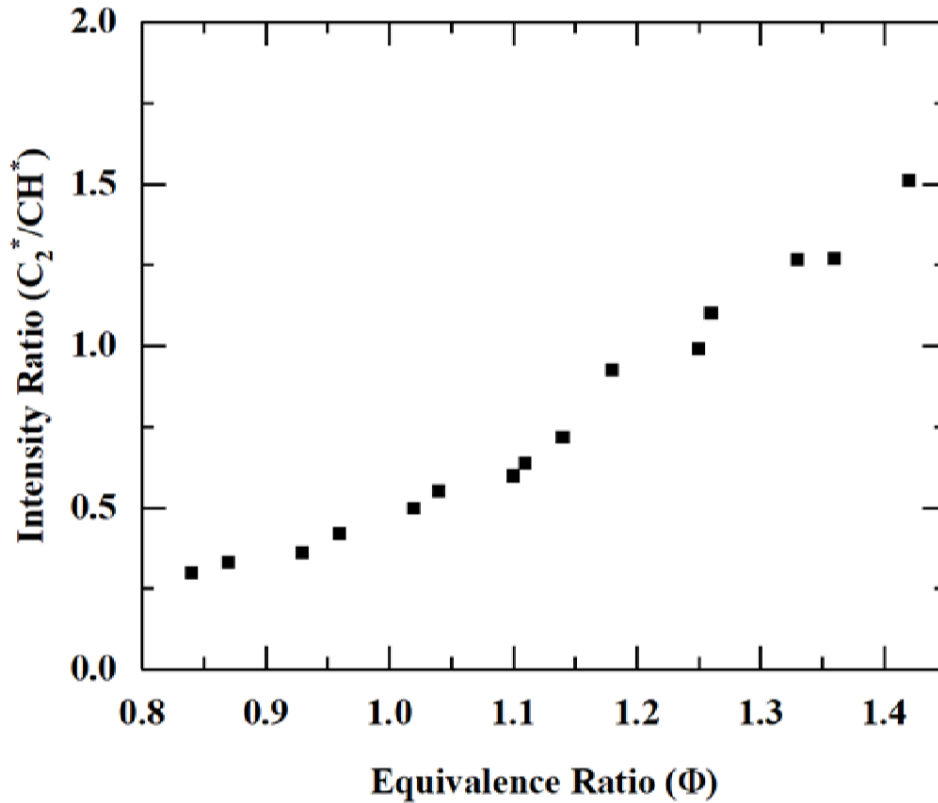


Figure 18: Correlation curve of the radical intensity ratio  $C_2^*/CH^*$  versus the equivalence ratio measured by oxygen sensor in the exhaust port for certified gasoline (99 % isooctane) at a charge pressure of atmosphere and initial temperature of 380 K. Points are averaged over 7 ms.

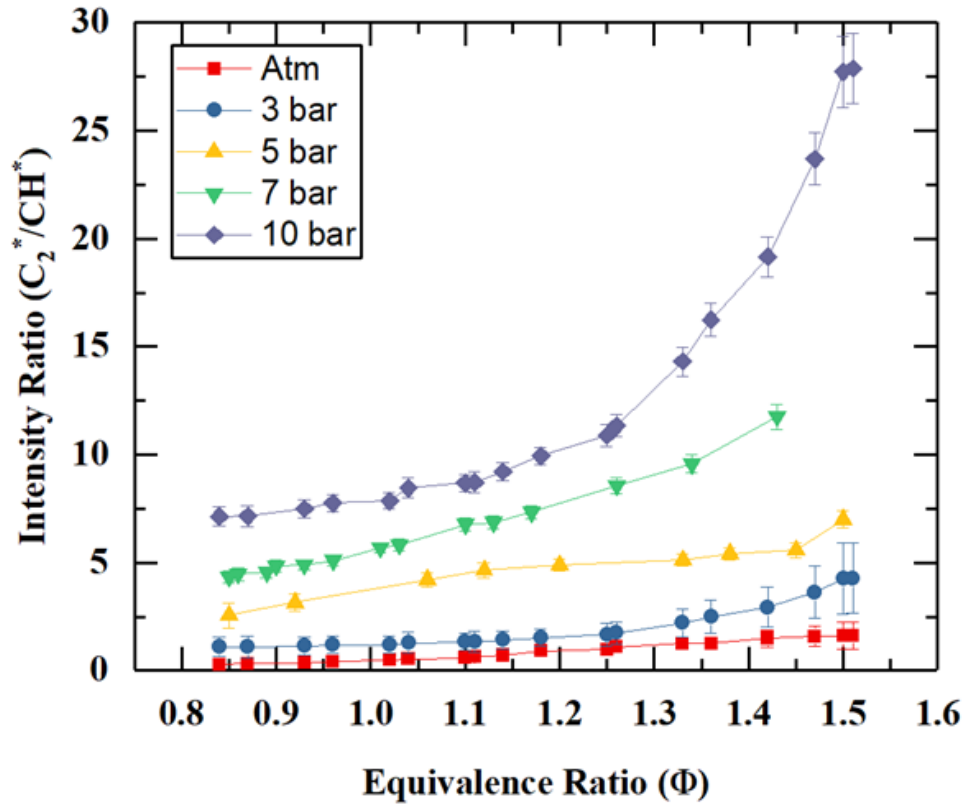
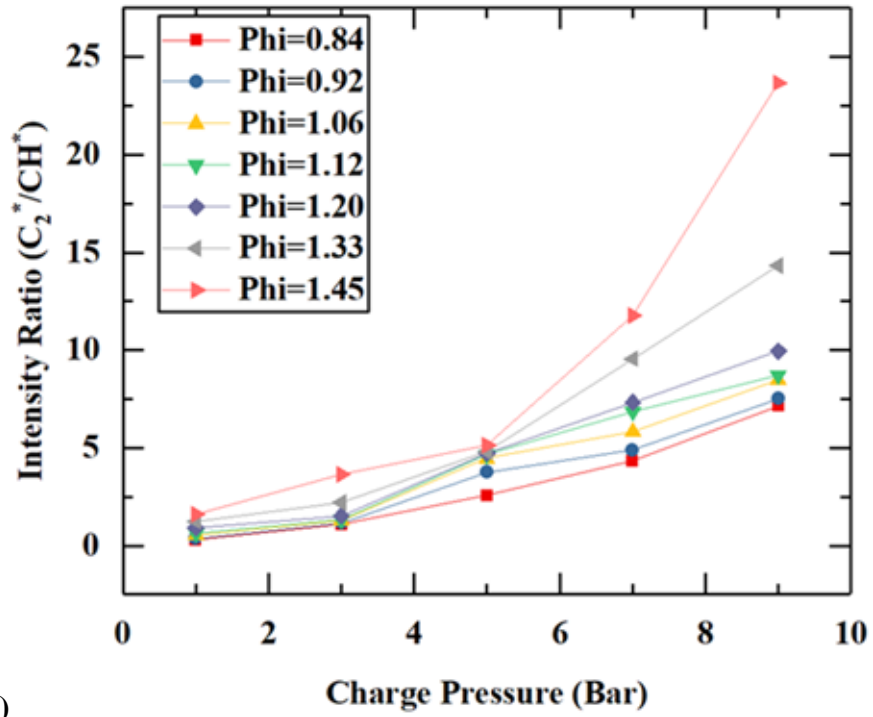
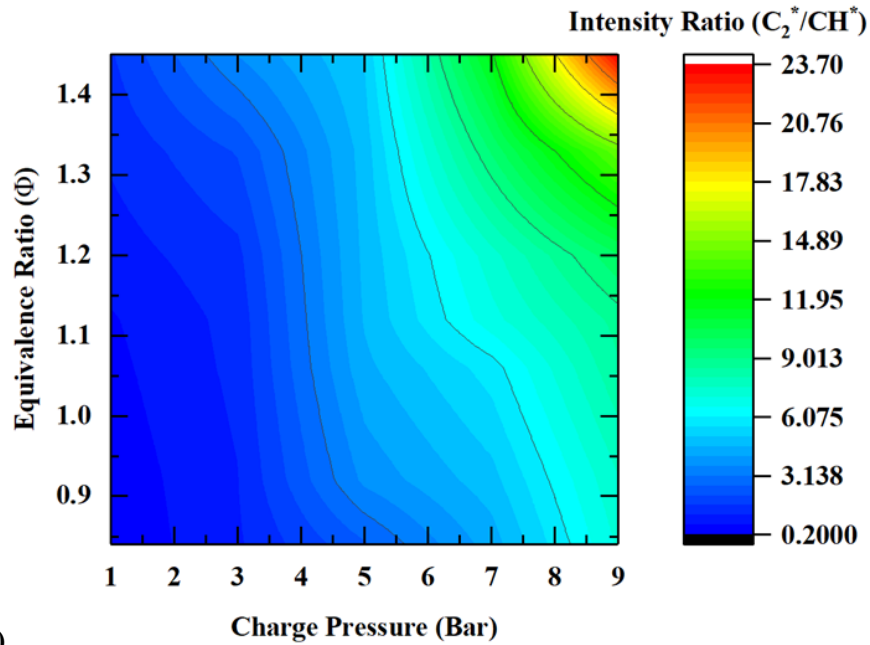


Figure 19: Correlation curves for charge pressures of atmosphere to 10 bar.



A.)



B.)

Figure 20: A.) Correlation curves from 1 to 10 bar at select equivalence ratios. B.) Correlation map of the intensity ratio as a function of equivalence ratio and charge pressure.

## CHAPTER EIGHT: TOMOGRAPHIC PIV FINDINGS

### 8.1 Air Jet

Utilizing the optical set up in Figure 6, two experimental set ups were used to assess the system's ability to capture unconfined and confined flows. A seeded air jet metered to 15 m/s was used to assess the ability for the system to capture a more complex flow field and is compared to data taken utilizing stereoscopic PIV. The results compared are not simultaneously acquired but are acquired in the same visual domain, in the same manner as Figure 12. The air jet see Figure 21, was 15 mm in diameter and was seeded with one-micron aluminum oxide particles. The pulse separation between the lasers was set to 20 microseconds and the optical configuration used were the same components and procedures as previously mentioned in chapter six. The data is acquired, reconstructed, and analyzed, an instantaneous snapshot of the data can be seen in Figure 22A along with the associated view callout in Figure 22B. Please note that data is only taken using the four corner imagers or imagers 1 through 4 in Figure 22. As seen previously the tomographic system yields comparable results to that of the stereo data. Figure 23A displays the mean axial velocity of the data with the stereo plan overlaid for comparison. The topology is similar to what has been seen in unconfined axial flow studies [59]. The velocity profiles extracted at the plane are compared in Figure 23B and are within 3% difference. The data shows the three-dimensional topology associated with the air jet. With the three-dimensional axial velocity information, it is possible to distinguish the jet core from the outer shear layer by the velocity gradient. The vorticity is reported in a similar manner in Figure 24. The tomographic system returned a wider range of values for the z vorticity but maintained within a 3% difference to the stereo data. The z-vorticity gives insight into the shear layer location of the air jet as well as the core size (where the vorticity is close to zero). The vorticity

data plotted in Figure 24B suggest that the jet core is 12 mm in diameter. Another benefit of the three-dimensional information is the ability to inspect the velocity profile at various slices in space. Figure 23A shows that as we leave the center of the jet, where the velocity profile is parabolic, and go towards the outside of the jet the velocity profile becomes less parabolic and more uniform. In the same manner we can use the three-dimensional vorticity data to extract the edges of air jet where the effects of the shear layer have dissipated. This suggest that the total jet size is 20.5 mm in diameter depicted by the area where the vorticity dissipates to close to zero. These are just a few simple types of analysis that could be done with three-dimensional information. The amount of information that can be extracted is immense. This data could be used to extract information such as vortex ring structures, strain induced by the shear layer, etc., all for a simple air jet. This has large implications for those who are interested in jet impingement for heat transfer applications.

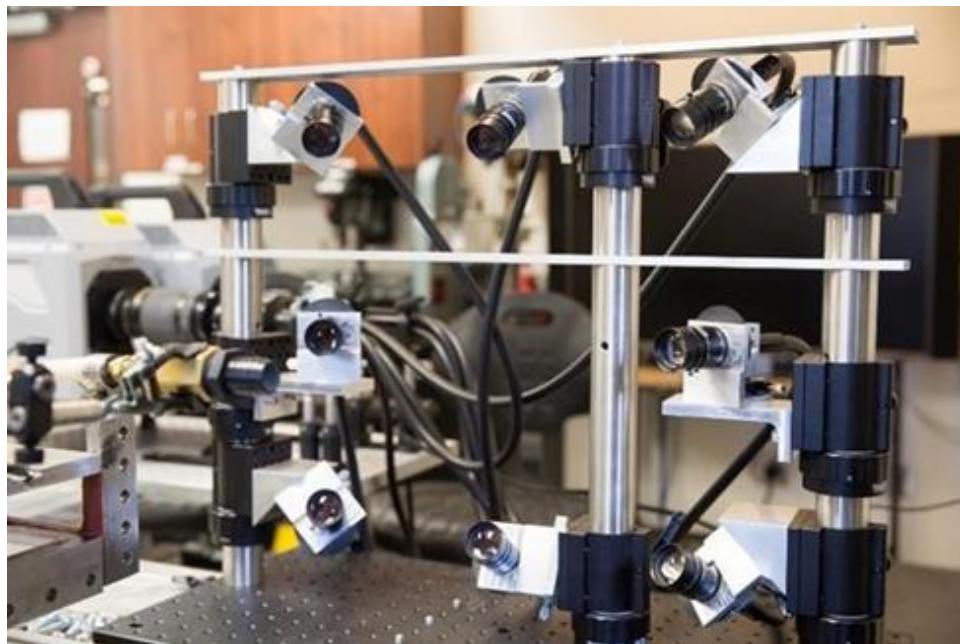
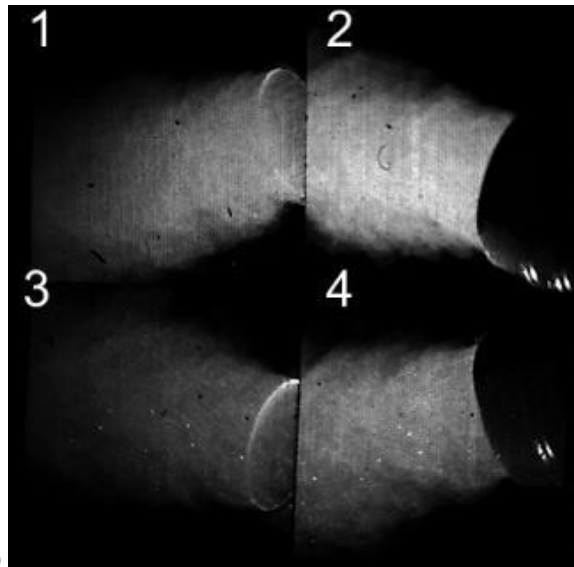
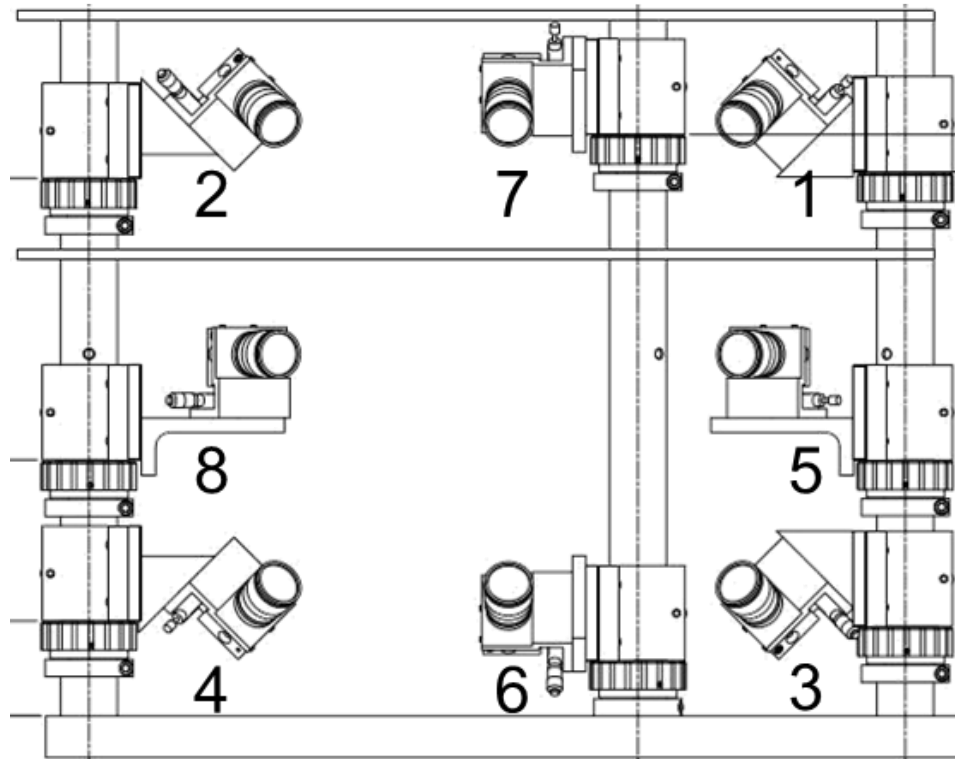


Figure 21: Image of the seeded air jet experiment, only corner imagers used to take data.





A.)



B.)

Figure 22: A. Raw image of flow field associated with the air jet experiment B. Lens location callout, only the four corner imagers are used to take the data.

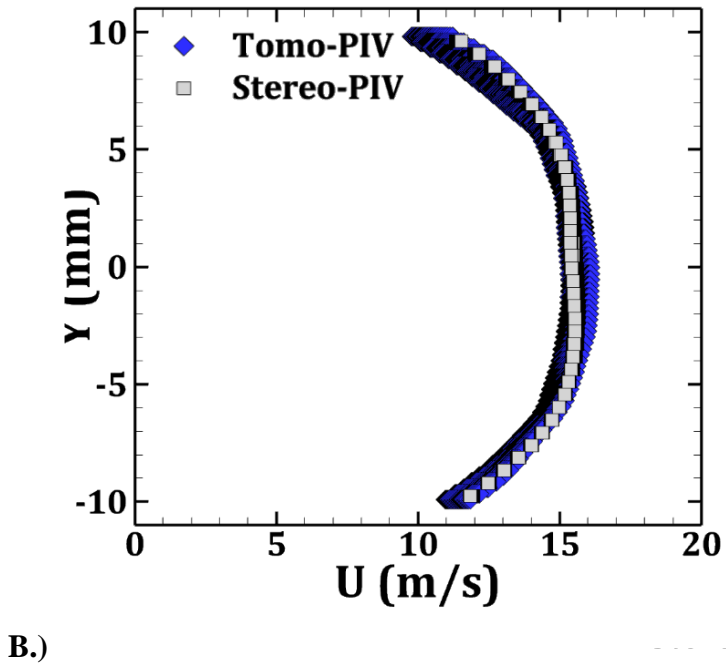
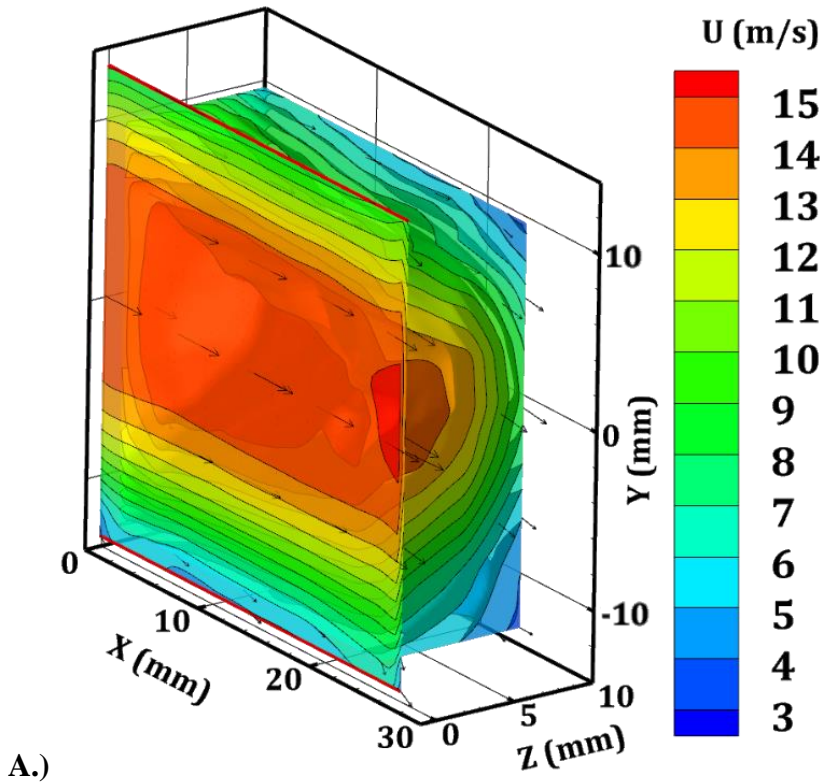
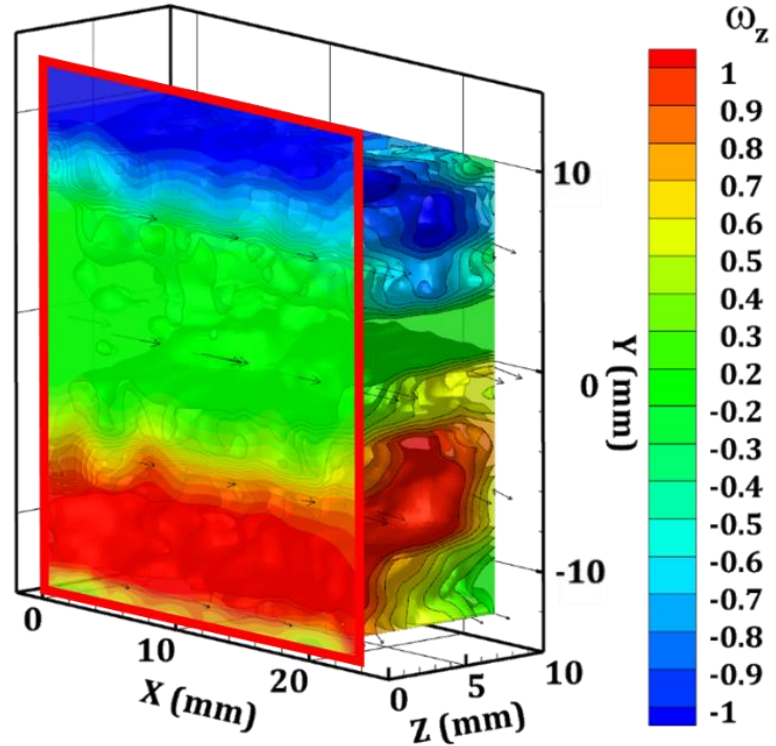
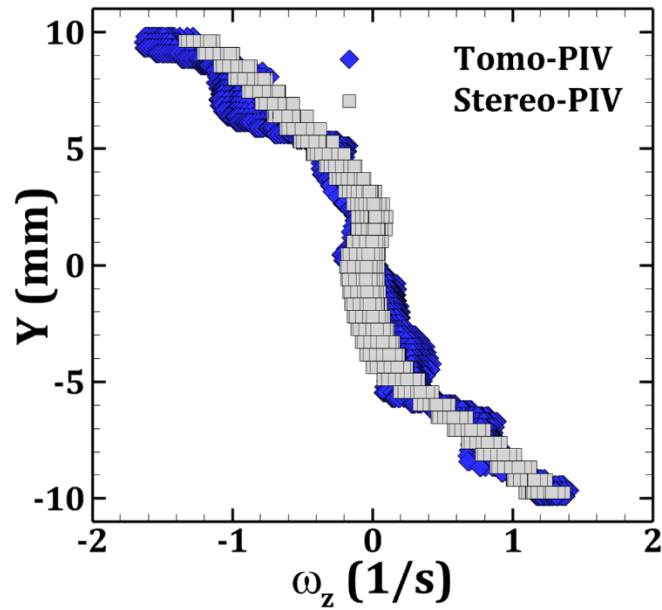


Figure 23: A. 3D mean axial velocity flow field from the seeded air jet data set with the stereo plane outlined by the dotted section B. extracted mean velocity profiles from the seeded air jet data for both 4D and stereo PIV at all x locations



A.)



B.)

Figure 24: A. Mean Three-dimensional z-vorticity of the seeded air jet with the stereo result outlined by the dotted section B. Extracted vorticity profiles associated with the air jet compared to stereo PIV at all x locations.

## 8.2 Confined Bluff Body Flow

Because it is important to understand the limits of the system. A TPIV recording was acquired for a confined bluff body flow in a subsonic wind tunnel facility. A schematic of the experiment can be seen in Figure 25 with the 25 mm square domain outlined. The domain is placed 5 mm away from the edge of the bluff body, which is 16 mm in height. To capture the entire flow field two sets of data were taken. One set with the volume domain biased towards the top of the bluff body (as can be seen in Figure 25) and another set biased towards the bottom of the bluff body. The information is then overlaid and reported. The data acquired is compared to previous 2D PIV data taken in the facility for the entire test section domain. The depth of field for the TPIV system was limited to 6 mm due to optical obstructions from the flanges of the optical test section. The mean axial velocity is reported in Figure 26. The mean velocity values agree and are below 3% difference. The recirculation region is calculated to be about 22 mm (including the 5 mm offset from the edge of the bluff body) from the data shown in Figure 26A where the 2D PIV (Figure 26B) shows a recirculation zone of about 1.5 bluff body heights (24 mm). The same can be seen from the cross plane and vorticity in Figure 27 and Figure 28, where the reported entrainment length is 30 mm for the TPIV system and 32 mm for the 2D PIV data. The boundary layer vorticity's high intensity region is seen to extend out 31 mm from the edge of the bluff body in the 2D PIV data where the data acquired from the TPIV system does not acquire data past the 31 mm mark where the vorticity intensity begins to taper which is still in agreement with what is seen in the 2D data. It can be seen that the same information that can be acquired from two-dimensional PIV is being captured by the three-dimensional system, but the difference is the third dimension. This allows for a clearer characterization of facilities as it is now possible to declare the degree of two dimensionality in experimental facilities. For example,

the span wise velocity ( $w$ ) has an average of 0.2 m/s in the entire inspected domain with a standard deviation of velocity being 0.01 m/s. Of course, for characterizing turbulence statistics it is important to have the third dimension, but it can be said that the bulk of the turbulence is occurring two-dimensionally.

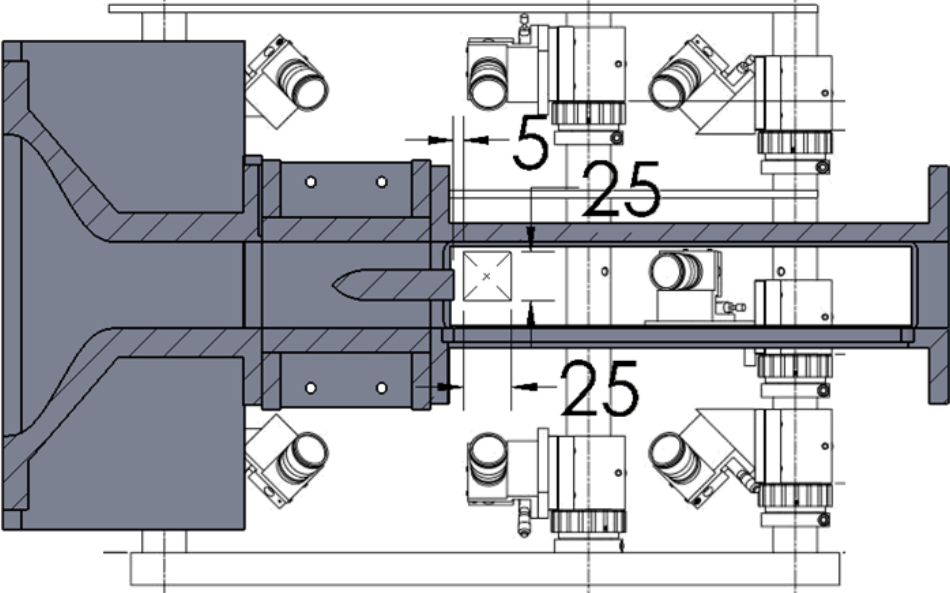


Figure 25: Schematic of Confined Bluff body flow experiment.

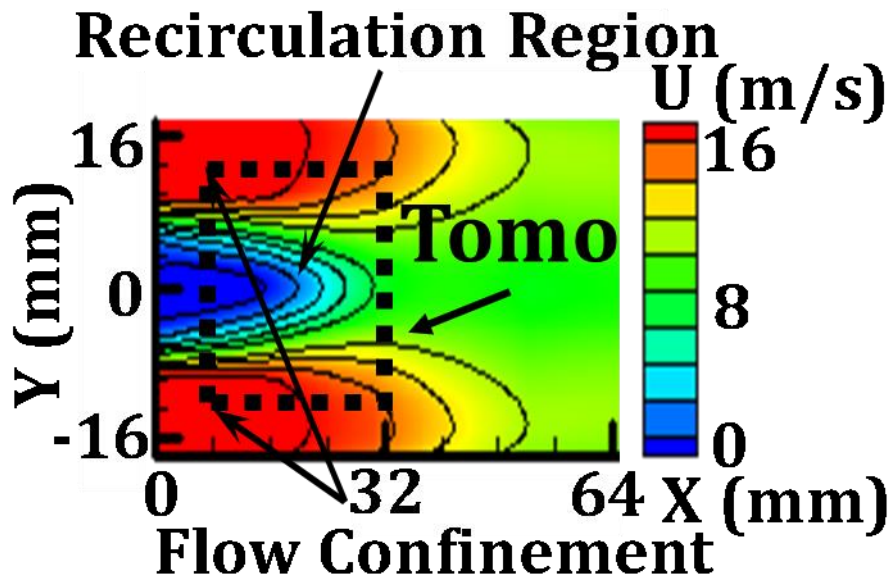
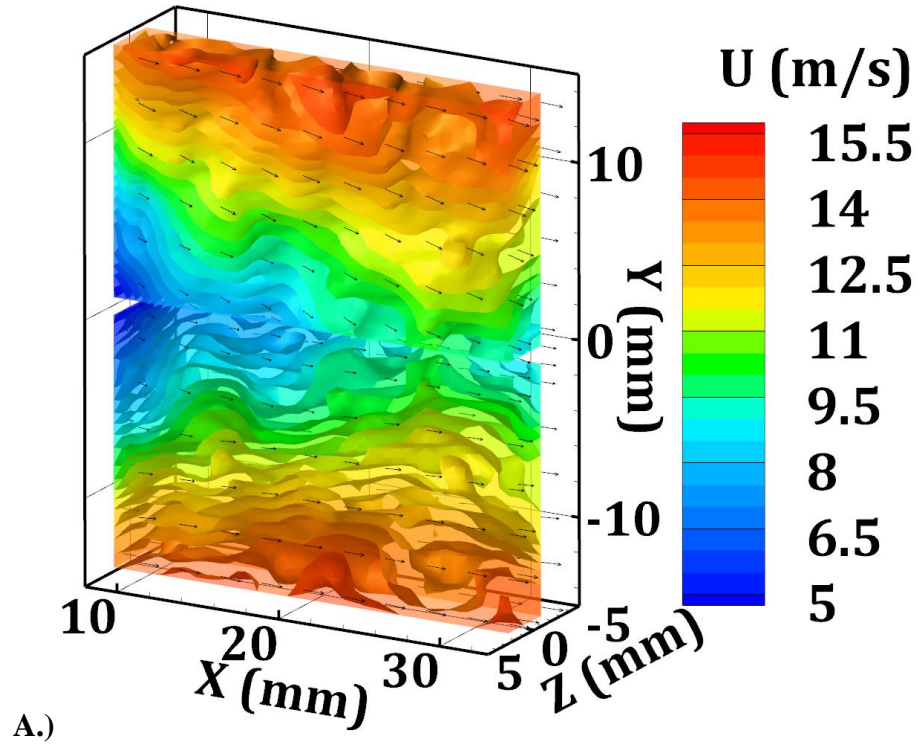


Figure 26: A. Three-dimensional mean axial velocity B. Axial velocity acquired from 2D PIV taken in the same facility.

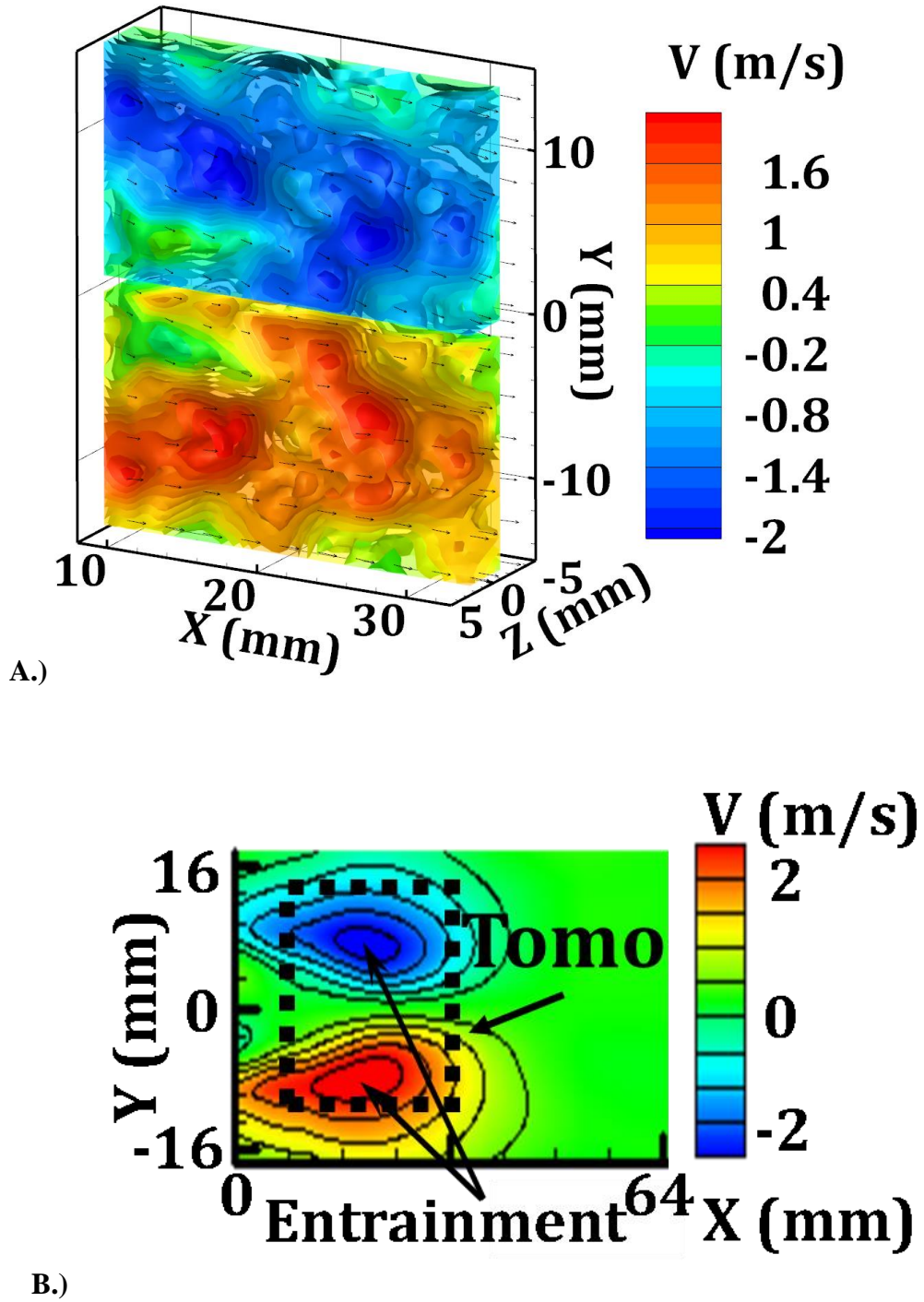


Figure 27: A. Mean Three-dimensional cross plane velocity data B. Cross plane velocity acquired from 2D PIV taken from the same facility



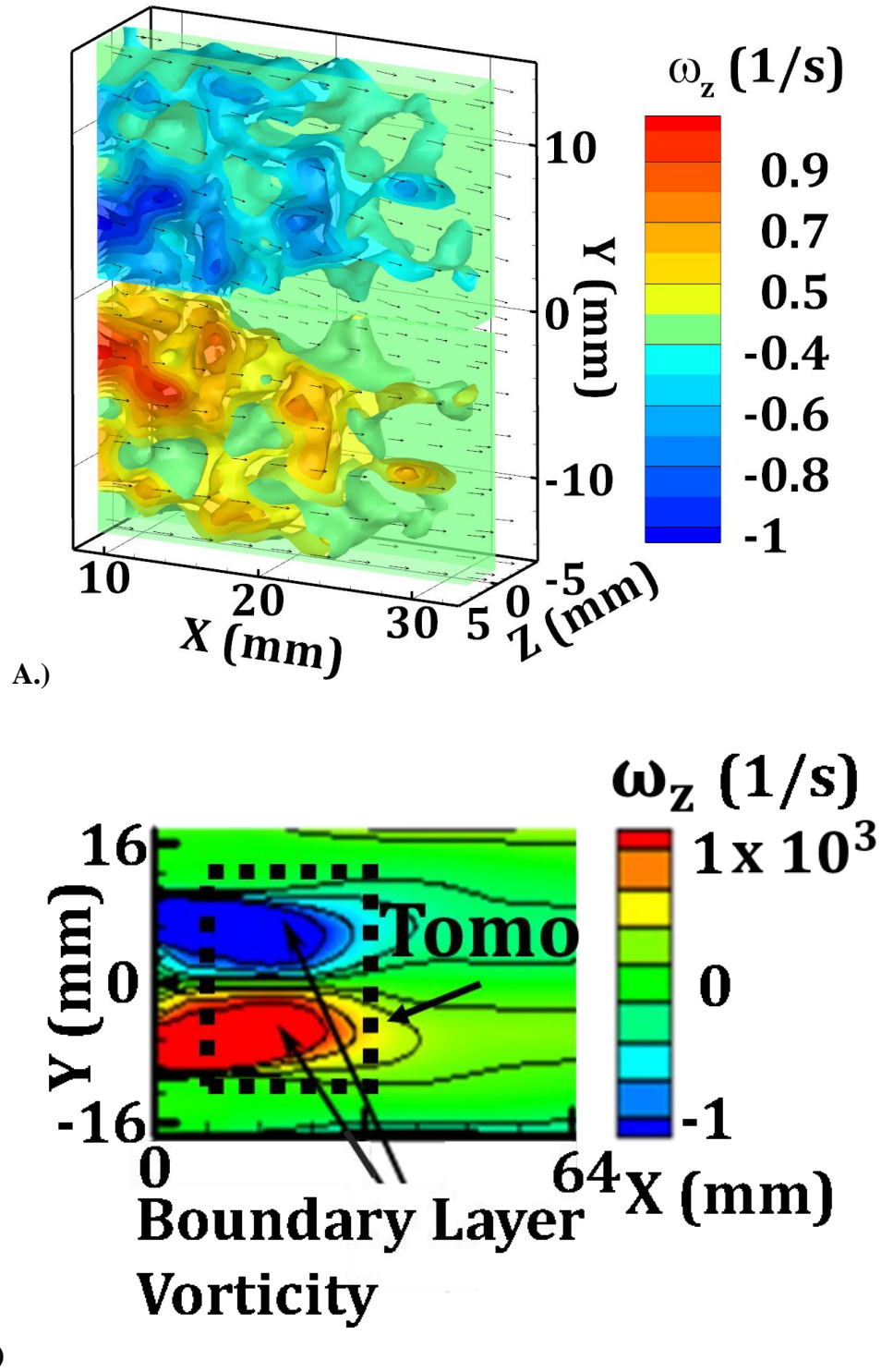


Figure 28: A. Mean Three-dimensional z-vorticity data B. Z-vorticity acquired from 2D PIV taken from the same facility.



## **CHAPTER NINE: COMBINING SPECIES IMAGING AND THREE-DIMENSIONAL PIV UTILIZING THE SINGLE SENSOR APPROACH**

At this point in this work we have described, validated and tested approaches for capturing line of sight species and 3D velocimetric information utilizing only one camera sensor. This section will combine the two measurements into one and perform a detailed characterization of the finalized 3D system.

### 9.1 System description

Figure 29 shows a schematic of the combined flame and PIV imaging system. There are few key differences from what is depicted in Figure 6. First is the inclusion of a second high-speed camera that will be used to capture three-dimensional species information. Second, the system is no longer operating with two opposed lenses. Instead, one 50 mm macroscopic relay lens with 1:2 up to 1:5 magnification capabilities is directly coupled to the camera. This approach magnifies the image coming from the proximal end of the bundle to the correct size for a 1:1 fiber to pixel ratio for the camera's image sensor. This allows for a finer degree of focus and removes signal clipping (vignetting) on the edges of the images. Third, a CH\* filter and light intensifier are placed in the optical path of the species imaging bundle to isolate the CH\* species associated with the flame and to amplify the light signal so that it can be captured at higher speeds. Lastly, the proximal end is on a 3-axis micrometer stage, with rotation about the vertical (z) stage, allowing for fine alignment of the proximal end with the sensor on the camera. Referring to Figure 22B, viewpoints 1 through 4 are used for capturing PIV data, while viewpoint 5 through 8 are used for species imaging. Viewpoints 6 and 7 are set up to be at the horizontal center of the lens array and are mounted such that  $\Phi$  is 22.5 degrees and  $\theta$  is 0

degrees, see Figure 7. Viewpoints 5 and 8 are set up to be at the vertical center of the lens array and are mounted such that  $\Phi$  is 0 degrees and  $\theta$  is 22.5 degrees, see Figure 7. The illumination volume is formed utilizing the optical system described in chapter five, but with an updated timing diagram, Figure 30. The frame rate of the PIV camera is set to 20,000 FPS with the PIV images separated by 30 microseconds, for a 10kHz image pair recording. The CH\* chemiluminescence images are captured in between PIV recordings at a framer rate of 10,000 FPS allowing for a maximum exposure of 68 microseconds. The intensifier is capable of high repetition rate gating up to 200 kHz and can apply up to 5 order of magnitude amplification. The intensifier is timed so that its gate is open while the CH\* camera is acquiring light and closed when the camera is not recording. The gain is set at 50% of its max (2.5 order of magnitude amplification). This makes for a 10 kHz recording system which is sufficiently fast enough to acquire temporally resolved information.

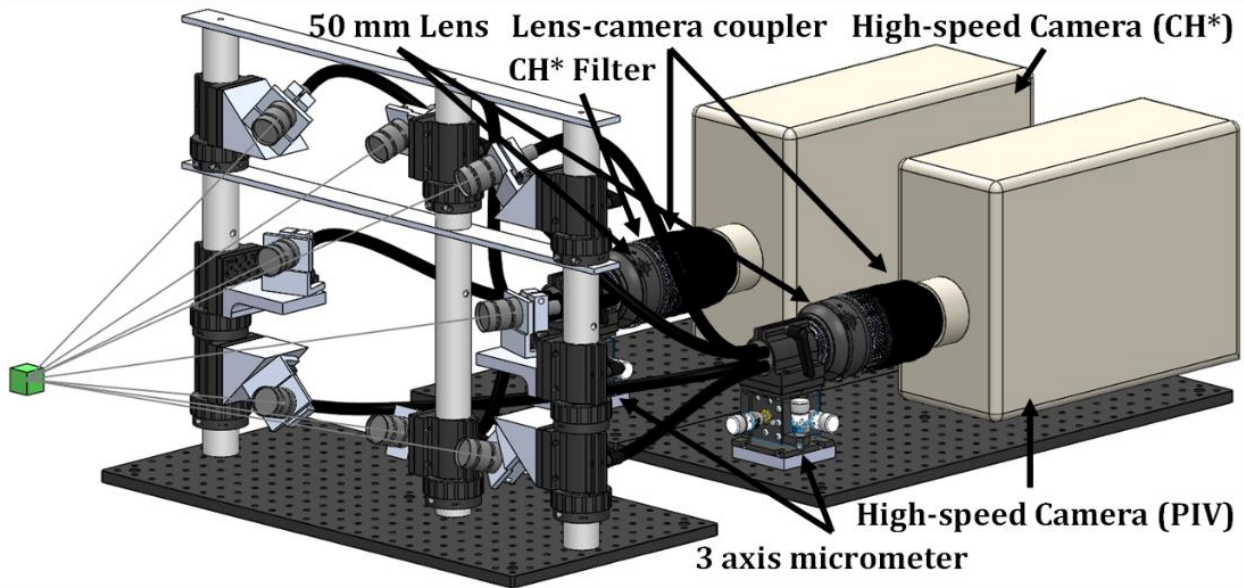


Figure 29: Schematic of the three-dimensional CH\* and PIV imaging system with key components labeled. High speed intensifier is not included in the diagram.

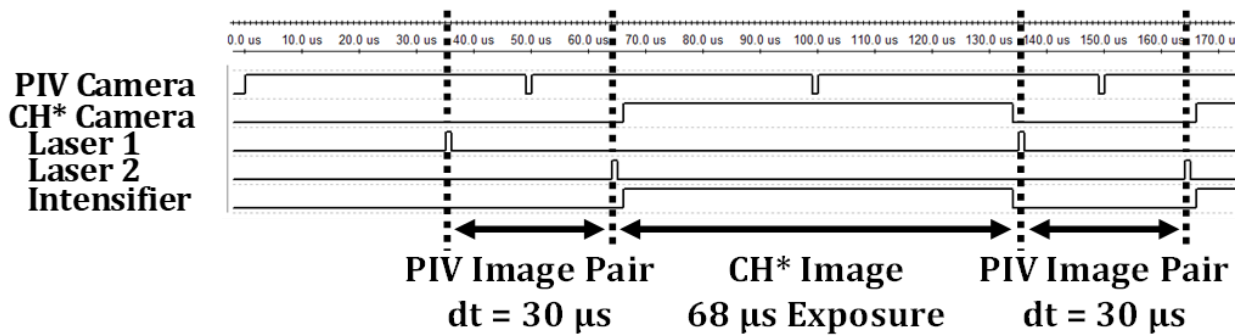


Figure 30: Timing diagram for combined three-dimensional CH\* and PIV imaging

## 9.2 Spatial Uncertainty

Before diving into the data, it is important to understand the uncertainty associated with this system down to the pixel, our final recording plane. Up to this point we have only assessed the single sensor approaches' ability in comparison to either measurements taken previously or by comparing to its two-dimensional counterpart. It has shown to be agreeable and within very small percent deviation for that matter, but now that we have reached a final design, per say, it is important to quantify its uncertainty, or rather quantify why it is agreeable.

Before starting the spatial quantification process, one assumption must be made. Spatial uncertainties associated with a pixel on the camera sensor are excluded. The camera is the acquisition device. It has its own associated spatial uncertainties that incur during manufacturing, but in the end, they are extremely small and negligible. Furthermore, the camera is what determines the physical coordinates of the image. It is the job of the fiber system to align to the camera and not vice versa. Meaning more focus should be devoted to aligning the fiber system to the image sensor properly instead of worrying about any uncertainties associated with the manufacturing of the sensor. Finally, the camera is the one component that is interchangeable. The idea is that other laboratories begin to utilize this approach with equipment that they already own and just adapt their camera for acquiring 3D images. The last assumption is that the fibers are densely packed such that there is no space in between them horizontally or vertically.

Let's begin first with the pixel. The size of a pixel on the camera's sensor is 20 x 20 microns (length by width, or  $p_l \times p_w$ ). The full sensor size is 20.48 x 20.48 mm ( $s_l \times s_w$ ) with 1024 x 1024 pixels ( $P_l \times P_w$ ). The diameter of an individual fiber ( $d_f$ ) is 10 microns. To be sure that we are accurately aligning the fiber to the pixel, the fiber bundle was designed to have close

to the same number of fibers with a square aspect ratio (1008 x 1008 fibers,  $F_l \times F_w$ , at 10.24 x 10.24 mm,  $f_l \times f_w$ ). Because this a four to one bundle, or four separate bundles being combined into one housing, there is some space between individual bundles at the combined end where there are no fibers. This is 16 fiber diameters wide ( $b_f$ ), see Figure 11B and C for an example.

For the camera sensor to visualize the fiber bundle the fiber bundle must be magnified to match the sensor size. It must be said that; this technique works most efficiently when the sensor aspect ratio and the bundle aspect ratio are the same. This work does not include a discussion on differing aspect ratio setups as it is generally not optically efficient. Since there are some sizing difference a few magnification parameters need to be observed. These are the bundle size magnification ( $M_B$ ), the fiber size magnification ( $M_F$ ), and the fiber count magnification ( $M_C$ ). The equations for these are listed below. Note that we will only be working in one dimension. For sensors with aspect ratios other than 1:1 the analysis would have to be applied for the other dimension as well.

$$M_B = \frac{s_l}{f_l} \tag{9}$$

$$M_F = \frac{p_l}{d_f} \tag{10}$$

$$M_C = \frac{P_l}{F_l + b_f} \tag{11}$$

$M_B$  in this case is 2.  $M_F$ , needs a bit of an explanation before a number is put to it. Generally, you don't try to put a square peg in a round hole, as the saying goes, but in this case, it is a must.

There are two options when matching up a circle cross section to a square cross section, one can scale the circle such that its diameter is the size of the square's diagonal (putting the square

inside the circle) or that the diameter of the circle be the size of the side of the square (putting the circle inside the square). If option one is chosen we ensure that the entire pixel is receiving a light signal, but then neighboring pixels will receive some bleed information. Also, the fiber stacking will eventually fall out of alignment with the pixels. Instead, it is better to align it such that the fiber size fits within the pixel, though we will not be utilizing the entirety of the pixel we ensure that each pixel is receiving a localized light signal dedicated to that location. These options are summarized in Figure 31. Choosing option two we arrive at a  $M_F$  of 2. Lastly, the fiber count magnification,  $M_C$ , is 1. Thus, the required magnification is 2. Let's assume though that we do not have a bundle designed to match a specific sensor. For an example, a bundle such that  $f_l = 11 \text{ mm}$ ,  $d_f = 11 \text{ um}$ ,  $F_l = 1008 \text{ fibers}$ , and  $b_f = 1 \text{ fiber}$ . These yield  $M_B = 1.82$ ,  $M_F = 1.82$ , and  $M_C = 1.01$ . In a case such as this it should be aligned such that the fiber is matched to a pixel but knowing that there will be a fifteen-pixel difference ( $P_l - (F_l + b_f)$ ). Also note that because of the densely packed assumption  $M_B = M_F$ . If  $M_B \neq M_F$ , this means that there is an associated spacing between each fiber, note that it must always be the case that  $M_B \leq M_F$ . In cases such as this it should be aligned such that  $M_B$  is used as the scaling parameter and that the fiber size will be smaller by  $p_l - d_f * M_B$ , where  $d_f * M_B$  is the final scaled fiber size. This overall lessens light throughput to the sensor but allows for higher spatial accuracy. This effect on acquisition will be discussed in the next subsection of this chapter.

To understand the spatial uncertainty in alignment the manufactures reported uncertainty for the bundles build is required. Since it has been determined that  $M_B$  is the preferred scaling parameter, the parameters for the final bundle size (not assuming densely packed) need to be formulated to calculate its spatial uncertainty when paired with the image sensor and are as such, where  $t_f$  is the distance between each fiber.

$$f_l = d_f * (F_l + b_f) + t_f * (F_l - 1) \quad (12)$$

The bundle manufacturer ensures that the bundle diameter has an uncertainty of 10 nm ( $\sigma_{d_f} = \pm 5 \text{ nm}$ ), the spacing in between individual bundle may be off by a maximum of a thousandth of a fiber diameter ( $\sigma_{b_f} = \pm 5 \text{ nm}$ ), the spacing between a fiber can range from 0 to 1 nm ( $\sigma_{t_f} = \pm 0.5 \text{ nm}$ ), and that there is no uncertainty in the fiber count ( $\sigma_{F_l} = 0$ ). The final uncertainty equation yields.

$$\sigma_{f_l} = \left( (F_l + b_f)^2 * \sigma_{d_f}^2 + (d_f + t_f)^2 * \sigma_{F_l}^2 + (d_f^2) * \sigma_{b_f}^2 + (F_l - 1)^2 * \sigma_{t_f}^2 \right)^{\frac{1}{2}} \quad (13)$$

This yields a total uncertainty of  $\pm 0.05 \text{ mm}$  in final fiber sensor size. Since this is scaled by  $M_B$  (2 in this case), which has an uncertainty of  $\pm 0.001$  (taken from the lens magnification step ring) the uncertainty of the scaled bundle is  $\pm 0.1 \text{ mm}$ . This would mean that assuming the bundle and sensor are matched perfectly there would be uncertainty of 5 thousandth of a pixel in fiber to pixel alignment.

Recall though that the proximal housing is on a 3-axis micron stage. The stage allows for 1 micron increments in x, y, and z directions. The z direction is used to focus, so it does not affect the alignment. Because the stage allows for micron increments, this correlates to alignment uncertainties of  $\pm 0.5 \text{ um}$  in both x and y directions, or a total uncertainty of  $\pm 1 \text{ um}$ . This results in an alignment uncertainty of 5 hundredth of a pixel. Combining the uncertainty from the bundle and the alignment stage there is a total uncertainty of  $\pm 0.055$  of a pixel in fiber to pixel alignment. This gives high confidence in proper fiber to pixel comparison.

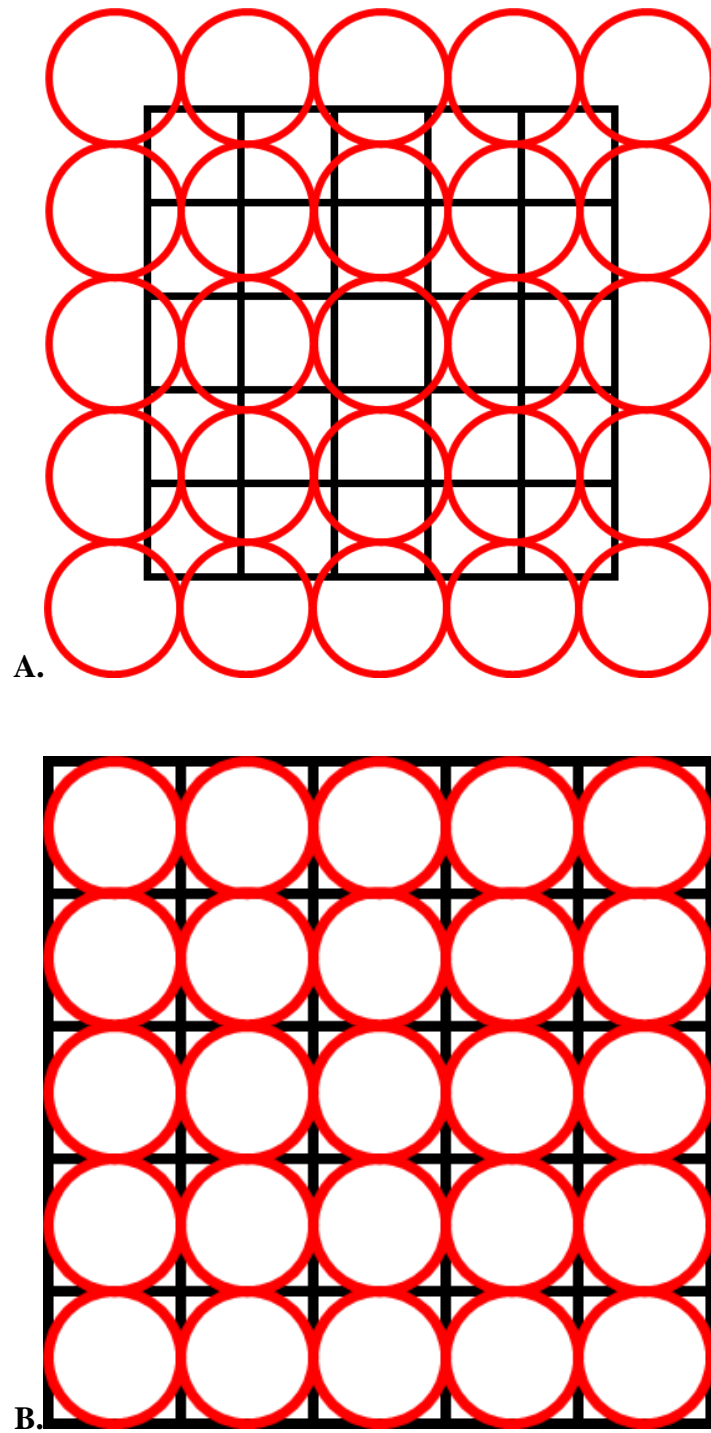


Figure 31: Options for choosing fiber size magnification. A. Choosing scaling such that the fiber diameter is the size of the pixel diagonal. B. Choosing scaling such that the fiber diameter is the size of the pixel side (preferred).



### 9.3 Light Transmittance

The last aspect that needs to be discussed in characterizing the system is its ability to capture light. The components associated with light capture are the distal lenses, the fiber bundle, the proximal lens, the CH\* filter, and the fiber to pixel alignment. To begin the camera has its own associated sensitivity across the light spectrum (100 to 1000 nm). We are interested in two wavelengths, 427 nm (CH\*), and 532 nm (PIV). Similar to the analysis in section 3.3, we see the camera captures 50% of its full-scale at 427 nm, and 75% of its full-scale at 532 nm. We will use an equation like equation 7 to deduce the total light transmittance percentage. The bundles have a light transmittance percentage (reported from the manufacture) of about 50% at 532 nm and 40% at 427 nm. The lenses have a light transmittance of 99.1%, and the filter has a transmittance of 99%. As mentioned in the previous section an individual fiber does not cover the entire pixel. By including the alignment uncertainty and taking in the difference in areas there can be a minimum transmittance of 90%. Using equation 14, we arrive at a total light transmittance of 35% at the 532 nm wavelength and 16% at 427 nm. Though there is quite a bit of loss at 532 nm the laser provides sufficient power to illuminate the entire volume without the need for intensification. Because of the low light transmittance at 427 nm an intensifier is required to amplify the incoming light signal.

$$\sigma_{\lambda} = 100 * \eta_{distal\ lens} * \eta_{bundle}(\lambda) * \eta_{proximal\ lens} * \eta_{CH*Filter} * \eta_{alignment} * S_{\lambda} \quad (14)$$

To conclude this chapter, please note that distal end alignment uncertainty associated with imaging a region of interest has been discussed in detail in section 5.3. The system produced a spatial uncertainty of 0.05  $\mu\text{m}$ . This reiterates the importance of proper fiber to pixel alignment. Such a low spatial uncertainty is achieved only when there is high alignment confidence.

## CHAPTER TEN: SIMULTANEOUS THREE-DIMENSIONAL CH\* IMAGING AND PIV

What is left to be done now that the system has been characterized, is to use it. The system is used to simultaneously acquire three-dimensional species and velocity information on a bluff body stabilized flame. This chapter will discuss in detail some of the aspects of the flame associated with the experiment to demonstrate its capabilities.

### 10.1 Experiment Description

Figure 32 shows a schematic of the facility used to perform simultaneous 3D flame and PIV. The facility is essentially two concentric cylinders with the outer cylinder equipped with a nozzle that has an exit diameter of 27 mm, and a bluff body, 12 mm in diameter, mounted in the inner cylinder extending past the nozzle exit by 5.5 mm. The blockage ratio between the nozzle exit and the bluff body is 0.44, but due to the bluff body being extended out from the nozzle face the flow is allowed to expand slightly before the end of the bluff body. The facility has been coined as the VAG (Vitiated Axial Gas) burner by the students in the Propulsion and Energy Research Laboratory at the University of Central Florida. Though for this work, the flow is not vitiated. The facility is provided with premixed propane fuel and air in both cylinders through the use of air and gas flow meters to control the equivalence ratio and is spark ignited. The flow is metered so that the non-reacting bulk velocity is 15 m/s. The experiment is oriented so that the base of the bluff body is just outside the illumination volume and is centered with the measurement domain, see Figure 33. The inspection volume for this experiment was 30 x 30 x 30 mm which was sufficient to capture the flow field associated with the nozzle and 12 mm bluff body. The tomographic data is taken using the timing diagram displayed in Figure 30. The results are divided into three sections: non-reacting, reacting, and capture of a blow off event.

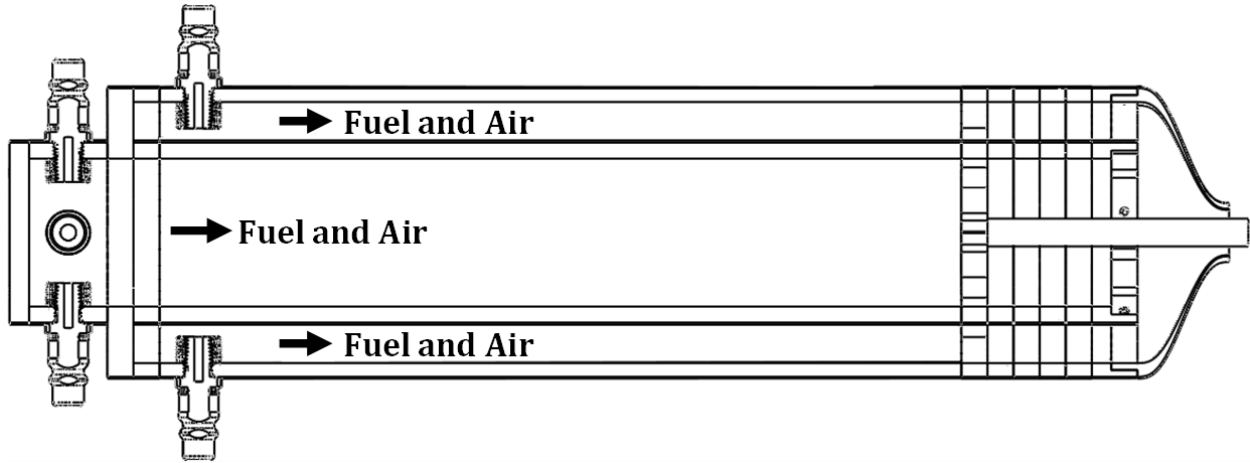


Figure 32: Diagram of the VAG burner in all its glory.

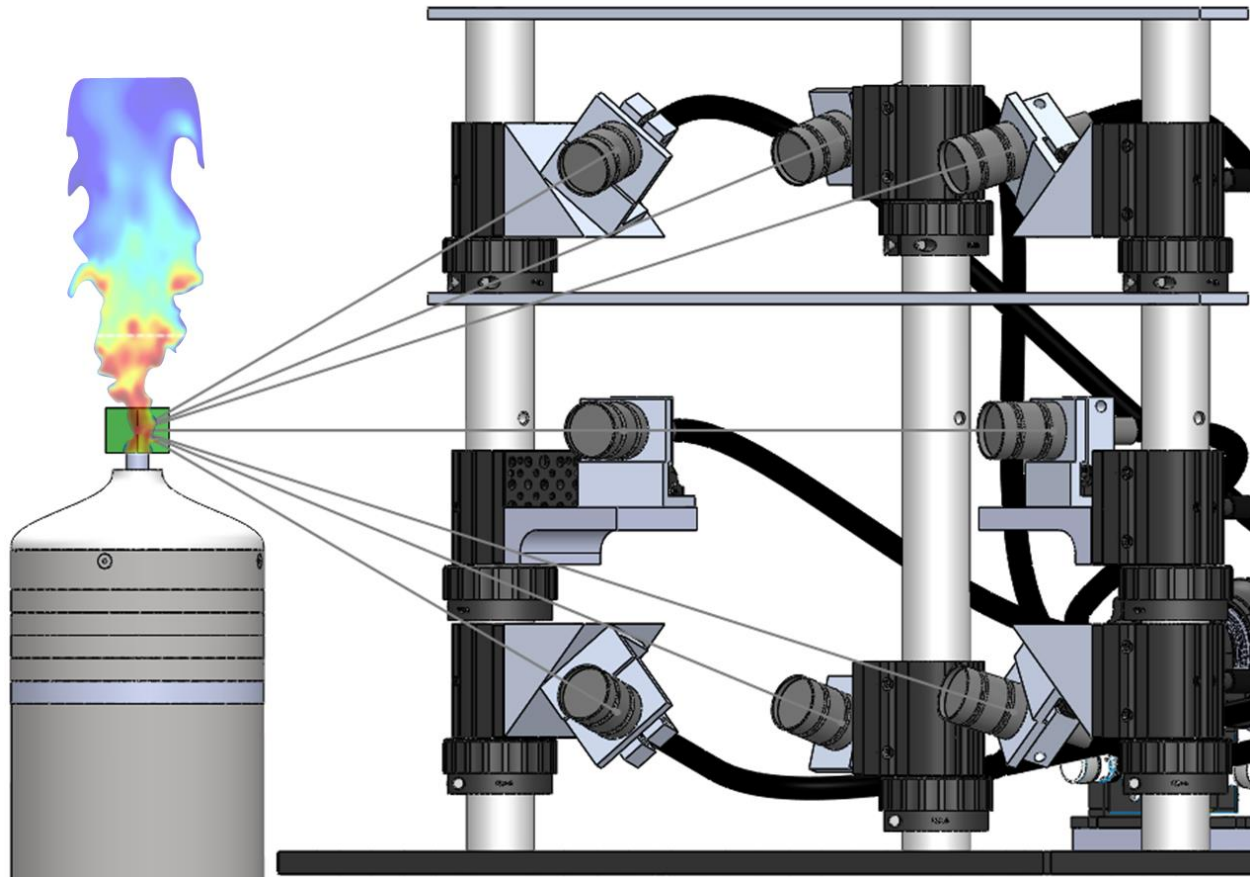


Figure 33: Orientation of the experiment relative to the tomographic imaging system.

## 10.2 Non-Reacting

Before we can begin analysis of a flame we must first understand the flow field we are working with. It is generally easier to interpret flow topologies visually with two-dimensional data, but the same does not translate well to three-dimensional data. The flow topology is somewhat similar to the bluff body explored in section 8.2, with key difference being that the bluff body is axisymmetric instead of two dimensional.

Figure 34 displays the mean axial velocity associated with the non-reacting flow field at the centerline of the bluff body. Because the seeding density is high the recirculation region is not captured as clearly in the axial velocity field, but it is easily extracted from other variables such as the vorticity and cross plane velocity. The flow behaves as expected with low velocity regions associated with the outside of the jet and high velocity regions between the bluff body and the edge of the nozzle. What is not easily noticed in Figure 34 is the slight dip in velocity at the center of the jet. This is due to the velocity being slowed down in the center by the bluff body. To capture this more clearly various velocity profiles are plotted at multiple spanwise locations in Figure 35. Figure 35A displays multiple velocity profiles from -10 to 10 mm and provides an isometric view of the profile where the dip is noticed only in the three center profiles (blue, black, and green lines). This dip of 3 m/s is only noticed in the range of -6 to 6 mm in the spanwise (z) dimension. This just under one bluff body height. Meaning that, this lower speed region is induced by the bluff body. In Figure 35B, where the plot displays a side view of the profiles plotted from 0 to 10 mm in the span, we see the dip also spans -6 to 6 mm in the cross plane (x) dimension. This displays the axisymmetric nature of the experiment. From Figure 35B, the flow fields profile, or its tapering as the observed velocity plane is moved towards the edge of the inspection volume, can be extracted.

The cross plane and span wise velocity give further insight into the description of the flow field. The mean flow field topologies at the centerline of the bluff body are seen in Figure 36. Note that though the cross plane and span wise topologies are slightly different there is a general trend of opposing velocities at about 2 m/s centered about the bluff body. Overall, they show similar trends in capturing the axial nature of the flow field.

Tomographic reconstruction tends to yield less accurate results in the span versus the axial and cross plane information due to the nature of the MART algorithm and imaging approach. To acquire more accurate span wise information more iterations of the MART algorithm would need to be performed. For the sake of processing time, though, only three iterations of the algorithm are performed for these data sets leading to what appears to be smeared information in the span. This does affect accuracy, but the goal of this work is to demonstrate the capabilities of the tomographic system. Figure 36C shows the mean span wise velocity if 100 MART iterations are used to reconstruct the span wise information. This drastically increased processing time from a few days to weeks for a single sample set. Because of the vast difference in processing time and to quickly go through large amounts of data efficiently only 6 iterations of the MART algorithm are used for the reacting data sets in the proceeding section.

Figure 37 brings the mean velocity components together into one plot. The XY slice is the cross plane velocity  $V_x$ , the YZ slice is the span wise velocity  $V_z$ , and the isosurface is of the axial velocity, along with streamlines to orient the observer of the flow direction. This combined plot allows for the depiction of the recirculation zone that is seen just behind the bluff body and is just over one bluff body height in length. The full 3D flow topology associated with the mean field as discussed with the two-dimensional information is seen here: The velocity dip due

induced by the velocity, the velocity profile tapers as we move towards the edge of the inspection domain, the counter-rotating in the cross-plan and span-wise velocities, and the recirculation zone.

The vorticity field provides a detailed description of the rotations happening in the flow. In Figure 38 we see the three components of vorticity. As expected  $z$  vorticity dominates the  $XY$  plane and  $x$  vorticity dominates the  $YZ$  plane and have very similar flow topologies. In both  $z$  and  $x$  vorticities counter-rotating rotations are seen induced by the bluff body and by the outer shear layer associated with the 27 mm nozzle. Most notably, though we are capturing the  $y$  vorticity which is zero on the horizontal and vertical axis but alternating positive/negative at 45-degree angles from either the horizontal or vertical axis. Figure 39 compiles the vorticity information into one plot, which displays the overall vortex structures associated with the experiment. This also gives insight into the size of the recirculation zone. Here it is seen to be 13 mm in length (about one bluff body height) with a 12 mm diameter at its base and tapers down to 2 mm in diameter at its close-out region. Figure 40 shows an instantaneous snapshot of the vorticity where an instance of Von-Karman vortex shedding can be seen. This is important to capture as the goal of this system would be to do detailed time-resolved three-dimensional analysis on flow fields.

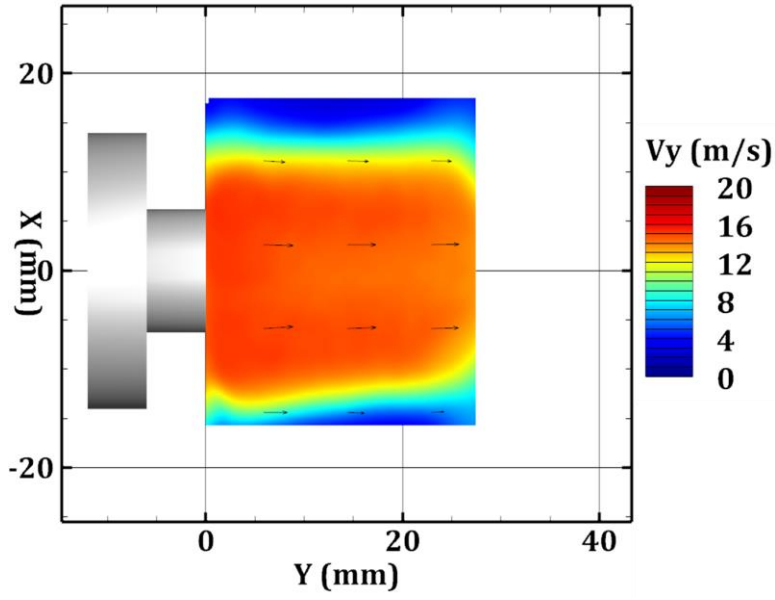


Figure 34: Mean axial velocity associated with the experiment. Outlined in grey are the nozzle exit and bluff body.

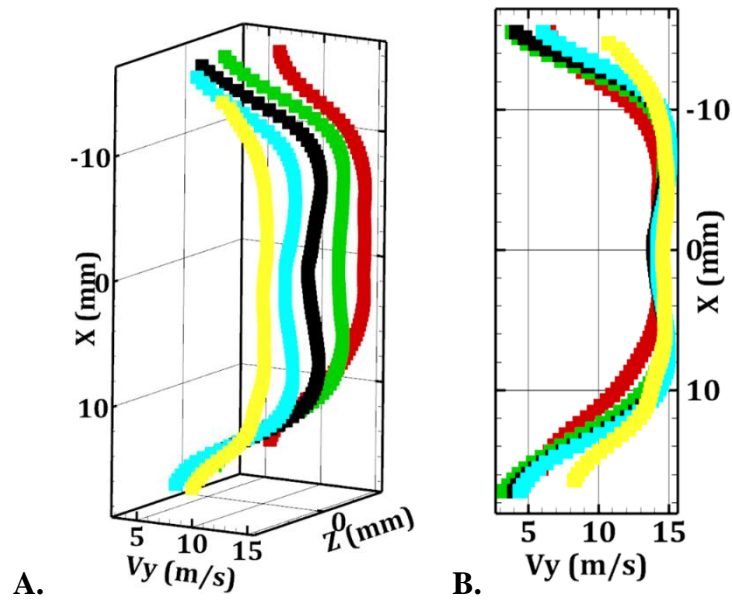


Figure 35: Mean axial Velocity profiles at various spanwise locations. A. An isometric view of the profiles plotted from  $z = -10$  to  $10$  mm. B. Side view of all the profiles plotted from  $z = 0$  to  $10$  mm.

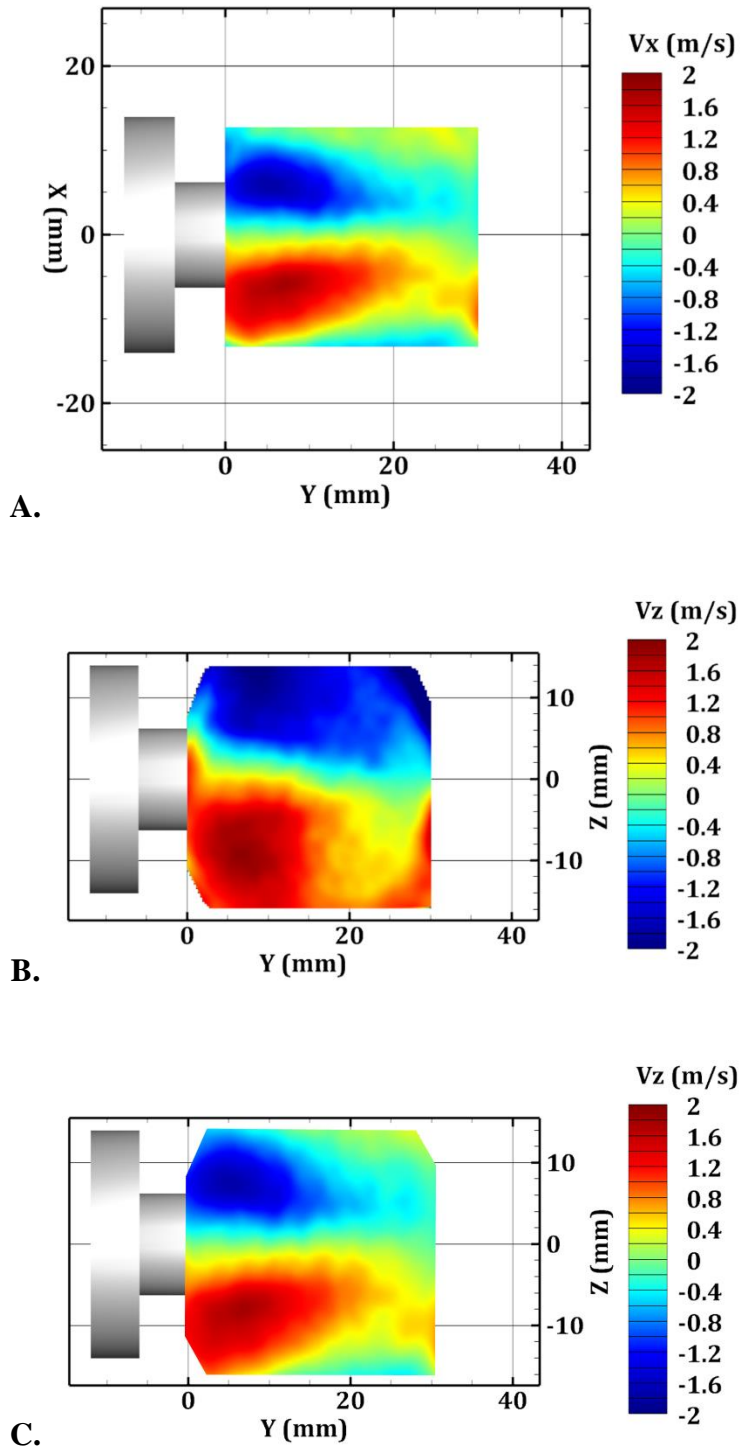


Figure 36: A. Mean cross plane velocity at the centerline of the bluff body. B. Span wise velocity at the centerline of the bluff body. C. Span wise velocity after 100 MART iterations along the centerline of the bluff body.



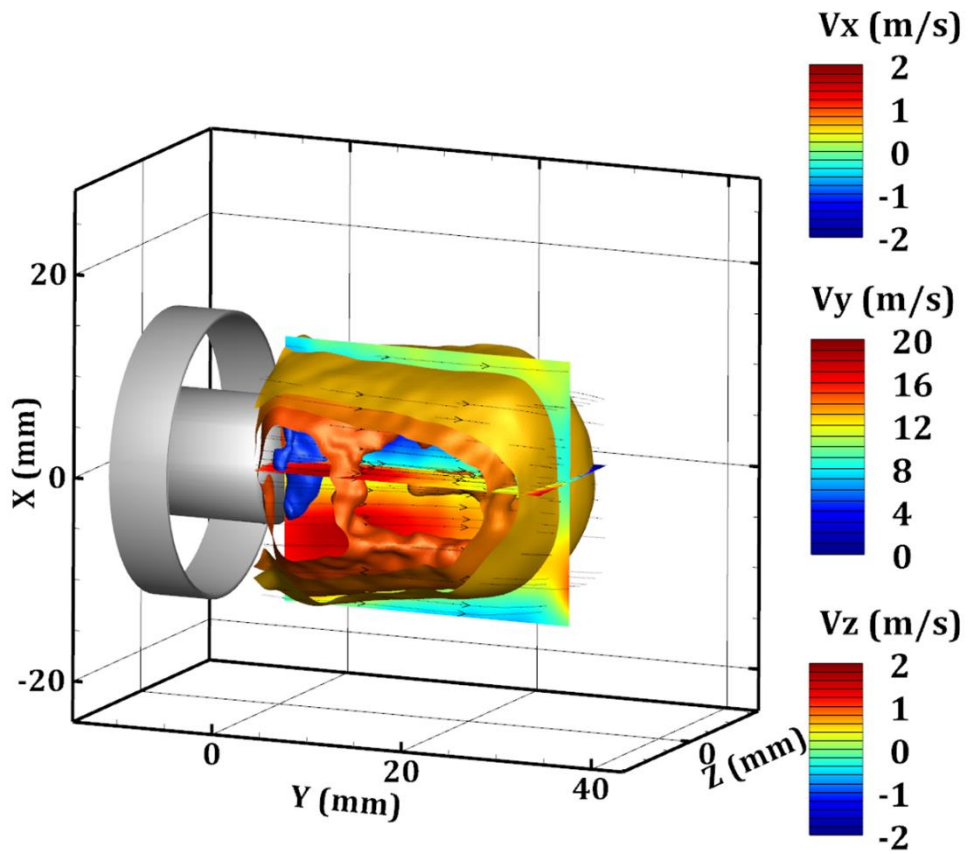


Figure 37: Combined mean velocity components. XY slice is  $V_x$ , the isosurface is of  $V_y$ , and the YZ slice is of  $V_z$ .

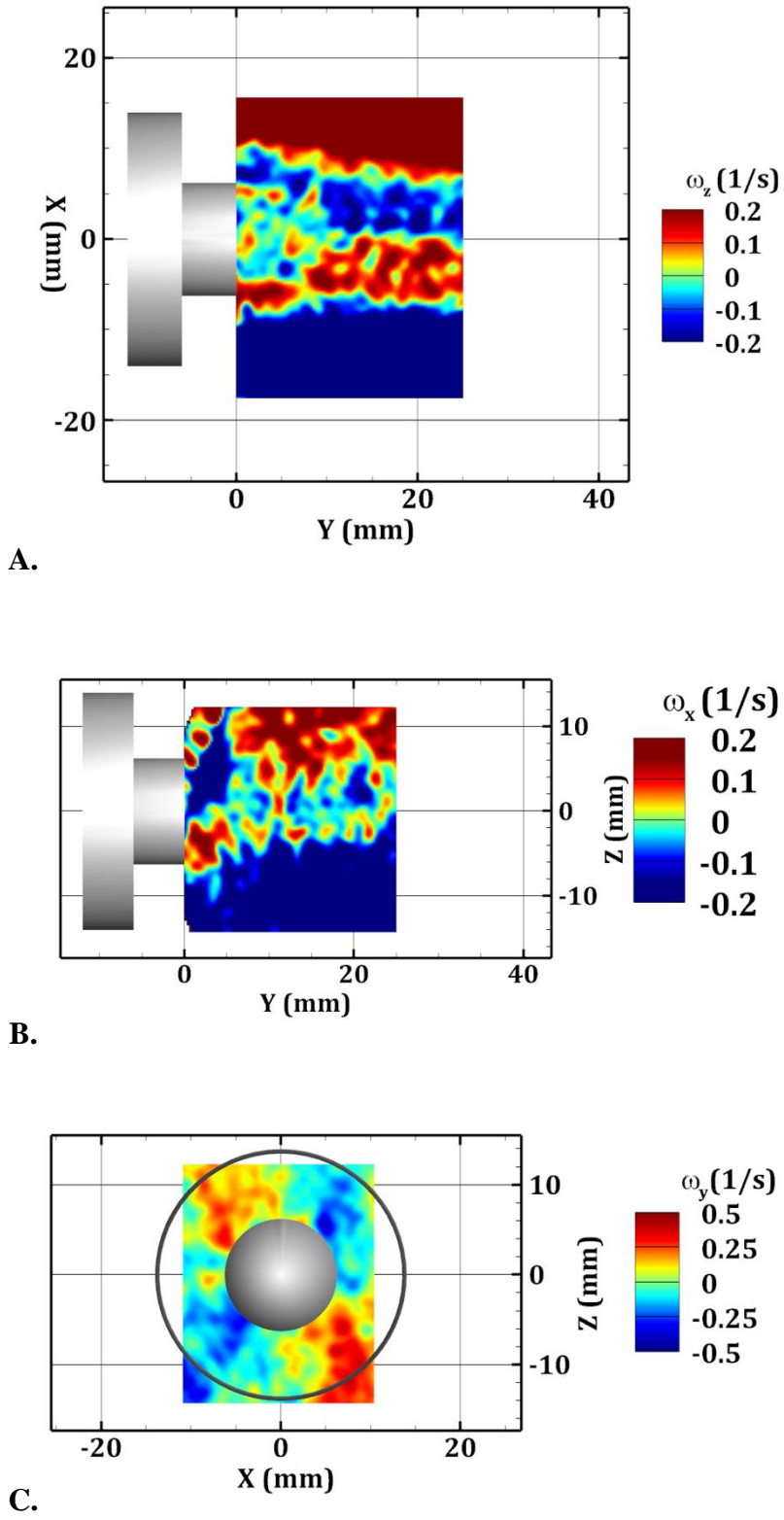


Figure 38: Components of vorticity. A. about z, B. about x, and C. is about y

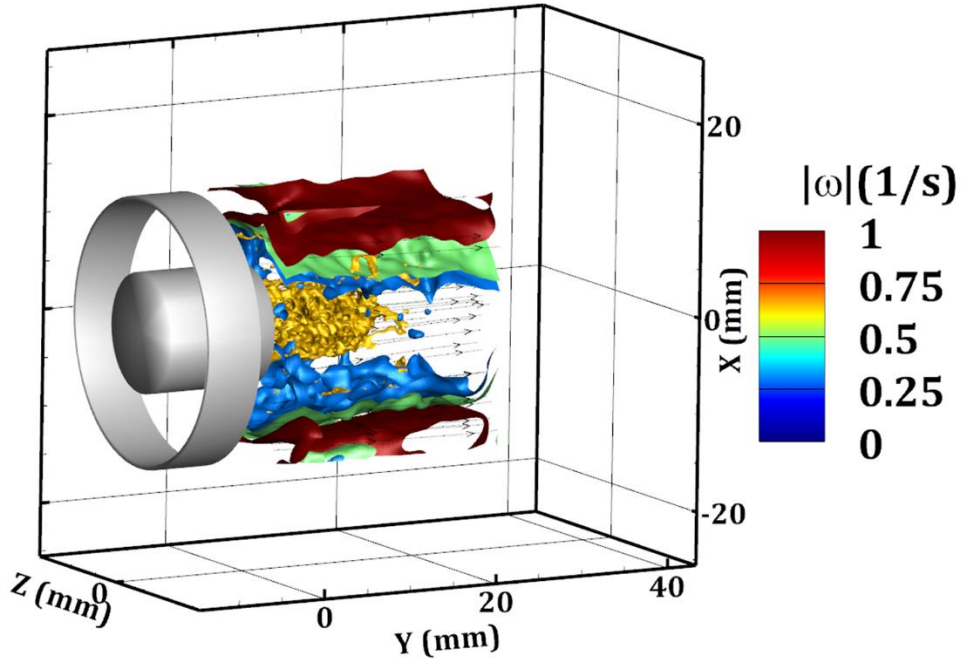


Figure 39: Mean vorticity magnitude

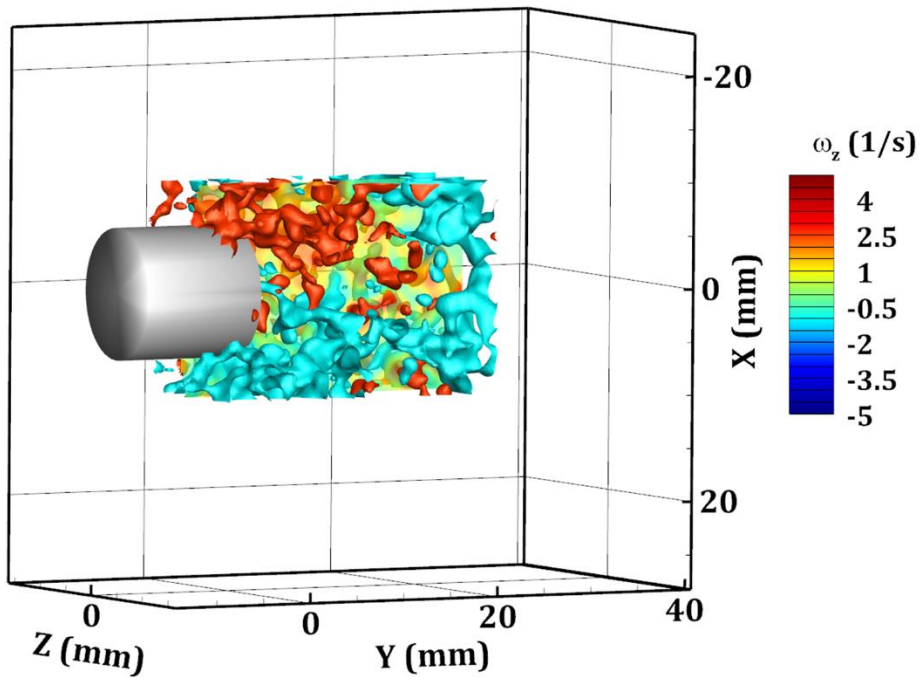


Figure 40: Instantaneous snap shot of the vorticity magnitude colored by the  $z$  vorticity

### 10.3 Reacting

With the general flow field understood, the facility was premixed with propane-air and then ignited at an equivalence ratio of unity. The recording captured the CH\* signal of the flame and PIV simultaneously. 6 SMART iterations are used to reconstruct the flame images. Two types of data are taken.

Figure 41 shows the reconstruction of an instantaneous snapshot of the CH\* species associated with the flame. This information not only allows for the location of the reaction zone, but also allows for the extraction of the flame thickness. To get a better understanding of the flame's overall topology, a mean of 2000 samples was taken, see Figure 42. This gives a glimpse as to the overall expected location of the flame front. Figure 43 and Figure 44 show the calculated mean vorticity fields from the PIV data associated with flame. They show very similar behavior at both the centerline and outer edge of the bluff body, where we see a weakening of the vorticity induced by the bluff body. To be acclimated with overall topology of the flow field associated with the flame, Figure 45 displays the mean axial velocity profile and overlaid with the vorticity. This shows the location of the recirculation zone and the location of the high velocity region of the flame.

We could approach the PIV data in a manner as rigorous as 10.2, but it is not necessary for this work. What is of interest is the possibilities one can achieve by coupling the two measurements, 3D flame and PIV. Figure 46, shows the mean axial velocity profile overlaid onto the mean flame. Here we can notice a few things. We can see the lower velocity core of the flame and the higher velocity region are tightly wrapped around the reaction zone of the flame. This show that as the products are leaving the reaction zone and being burnt they accelerate.

Similarly, Figure 47 shows the mean three-dimensional vorticity overlaid onto the mean flame. Here we can see the opposed vortex structures and how they wrap tightly around the reaction zone of the flame. Shown as well, is the location of the outer shear layer induced by the 27 mm nozzle. It is important to note that in the region of interest the flame does not interact with the outer shear layer, so that analysis can be focused on bluff body effects.

Another benefit of the coupling of these two measurements is the extraction of the three-dimensional flame front thickness. Shown in Figure 48 is an instantaneous snapshot of the flame with the vorticity profile and the flame edge extracted at  $z = 0$  mm where a progress variable has been used to dictate the location of the reaction zone. This progress variable is then scanned through the span and the flame edge is extracted at each plane. This very useful for the calculation of the physical phenomena occurring at the reaction zone such as local three-dimensional strain, acceleration due to the reaction, etc. Figure 49 shows a few instantaneous snapshots of the PIV information overlaid onto the flame. Here we can see how the vorticity effects the flame wrinkling. Outlined in yellow on the first frame is vortex structure. As we proceed through time we see how the propagation of this structure affects the wrinkling of the flame until the structure exits the inspection volume. As the positive vortex structure exits the frame we start to see the onset of a negative structure entering the flame that will wrinkle the flame back in the opposite direction. This cycle will continue throughout the recording displaying the oscillatory behavior of the flame.

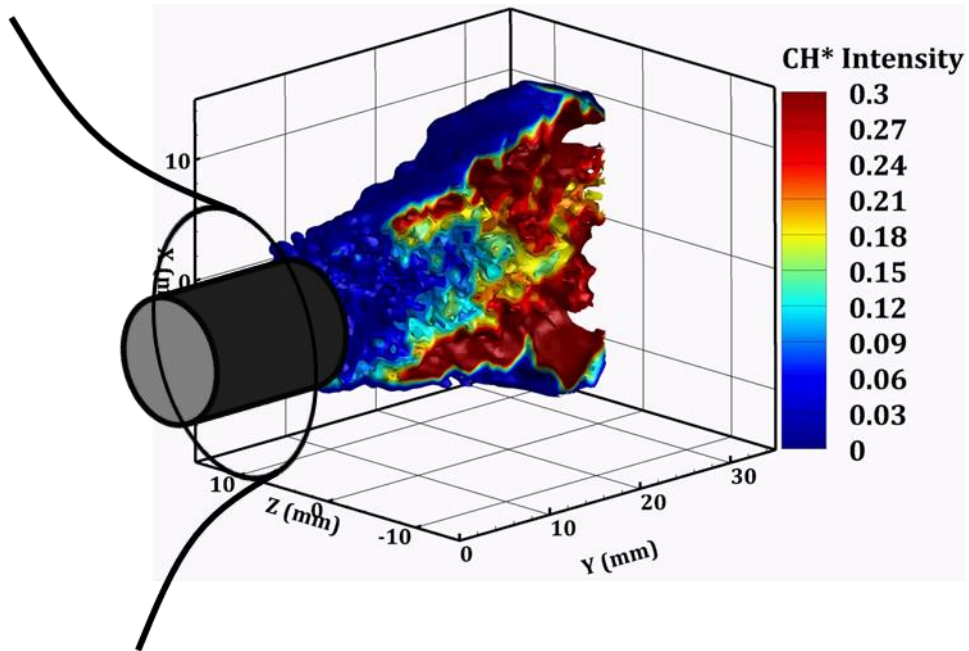


Figure 41: Instantaneous Snapshot of the CH\* species

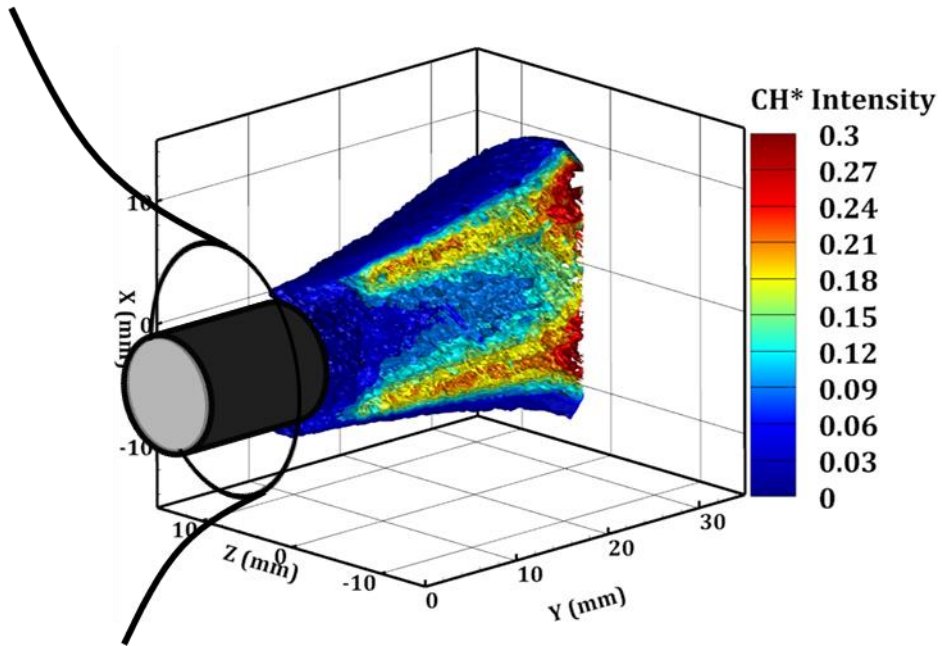
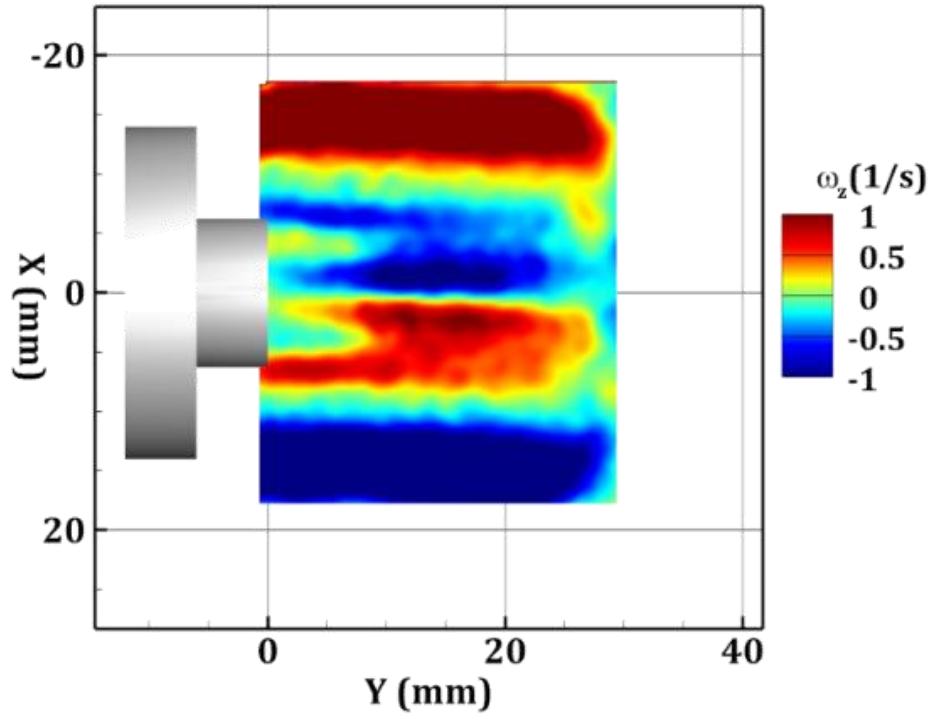
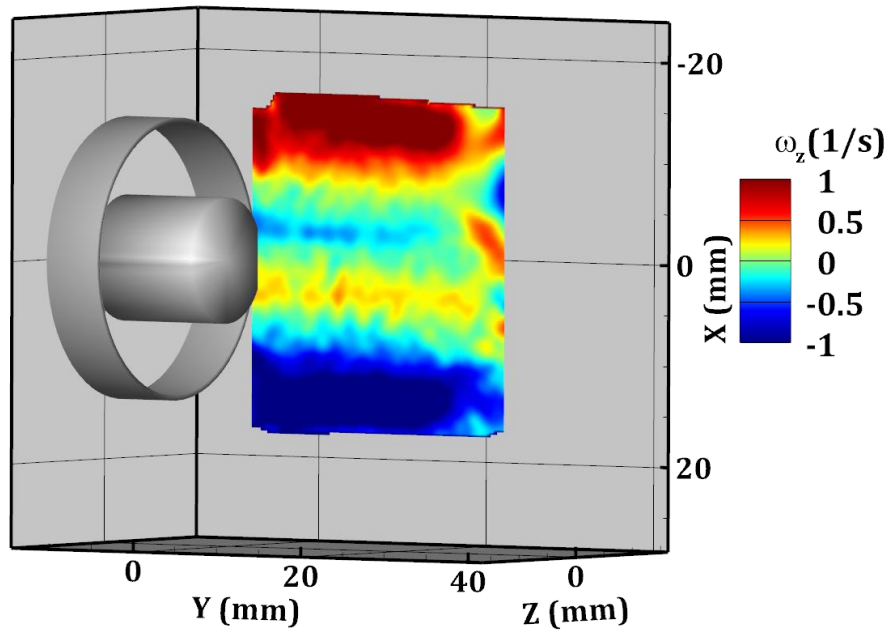


Figure 42: Mean CH\* tomographic reconstruction



A.



B.

Figure 43: Mean cross plane vorticity at A. the centerline of the bluff body and B. the outer edge of the bluff body

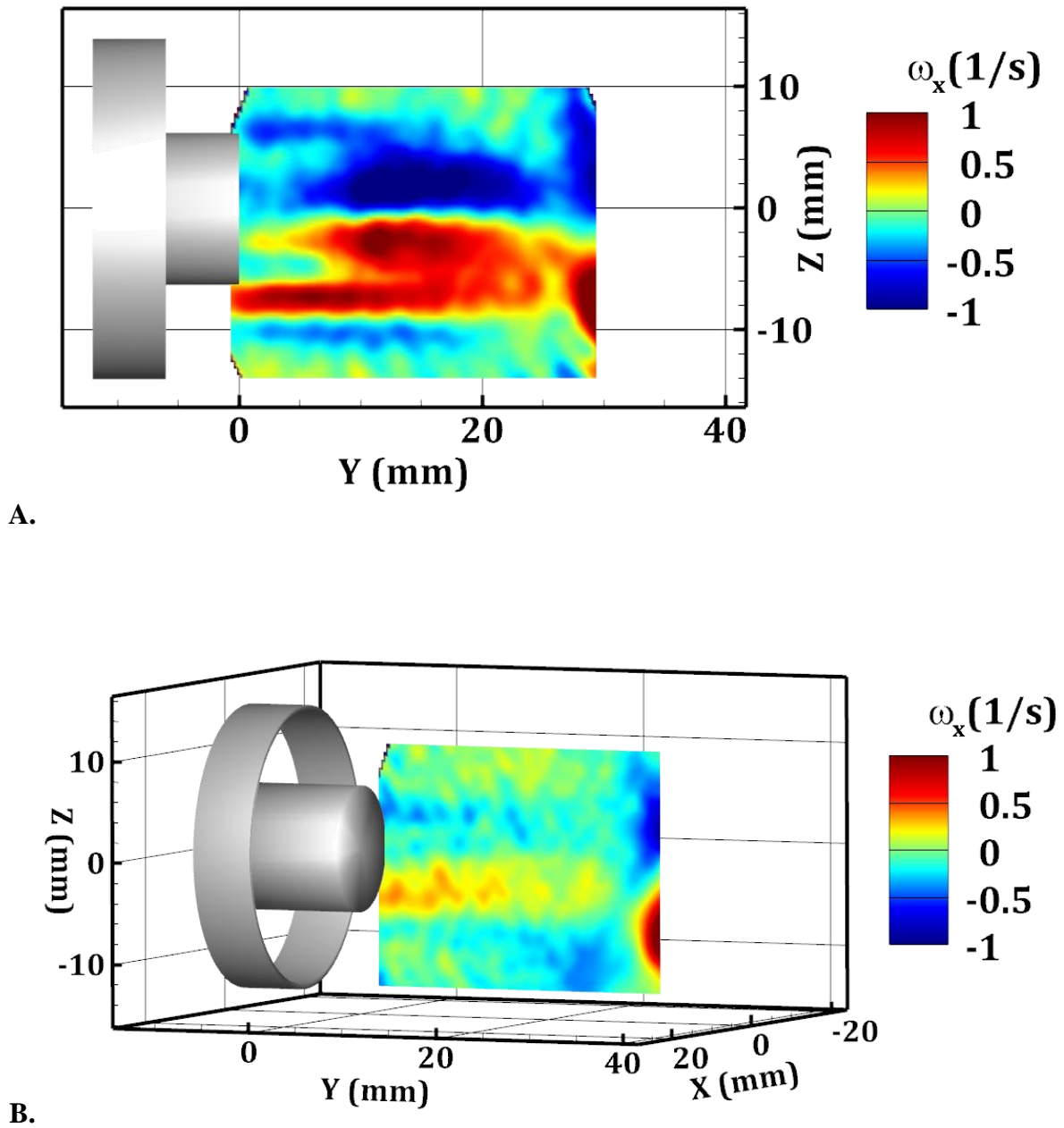


Figure 44: Mean span wise vorticity at A. the centerline of the bluff body and B. at the outer edge of the bluff body



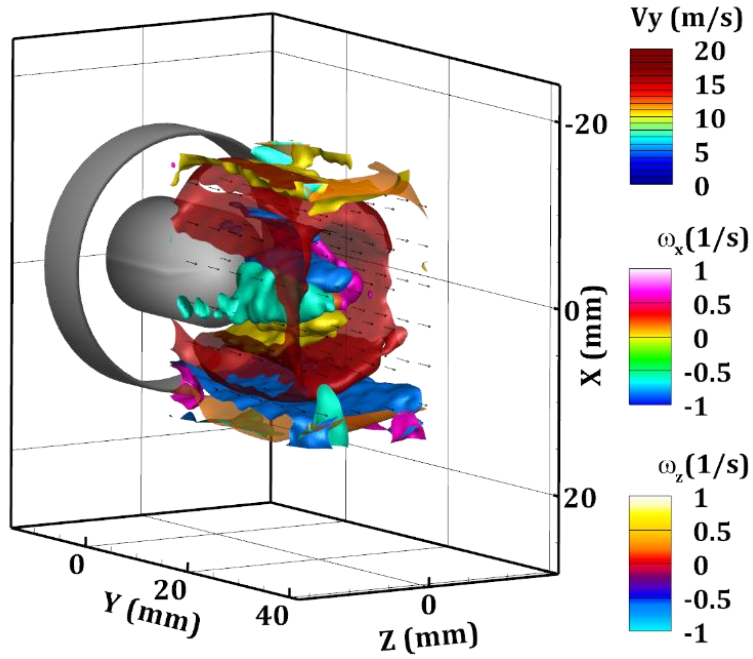


Figure 45: Mean three-dimensional axial velocity profile, cross plane vorticity, and span wise vorticity overlaid from the PIV data.

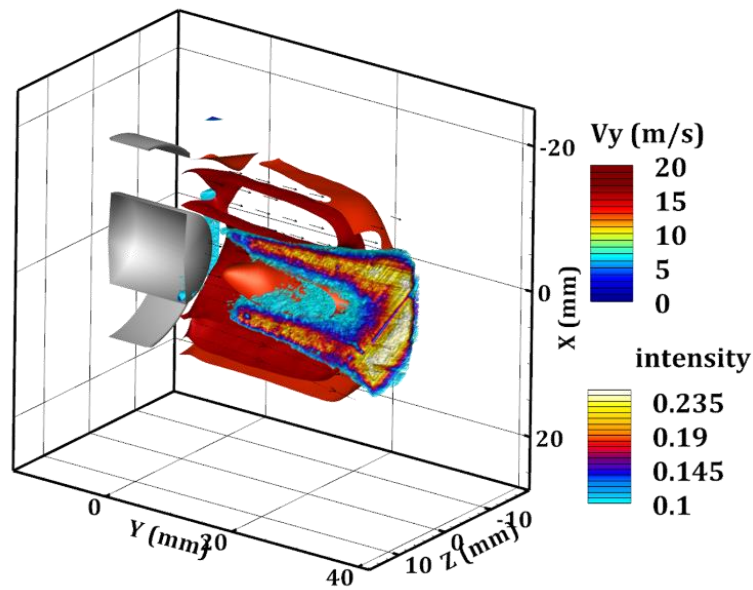


Figure 46: Mean three-dimensional axial velocity overlaid with the mean of the CH\* measurement.

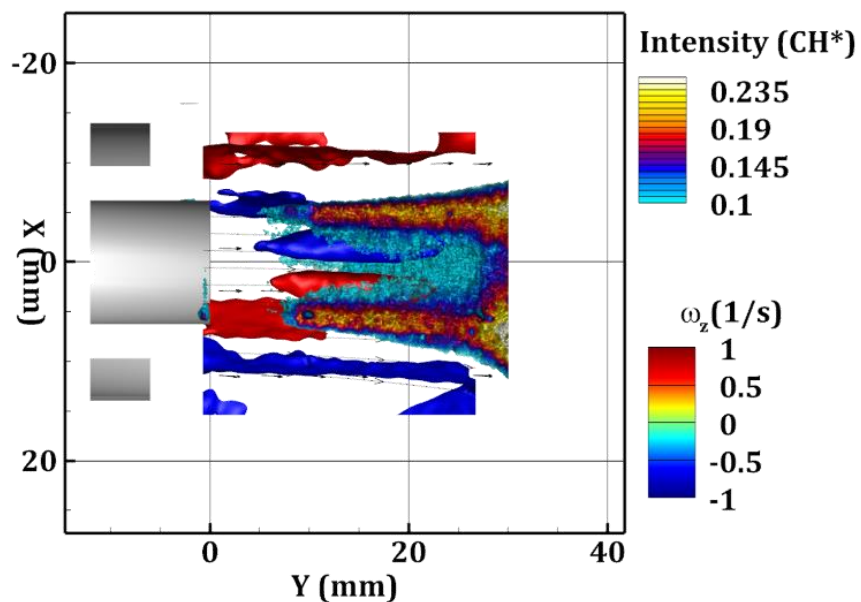


Figure 47: Mean three-dimensional cross plane vorticity overlaid with the mean CH\* intensity of the flame

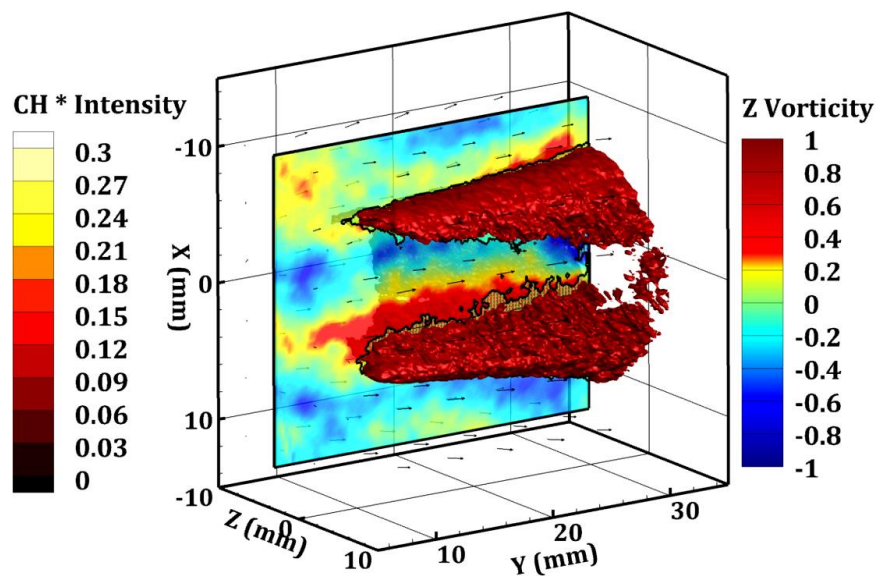


Figure 48: Extracting the edge of the flame on an instantaneous snapshot overlaid with the vorticity field

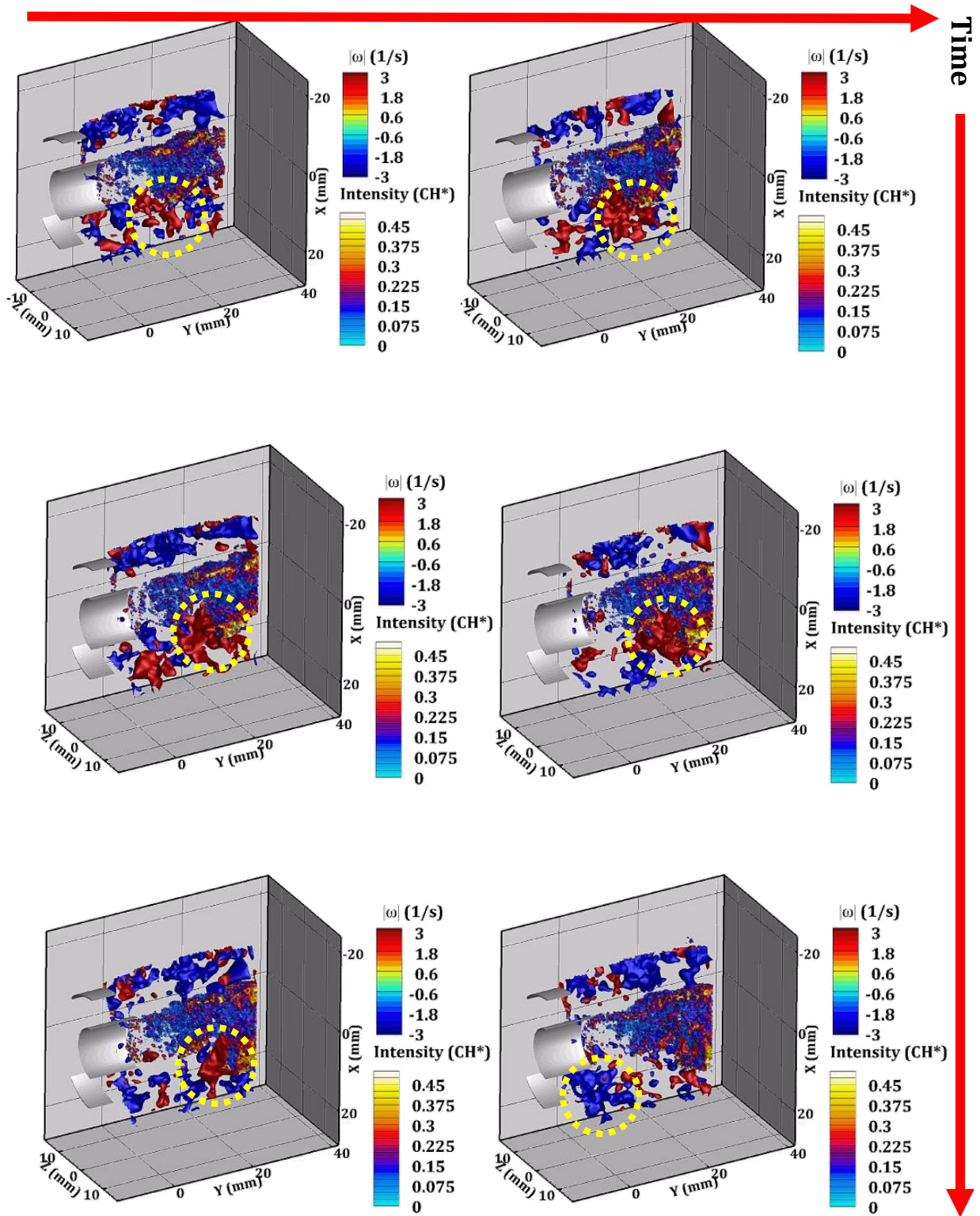


Figure 49: 6 Instantaneous snapshots of a vortex wrinkling the flame

## 10.4 Capturing a Blow Off Event

To demonstrate the capabilities of capturing three-dimensional, temporally resolved information a recording of a blow off event is captured. The blow off event is produced by starving the flame of fuel and timing the start of the recording accordingly to capture the flame as it blows off. Figure 50A shows the raw image from the recording where the first flame hole begins to appear and Figure 50B is the reconstruction of this frame. Despite the fact that this is a high noise scenario we are still able to reconstruct the frame and capture the three-dimensional flame topology. By coupling the reconstruction with the PIV data, it is possible to calculate the vorticity at the necking point of this flame where the flame hole is appearing. Figure 51 is a rotated view of Figure 50B with the vorticity field overlaid. You can see that at this necking point of the flame there are two counter opposed vortex pairs causing a strain on the flame. As we move forward in time, closer to point of a full blow out we start to see that these vortex pairs grow in size and strength and begin to display von-Karman vortex behavior. Figure 52 displays an instance close to full blow out where there is a larger flame hole. By looking at the vorticity field we see that in comparison to flame hole in Figure 50 these pairs are much larger and exhibit behavior closely related to von-Karman vortex shedding. This would insinuate that the flame front is seeing large amounts of strain from the shear layer induced by the bluff body. The isosurface of the vorticity is plotted in Figure 53 and shows the three-dimensionality of the vorticity field. Here it is seen that the vortex structure has a width on the order of one bluff body height. This again insinuates that the behavior displayed in the non-reacting data is beginning to induce high amounts of strain on the flame, causing these large flame holes and ultimately blowing off the flame.

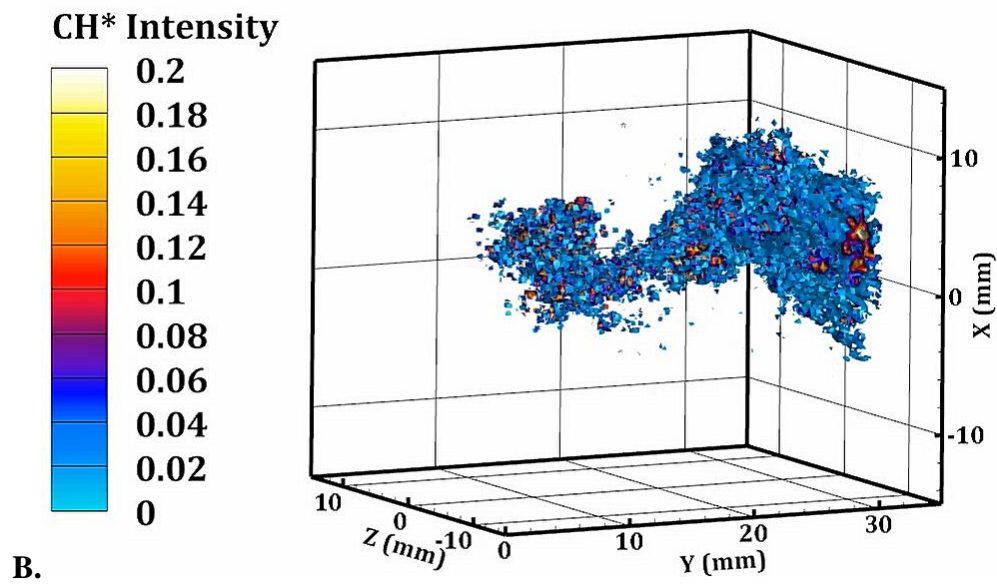
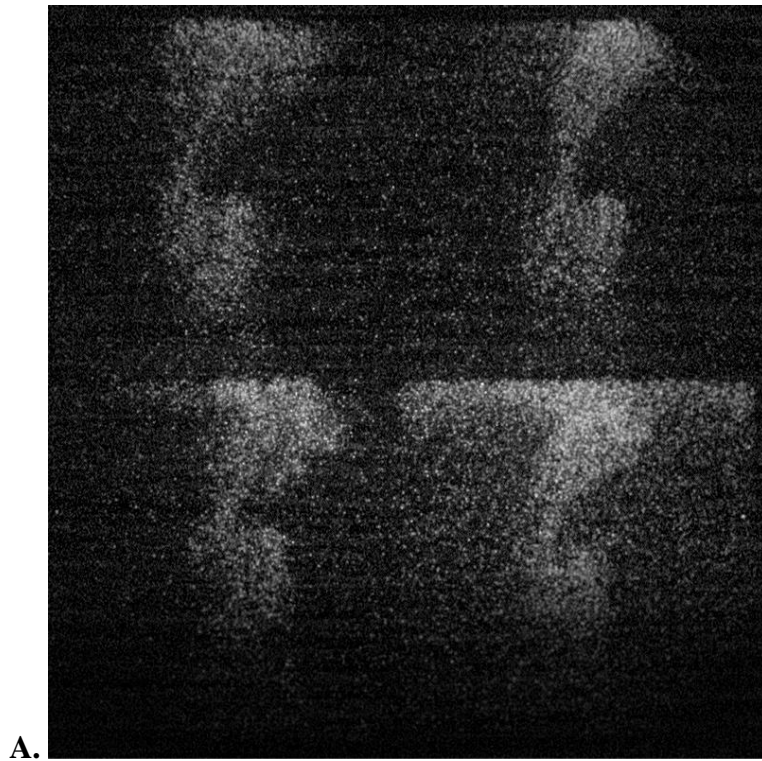


Figure 50: Instantaneous snapshot where the flame is beginning to produce flame holes. A. is the raw data and B. is the three-dimensional reconstruction.



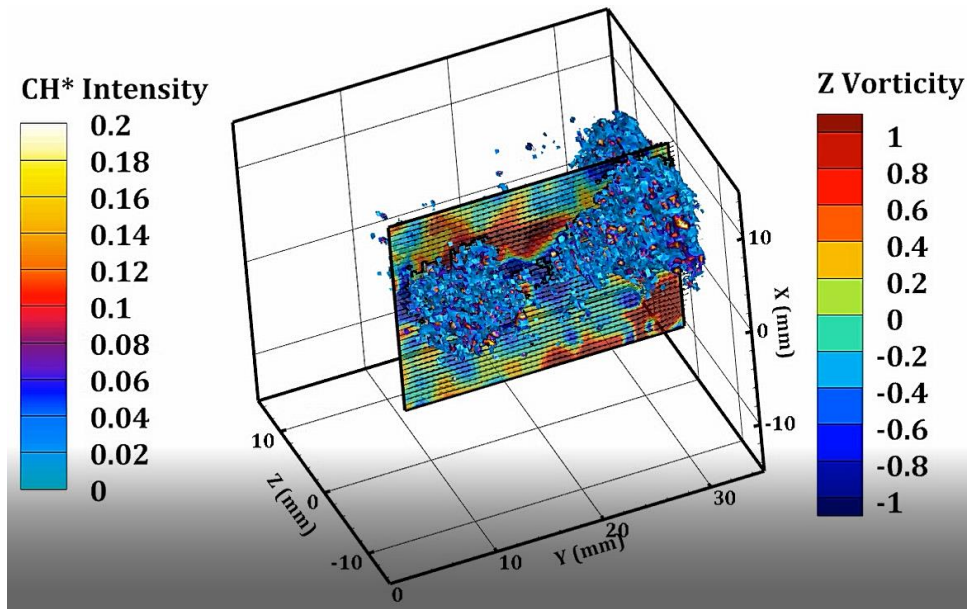


Figure 51: Rotated view of Figure 50B overlaid with the cross-plane vorticity

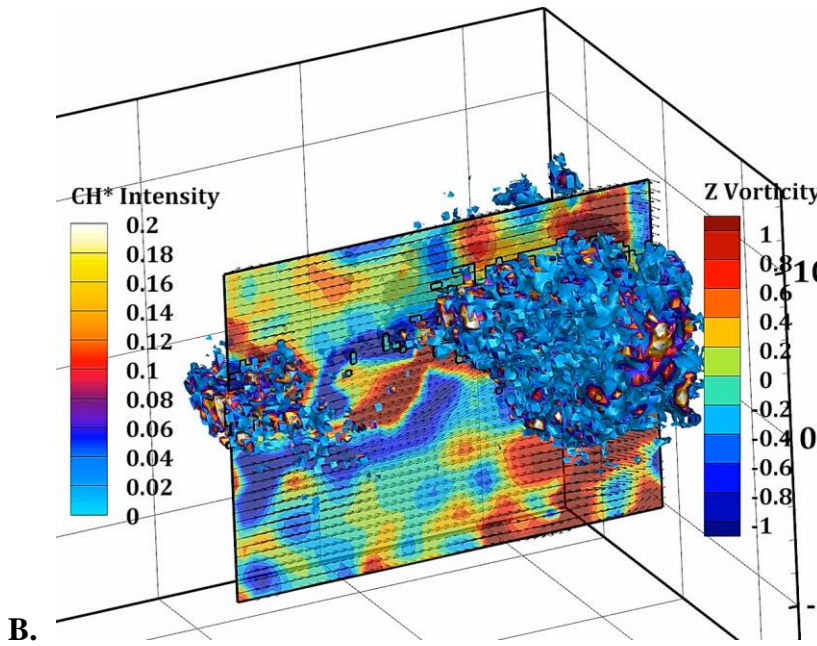
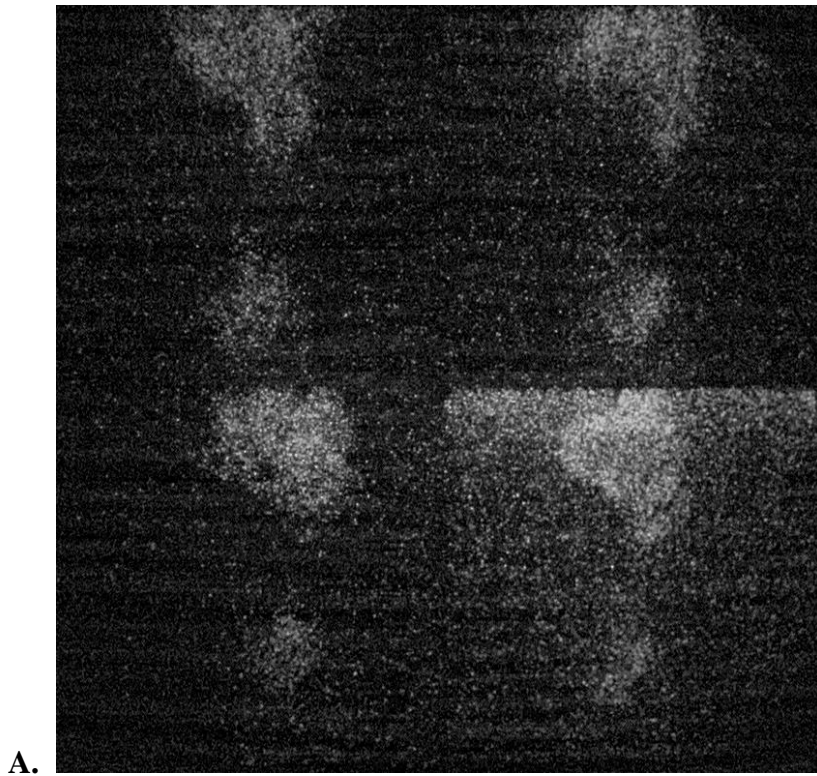


Figure 52: Three-dimensional reconstruction of a flame hole associated with the blow off data.

A. is the raw data and B. is the three-dimensional reconstruction overlaid with the vorticity

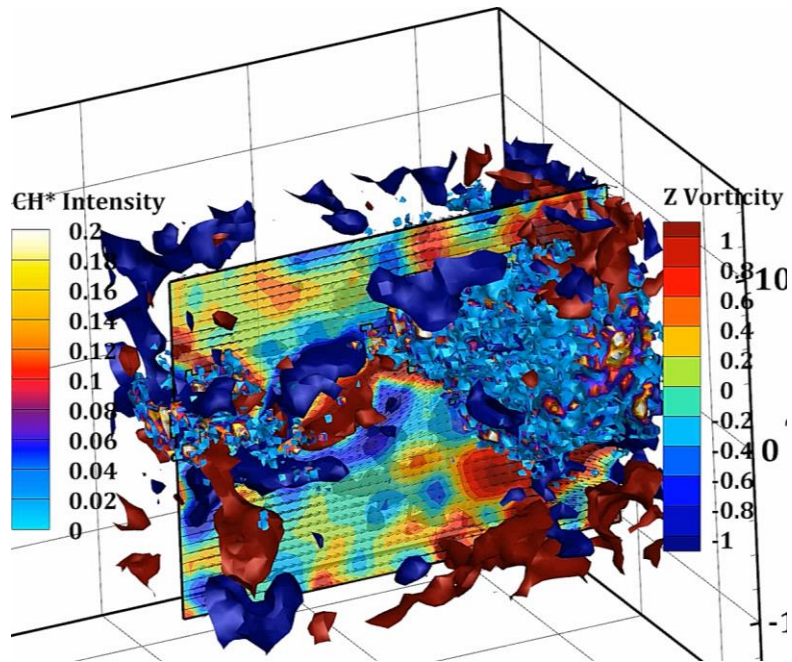


Figure 53: Plotted isosurfaces of the vorticity field in Figure 52B to display the size of the vortex structures that are inducing this flame hole.



## CHAPTER 11: CONCLUSIONS

A system has been developed that is capable of acquiring three-dimensional flame or PIV data with the use of one camera. By utilizing two cameras, for the first time, simultaneous, time resolved, three-dimensional flame and velocimetry measurements have been taken. Though for demonstration purposes both a steady flame and a blow off event were captured, where more complex analysis can be done. The system has shown to produce accurate information and shows great value in supplying laboratories with a means of acquiring three-dimensional data.

The system as a whole has very little uncertainty. Both, in alignment and in data acquisition. This system has the added benefit of being cost effective, comparatively small relative to other tomographic imaging systems. The system is robust and easily transported. It has been stringently compared to standard velocimetric measurements and has shown very little deviation. The system is also able to capture flow fields in a confined space.

Future work on this system will be done in extending its capabilities in acquiring three-dimensional fuel air data. By combining the approach utilized in the line of sight fuel air approach to the tomographic system and coupling with three-dimensional PIV, it is possible to back calculate the three-dimensional density field and capture all three components of velocity. This would allow for a very accurate calculation of the Navier-Stokes equations. Lastly, it is planned to compare this system to computational work. That is where this system is most needed. Most models are easily adapted to extract three-dimensional information but lack the experimental data to validate the conclusion. This system will help fill in such gaps. Other planned work includes utilizing the system to perform low seed density three-dimensional Lagrangian tracking and extending the field of view to capture more spatial information.

## LIST OF REFERENCES

- [1] F. Zhao *et al.*, “PROGRESS IN ENERGY AND Automotive spark-ignited direct-injection gasoline engines,” *Prog. Energy Combust. Sci.*, no. 25, pp. 437–562, 1999.
- [2] P. Sementa, B. Maria Vaglieco, and F. Catapano, “Thermodynamic and optical characterizations of a high performance GDI engine operating in homogeneous and stratified charge mixture conditions fueled with gasoline and bio-ethanol,” *Fuel*, vol. 96, pp. 204–219, 2012.
- [3] K. Reif Ed, *Gasoline Engine Management Bosch Professional Automotive Information*. .
- [4] N. Kawahara, A. Inoue, and E. Tomita, “Time-series Spectra Measurements from Initial Flame Kernel in a Spark-Ignition Engine,” *17th Int. Symp. Appl. Laser Tech. to Fluid Mech.*, no. Iccd, pp. 7–10, 2014.
- [5] Z. Wang, H. Liu, and R. D. Reitz, “Knocking combustion in spark-ignition engines,” *Prog. Energy Combust. Sci.*, vol. 61, pp. 78–112, 2017.
- [6] Z. Wang *et al.*, “Relationship between super-knock and pre-ignition,” *Int. J. Engine Res.*, vol. 16, no. 2, pp. 166–180, 2015.
- [7] M. C. Drake, T. D. Fansler, and A. M. Lippert, “Stratified-charge combustion: Modeling and imaging of a spray-guided direct-injection spark-ignition engine,” *Proc. Combust. Inst.*, vol. 30 II, no. 2, pp. 2683–2691, 2005.
- [8] Y. K. Jeong, C. H. Jeon, and Y. J. Chang, “Evaluation of the equivalence ratio of the reacting mixture using intensity ratio of chemiluminescence in laminar partially premixed

- CH<sub>4</sub>-air flames,” *Exp. Therm. Fluid Sci.*, vol. 30, no. 7, pp. 663–673, 2006.
- [9] T. P. (Lewis F. P. L. Clark, “Studies of Oh, Co, Ch, and C<sub>2</sub> Radiation From Laminar and Turbulent Propane-Air and Ethylene-Air Flames,” *Natl. Advis. Committee Aeronaut.*, no. 4266, p. 25, 1955.
- [10] T. S. Cheng, C. Y. Wu, Y. H. Li, and Y. C. Chao, “Chemiluminescence measurements of local equivalence ratio in a partially premixed flame,” *Combust. Sci. Technol.*, vol. 178, no. 10–11, pp. 1821–1841, 2006.
- [11] C. Jeon, S. Choi, H. Park, and Y. Chang, “Combustion Analysis by Radical Intensity Measurement and Instantaneous Image in a Constant Volume Chamber,” *Int. Symp. COMODIA*, vol. 94, pp. 459–464, 1994.
- [12] H. Sawada, T. Suzuki, Y. Oguri, and M. Yoshida, “The Method of Measuring Air-Fuel Ratio by Radical Luminescence in High Combustion Pressure,” *SAE Tech. Pap.*, vol. 01, no. 0507, p. 10, 1999.
- [13] T. Chou and D. J. Patterson, “In-cylinder measurement of mixture maldistribution in a L-head engine,” *Combust. Flame*, vol. 101, no. 1–2, pp. 45–57, 1995.
- [14] Y. Ikeda, M. Kaneko, and T. Nakajima, “Local A/F Measurement by Chemiluminescence OH\*, CH\*, C<sub>2</sub>\* in SI Engine,” *SAE*, vol. 01, no. 0919, pp. 754–760, 2001.
- [15] J. Kojima, Y. Ikeda, and T. Nakajima, “Basic aspects of OH(A), CH(A), and C<sub>2</sub>(d) chemiluminescence in the reaction zone of laminar methane-air premixed flames,” *Combust. Flame*, vol. 140, no. 1–2, pp. 34–45, 2005.

- [16] J. Kojima, Y. Ikeda, and T. Nakajima, "Spatially resolved measurement of OH\*, CH\*, AND C\*<sub>2</sub> chemiluminescence in the reaction zone of laminar methane/air premixed flames," *Proc. Combust. Inst.*, vol. 28, pp. 1757–1764, 2000.
- [17] Y. Ikeda, T. Kurahashi, N. Kawahara, and E. Tomita, "Temperature Measurements of Laminar Propane / Air Premixed Flame Using Detailed OH\* Spectra Intensity Ratio," *12th Int. Symp. Appl. Laser Tech. to Fluid Mech.*, no. 1, pp. 1–11, 2004.
- [18] B. Higgins, M. Q. McQuay, F. Lacas, and S. Candel, "An experimental study on the effect of pressure and strain rate on CH chemiluminescence of premixed fuel-lean methane/air flames," *Fuel*, vol. 80, no. 11, pp. 1583–1591, 2001.
- [19] F. V. Tinaut, M. Reyes, B. Giménez, and J. V. Pastor, "Measurements of OH\* and CH\* chemiluminescence in premixed flames in a constant volume combustion bomb under autoignition conditions," *Energy and Fuels*, vol. 25, no. 1, pp. 119–129, 2011.
- [20] J. R. Kim, F. Akamatsu, G. M. Choi, and D. J. Kim, "Observation of local heat release rate with changing combustor pressure in the CH<sub>4</sub>/air flame (wrinkled laminar regime)," *Thermochim. Acta*, vol. 491, no. 1–2, pp. 109–115, 2009.
- [21] H. H. Geok, T. I. Mohamad, S. Abdullah, Y. Ali, A. Shamsudeen, and E. Adril, "Experimental investigation of performance and emission of a sequential port injection natural gas engine," *Eur. J. Sci. Res.*, vol. 30, no. 2, 2009.
- [22] P. Arroyo and C. A. Greated, "Stereoscopic particle image velocimetry," *Meas. Sci. Technol.*, vol. 2, pp. 1181–1186, 1991.

- [23] C. Willert, “Stereoscopic digital particle image velocimetry for application in wind tunnel flows,” *Meas. Sci. Technol.* *Meas. Sci. Technol.*, vol. 8, no. 8, pp. 1465–1479, 1997.
- [24] C. J. Kähler and J. Kompenhans, “Fundamentals of multiple plane stereo particle image velocimetry,” *Exp. Fluids*, vol. 29, no. 7, pp. S070–S077, 2000.
- [25] J. A. Mullin and W. J. A. Dahm, “Dual-plane stereo particle image velocimetry (DSPIV) for measuring velocity gradient fields at intermediate and small scales of turbulent flows,” *Exp. Fluids*, vol. 38, no. 2, pp. 185–196, 2005.
- [26] F. Scarano, “Tomographic PIV: Principles and Practice,” *Meas. Sci. Technol.*, vol. 24, no. 1, 2013.
- [27] N. Worth, T. Nickels, and N. Swaminathan, “A tomographic PIV resolution study based on homogenous isotropic turbulence DNS data,” *Exp. Fluids*, vol. 49, no. 3, pp. 637–656, 2010.
- [28] C. de Silva, R. Baidya, M. Khashehchi, and I. Marusic, “Assessment of tomographic PIV in wall-bounded turbulence using direct numerical simulation data,” *Exp. Fluids*, vol. 52, no. 2, pp. 425–440, 2012.
- [29] S. Herrmann and K. Hinsch, “Light-in-flight holographic particle image velocimetry for wind-tunnel applications,” *Meas. Sci. Technol.*, vol. 15, no. 4, pp. 613–621, 2004.
- [30] K. Hinsch, “Holographic particle image velocimetry,” *Meas. Sci. Technol.*, vol. 13, no. 7, pp. 61–72, 2002.
- [31] K. Hinsch, “Three-dimensional particle velocimetry,” *Meas. Sci. Technol.*, vol. 6, no. 6,

- pp. 742–753, 1995.
- [32] C. Brücker, “3D scanning PIV applied to an air flow in a motored engine.pdf,” vol. 8, pp. 1480–1492, 1997.
- [33] H. Maas, A. Gruen, and D. Papantoniou, “Particle tracking velocimetry in three-dimensional flows,” *Exp. Fluids*, vol. 15, no. 2, pp. 133–146, 1993.
- [34] A. Schimpf and S. Kallweit, “Photogrammetric Partice Image Velocimetry,” in *Stanislas M., Westerweel J., Kompenhans J. (eds) Particle Image Velocimetry: Recent Improvements.*, 2004, pp. 295–300.
- [35] F. Perera, M. Gharib, D. Dabiri, and D. Modarress, “Defocusing digital particle image velocimetry: a 3-component 3-dimensional DPIV measurement technique. Application to bubbly flows,” *Exp. Fluids*, vol. 29, no. S1, pp. 078–084, 2000.
- [36] T. Hori and J. Sakakibara, “High-speed scanning stereoscopic PIV for 3D vorticity measurement in liquids,” *Meas. Sci. Technol.*, vol. 15, no. 6, pp. 1067–1078, 2004.
- [37] S. Burgmann, C. Brücker, and W. Schröder, “Scanning PIV measurements of a laminar separation bubble,” *Exp. Fluids*, vol. 41, no. 2, pp. 319–326, 2006.
- [38] L. Schäfer and W. Schröder, “Comparison of holographic and tomographic particle-image velocimetry turbulent channel flow measurements,” *J. Phys. Conf. Ser.*, vol. 318, no. SECTION 2, pp. 1–7, 2011.
- [39] J. Sheng, E. Malkiel, and J. Katz, “Digital holographic microscope for measuring three-dimensional particle distributions and motions,” *Appl. Opt.*, vol. 45, no. 16, p. 3893, 2006.

- [40] G. E. Elsinga, F. Scarano, B. Wieneke, and B. W. Van Oudheusden, “Tomographic particle image velocimetry,” *Exp. Fluids*, vol. 41, no. 6, pp. 933–947, 2006.
- [41] D. Violato and F. Scarano, “Three-dimensional evolution of flow structures in transitional circular and chevron jets,” *Phys. Fluids*, vol. 23, no. 12, p. 124104, 2011.
- [42] D. Violato, P. Moore, and F. Scarano, “Lagrangian and Eulerian pressure field evaluation of rod-airfoil flow from time-resolved tomographic PIV,” *Exp. fluid*, vol. 50, no. 4, pp. 1057–1070, 2011.
- [43] R. a Humble, F. Scarano, B. W. Van Oudheusden, and B. W. van Oudheusden, “Experimental Study of an Incident Shock Wave/Turbulent Boundary Layer Interaction Using PIV,” *36th AIAA Fluid Dyn. Conf. Exhib.*, no. June, pp. 1–16, 2006.
- [44] J. Udovich, N. Kirkpatrick, A. Kano, A. Tanbakuchi, U. Utzinger, and A. Gmitro, “Spectral background and transmission characteristics of fiber optic imaging bundles,” *Appl. Opt.*, vol. 47, no. 25, pp. 4560–4568, 2008.
- [45] R.-D. Sun, A. Nakajima, I. Watanabe, T. Watanabe, and K. Hashimoto, “TiO<sub>2</sub>-coated optical fiber bundles used as a photocatalytic filter for decomposition of gaseous organic compounds,” *J. Photochem. Photobiol. A Chem.*, vol. 136, no. 1–2, pp. 111–116, 2000.
- [46] L. Yang, A. Mac Raighne, E. M. McCabe, L. A. Dunbar, and T. Scharf, “Confocal microscopy using variable-focal-length microlenses and an optical fiber bundle,” *Appl. Opt.*, vol. 44, no. 28, pp. 5928–5936, 2005.
- [47] A. R. Rouse, A. Kano, J. A. Udovich, S. M. Kroto, and A. F. Gmitro, “Design and

- demonstration of a miniature catheter for a confocal microendoscope,” *Appl. Opt.*, vol. 43, no. 31, pp. 5763–5771, 2004.
- [48] K. Carlson *et al.*, “In vivo fiber-optic confocal reflectance microscope with an injection-molded plastic miniature objective lens,” *Appl. Opt.*, vol. 44, no. 10, pp. 1792–1797, 2005.
- [49] M. W. Kang, X. Li, and L. Ma, “Calibration of Fiber Bundles for Flow and Combustion Measurements,” *52nd Aerosp. Sci. Meet.*, no. January, pp. 1–7, 2014.
- [50] M. M. Hossain, G. Lu, D. Sun, and Y. Yan, “Three-dimensional reconstruction of flame temperature and emissivity distribution using optical tomographic and two-colour pyrometric techniques,” *Meas. Sci. Technol.*, vol. 24, no. 7, 2013.
- [51] M. M. Moinul Hossain, G. Lu, and Y. Yan, “Optical fiber imaging based tomographic reconstruction of burner flames,” *IEEE Trans. Instrum. Meas.*, vol. 61, no. 5, pp. 1417–1425, 2012.
- [52] X. Zhang, C. Tang, H. Yu, Q. Li, J. Gong, and Z. Huang, “Laminar flame characteristics of iso-octane/n-butanol blend-air mixtures at elevated temperatures,” *Energy and Fuels*, vol. 27, no. 4, pp. 2327–2335, 2013.
- [53] G. E. Andrews and D. Bradley, “Determination of burning velocities: A critical review,” *Combust. Flame*, vol. 18, no. 1, pp. 133–153, 1972.
- [54] D. R. Dowdy, D. B. Smith, S. C. Taylor, and A. Williams, “The use of expanding spherical flames to determine burning velocities and stretch effects in hydrogen/air mixtures,” *Symp. Combust.*, vol. 23, no. 1, pp. 325–332, 1991.



- [55] M. Faghieh and Z. Chen, “The constant-volume propagating spherical flame method for laminar flame speed measurement,” *Sci. Bull.*, vol. 61, no. 16, pp. 1296–1310, 2016.
- [56] Z. Chen, M. P. Burke, and Y. Ju, “Effects of compression and stretch on the determination of laminar flame speeds using propagating spherical flames,” *Combust. Theory Model.*, vol. 13, no. 2, pp. 343–364, 2009.
- [57] F. N. Egolfopoulos, N. Hansen, Y. Ju, K. Kohse-Hoinghaus, C. K. Law, and F. Qi, “Advances and challenges in laminar flame experiments and implications for combustion chemistry,” *Prog. Energy Combust. Sci.*, vol. 43, pp. 36–67, 2014.
- [58] Y. H. Liao and W. L. Roberts, “Laminar Flame Speeds of Gasoline Surrogates Measured with the Flat Flame Method,” *Energy and Fuels*, vol. 30, no. 2, pp. 1317–1324, 2016.
- [59] J. Mi, P. Kalt, G. Nathan, and C. Wong, “PIV measurements of a turbulent jet issuing from round sharp-edged plate,” *Exp. Fluids*, vol. Experiment, no. 4, pp. 625–637, 2007.